National Technical University of Athens
School of Mechanical Engineering
Fluids Department
Parallel CFD & Optimization Unit

Programming of the Curle's Acoustic Analogy and the ENP Model for the Prediction of the Exterior Wind Noise from Car Geometries

Diploma Thesis

Andreas Spyropoulos

Supervisor : Kyriakos C. Giannakoglou, Professor NTUA

Athens, 2019

Acknownledgements

First and foremost, I would like to express my gratitude to my professor Kyriakos C. Giannakoglou, who assigned me this interesting and challenging topic for my diploma thesis. I also want to thank him for his precious advices, both technical and practical; their value were proven on the act and I wish I knew earlier their importance.

Also, as big part of this thesis was conducted in the premises of Toyota Motor Europe, I would like to deeply thank my mentor there, Mr. A. Delacroix, for his patience in explaining new things to me and his continuous support. I could not forget to thank my college, Panagiotis Koutsantonis, who was always eager to help and guide me in that new industrial environment.

My grateful thanks are also extended to all the member of the Parallel CFD & Optimization Unit of NTUA. Most important I would like to thank Dr. E. M. Papoutsis-Kiachagias and Kostas Gkaragounis for all the help they provided, introducing me to the OpenFOAM environment and continuously supporting my efforts.

Last but not least, I would like to thank my family for believing in me and my friends, during all the years of my studies, who accompanied me to that journey.

National Technical University of Athens
School of Mechanical Engineering
Fluids Department
Parallel CFD & Optimization Unit

Programming of the Curle's Acoustic Analogy and the ENP Model for the Prediction of the Exterior Wind Noise from Car Geometries

Diploma Thesis

Andreas Spyropoulos

Supervisor: Kyriakos C. Giannakoglou, Professor NTUA

Athens, 2019

Abstract

The purpose of this diploma thesis is to program and validate fast and relatively accurate methods for the aeroacoustic noise evaluation of passenger vehicles.

To this end, two methods were programmed in the OpenFOAM® environment, for which the DDES-SA turbulence model, based on wall functions, was used for the prediction of the unsteady turbulent flow field. The first method is a simplified version of Curle's acoustic analogy, which integrates the unsteady pressure fluctuations and its time derivatives on the solid surface and computes the acoustic pressure time signal at a distant receiver. Both the acoustic pressure at the far field and the unsteady pressure fluctuation on the surface are validated on a generic side mirror mounted on a flat plate through comparison with experimental data and other CFD simulations from the literature. In addition, three different convection schemes for the momentum equation were tested and their effects on the computed drag coefficient are compared.

The second method programmed was the Exterior Noise Power (ENP) method. Its output is the ENP index which represents the total acoustic power radiated from the car surface on the far-field. The method also stands as a virtual noise source localization technique, having as output a noise source intensity map on the vehicle's surface. For this method, correlation of the resulting ENP index with interior noise measurements and beamforming results for two different car geometries was conducted. These experimental data was acquired through testing in the semi-anechoic S2A GIE wind tunnel in France, in which the writer of this thesis participated during his internship.

Major part of this diploma thesis was carried out in the premises of Toyota Motor Europe (TME) in Brussels, Belgium, during an 8 month long internship, with Mr A. Delacroix as the industrial advisor.

Εθνικό Μετσόβιο Πολυτεχνείο
Σχολή Μηχανολόγων Μηχανικών
Τομέας Ρευστών
Μονάδα Παράλληλης Υπολογιστικής Ρευστοδυναμικής & Βελτιστοποίησης

Προγραμματισμός της Ακουστικής Αναλογίας του Curle και του Μοντέλου ENP για την Πρόλεξη του Αεροδυναμικά Επαγόμενου Εξωτερικού Θορύβου από Γεωμετρίες Αυτοκινήτου

Διπλωματική Εργασία

Ανδρέας Σπυρόπουλος

Επιβλέπων: Κυριάκος Χ. Γιαννάκογλου, Καθηγητής ΕΜΠ

Αθήνα, 2019

Περίληψη

Σκοπός αυτής της διπλωματικής εργασίας είναι ο προγραμματισμός και η πιστοποίηση γρήγορων και αξιόπιστων μεθόδων για την αξιολόγηση του αεροδυναμικού θορύβου επιβατηγών οχημάτων.

Σε αυτή την κατεύθυνση, δύο μέθοδοι προγραμματίστηκαν στο περιβάλλον OpenFOAM®, για τις οποίες το μοντέλο τύρβης DDES-SA, με χρήση συναρτήσεων τοίχου χρησιμοποιήθηκε για την πρόλεξη του μη-μόνιμου τυρβώδους πεδίου ροής. Η πρώτη μέθοδος είναι μία απλοποιημένη εκδοχή της αναλογίας του Curle, η οποία ολοκληρώνει τις χρονικά μη-μόνιμες διαταραχές της πίεσης στην στερεή επιφάνεια και τις χρονικές τους παραγώγους και υπολογίζει το σήμα της ακουστικής πίεσης σε έναν απομακρυσμένο αποδέκτη. Πιστοποιούνται τόσο η ακουστική πίεση στο επ΄ άπειρο όριο, όσο και οι διαταραχές της πίεσης στην επιφάνεια στην περίπτωση του απλοποιημένου καθρέφτη σε επίπεδη πλάκα μέσω σύγκρισης με πειραματικά και αλλά δεδομένα προσομοιώσεων υπολογιστικής ρευστοδυναμικής από τη βιβλιογραφία. Επιπλέον, δοκιμάζονται τρία σχήματα διακριτοποίησης για την εξίσωση της ορμής και διερευνάται η επίδρασή τους στον συντελεστή αντίστασης.

Η δεύτερη μέθοδος που προγραμματίστηκε ήταν η μέθοδος Exterior Noise Power (ENP). Αποτέλεσμα της εφαρμογής της μεθόδου είναι ο δείκτης ENP, ο οποίος αναπαριστά τη συνολική ακουστική ισχύ που εκπέμπεται από την επιφάνεια του αυτοκινήτου στο επ΄ άπειρο όριο. Ακόμη, η μέθοδος αποτελεί μία εικονική τεχνική beamforming, ικανή να εντοπίσει τις αερακουστικής πηγές θορύβου στην επιφάνεια του οχήματος. Για αυτήν τη μέθοδο, πραγματοποιήθηκε συσχέτιση του δείκτη ENP με μετρήσεις του θορύβου στο εσωτερικό και με αποτελέσματα της πειραματικής τεχνικής beamforming για δύο γεωμετρίες αυτοκινήτου. Τα πειραματικά δεδομένα αποκτήθηκαν μέσω μετρήσεων στην ημι-ανηχοϊκή αεροσήραγγα S2A GIE στη Γαλλία, στις οποίες συμμετείχε και

ο συγγραφέας αυτής της διπλωματικής εργασίας κατά τη διάρκεια της πρακτικής του άσκησης.

Το μεγαλύτερο μέρος αυτής της εργασίας πραγματοποιήθηκε στις εγκαταστάσεις της Toyota Motor Europe (TME) στις Βρυξέλλες, κατά τη διάρκεια μίας οκτάμηνης πρακτικής άσκησης, με τον κ. Antoine Delacroix ως επιβλέποντα από την πλευρά της βιομηχανίας.

Acronyms

CFD	Computational Fluid Dynamics
NTUA	National Technical University of Athens
PCopt	Parallel CFD & Optimization unit
TMC	Toyota Motor Company
TME	Toyota Motor Europe

PDE	Partial Differential Equation
PF	Pressure Fluctuation
PL	Pressure Level
DDES	Delayed Detached Eddy Simulation
DES	Detached Eddy Simulation
DNS	Direct Numerical Simulation
ENP	Exterior Noise Power
ENPD	Exterior Noise Power Distribution
FFT	Fast Fourier Transform
LES	Large Eddy Simulation
NS	Navier-Stokes
RANS	Reynolds-Averaged Navier-Stokes
SA	Spalart-Allmaras
SGS	Sub-grid Scale
SPL	Sound Pressure Level
URANS	Unsteady Reynolds-Averaged Navier-Stokes

Contents

Chapter 1

Introduction

In recent years, the numerous innovations of powertrain technologies have led to significant reductions in the interior noise contributions from the engine, tires and irregular road surface. This along with the electrification trend which will further minimize the engine noise have made exterior wind noise the most dominant noise source at higher car speeds, generally above 100 km/h. Given the fact that interior noise has a strong influence on customer perception and is, also, important for safety and comfort, evaluation and understanding of this noise source is a key factor for the development of quality and competitive vehicles.

1.1 Basic Definitions of Acoustics

1.1.1 Sound Pressure

As described in [1], the perception of sound is the response to a physical stimulus to the ear. This stimulus is the unsteady sound pressure

$$p'(t) := p(t) - \overline{p} \quad [Pa] \tag{1.1}$$

where $\overline{p}$ the temporal average of $p(t)$.

In the following chapters, the term noise will occasionally be used to refer to disturbing, undesirable sound.

An appropriate measure of the strength of an acoustic signal is the root mean square

p_{rms} of pressure fluctuations, given by

$$p_{rms} = \sqrt{\overline{(p')^2}} \tag{1.2}$$

Because of the large range of rms-values which are audible by the human ear, the logarithmic scale is often used to describe acoustic quantities.

The sound pressure level L_p or SPL is defined as

$$L_p := 10 \log_{10} \frac{{p_{rms}}^2}{p_{ref}} = 20 \log_{10} \frac{p_{rms}}{p_{ref}} \quad [dB] \tag{1.3}$$

where $p_{ref} = 2 \cdot 10^{-5} Pa$, i.e. a reference value, corresponding approximately to the smallest perceivable pressure amplitude, called threshold of hearing.

1.1.2 Sound Intensity

The sound intensity $\vec{I}$ represents the acoustic power per unit surface. It's a vector, with direction the average direction in which energy is flowing. For a stagnant medium at rest, sound intensity is derived from the sound pressure and the acoustically induced local motion of the medium, namely the acoustic particle velocity $\vec{v'}$ like

$$\vec{I}(\vec{x}) := \overline{p'\vec{v'}} \quad [W/m^2] \tag{1.4}$$

The corresponding sound intensity level L_I is defined by

$$L_I := 10 \log_{10} \frac{|\vec{I}|}{I_{ref}} \quad [dB] \tag{1.5}$$

where $I_{ref} = 10^{-12} W/m^2$ is a reference value.

1.1.3 Sound Power

The sound power P emitted by a source is obtained by integrating sound intensity normal to a surface enclosing the source over that surface as

$$P := \oint_A \vec{I} \cdot \vec{n} dA \quad [W] \tag{1.6}$$

where $\vec{n}$ the unit normal vector on the surface.

The corresponding sound power lever L_W is given by

$$L_W := 10 \log_{10} \frac{P}{P_{ref}} \quad [dB] \tag{1.7}$$

where $P_{ref} = 10^{-12} W$.

1.2 Distinction of Noise Contributors

In this section, a distinction of noise to acoustic or aeroacoustic and hydrodynamic or "pseudo-sound", as is often referred to, will be made.

1.2.1 Aeroacoustic Noise

The term aeroacoustic or acoustic noise refers to pressure fluctuations, raised by mechanisms related to the turbulent fluid flow and propagate as acoustic waves with the speed of sound in the medium. There are three principal mechanisms of aeroacoustic noise generation [2],[3],[4],[5] and can be approximated by an idealized model (fig. 1.1) as:

- **Monopole sources:** The ideal monopole source radiates sound equally in all directions and can be represented by an infinitely small sphere whose radius alternately expands and contracts. A monopole-like source is related to a time variable displacement of mass flow. As an example, the noise emanating from a leakage of air inside the cabin of a vehicle is, mostly, of monopole character.
- **Dipole sources:** In the idealized case, two monopoles with opposite phase in close distance comprise an acoustic dipole. A dipole-like noise source is associated with unsteady pressure fluctuations upon a rigid surface. The whole surface can be viewed as a distributed dipole sound source with power depending on the temporal variation of the surface pressures. The von Karman vortex shedding or the presence of vortical structures in the flow, inducing pressure fluctuations on a solid surface are examples of dipole-like noise sources.
- **Quadrupole sources:** A quadrupole noise source consists of two identical dipoles, with opposite phase at a small distance from each other. A quadrupole-like source originates from unsteady internal stresses in the fluid, such as in the shear layer at the periphery of a jet or the wake of a blade. Sound radiated by free turbulence and shock waves are also cases of quadrupole-like sources.

(a) Monopole (b) Dipole (c) Quadrupole

Figure 1.1: *Fundamental acoustic sources. From [6].*

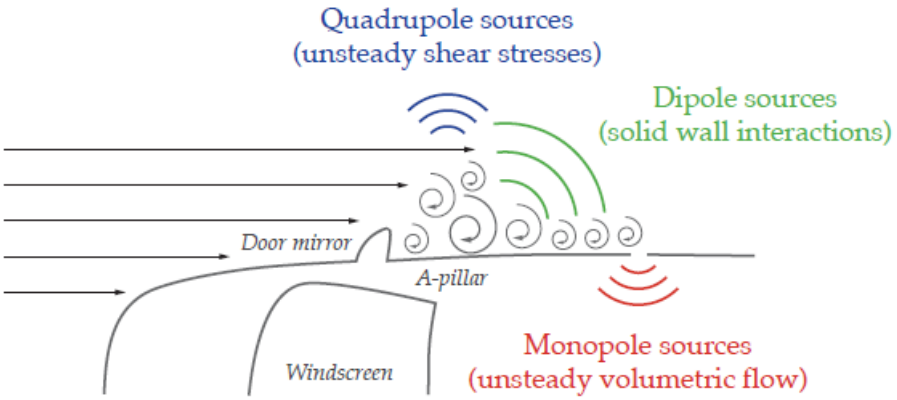

Figure 1.2: *Aeroacoustic noise sources on a commercial vehicle. From [2].*

Based on the idealized models, the acoustic intensity I of different noise sources can be scalled as [2]:

$$I_{monopole} \sim \frac{\rho}{c} u^4 = \rho u^3 M \tag{1.8}$$

$$I_{dipole} \sim \frac{\rho}{c^3} u^6 = \rho u^3 M^3 \tag{1.9}$$

$$I_{quadrupole} \sim \frac{\rho}{c^5} u^8 = \rho u^3 M^5 \tag{1.10}$$

where u is the flow speed, c the speed of sound, M is the Mach number and ρ the density.

For a low Mach number case, such as a car cruising at $100 - 120 km/h$ i.e. $M = 0.08 - 0.09 < 0.1$ the most dominant noise sources are of monopole character, followed by dipole-like and quadrupole-like sources. As a result, for a perfectly sealed car, in which sources of monopole character are absent, the dipole sources dominate the overall cabin noise of a road vehicle. Beside the fact that dipole noise sources are evident all over the car surface, the most likely to be transmitted inside the cabin and contribute to the interior noise at the drivers ear are located in the vicinity of the A-pillar and side mirror region. This is due to the fact, that these are close to the driver and side glass and windshield surfaces are better transmitting paths than the panels.

1.2.2 Hydrodynamic Noise

Hydrodynamic noise is related to the pressure fluctuations induced by the unsteady turbulent flow. These fluctuations do not propagate, but are convected with the eddy structures in the flow and often, are at a much higher level than the fluctuations of the acoustic field. However, the acoustic field has equal or even greater contribution to the noise inside the cabin [7],[8],[9] depending on the frequency. The reason for that depends on the transmission mechanism of the side glass.

1.2.3 Contribution of the Different Types of Noise to the Interior Noise

The wavenumber k of a pressure wave fluctuating at frequency f, is a function of its wave speed v as follows:

$$k = \frac{2\pi f}{v} = \frac{\omega}{v} \tag{1.11}$$

The hydrodynamic pressure fluctuations are convected with the local convection velocity, often one order of magnitude smaller than the propagation speed of the acoustic waves, which is the speed of sound and, hence, from eq. 1.11 the wavenumber of acoustic waves is one order of magnitude smaller than the hydrodynamic one. Although in the exterior, the acousic part is masked by the hydrodynamic, the glazing provides a strong filter for higher wavenumber hydrodynamic fluctuations, attenuating their amplitude in the interior, as these do not couple as effectively with the structural vibration characteristics of the side glass [2]. As a result, for the interior noise the contribution of both the hydrodynamic and the acoustic part of noise should be considered.

1.3 Different CAA Approaches to Compute the Far Field Noise

In figure 1.3, three different approaches to a computational aeroacoustic (CAA) problem are presented [10]. The first one, is a direct method, which requires to solve the full compressible N-S equations for all the scales all the way to the reciever, which translates to great computational cost due to the small timesteps and grid size needed to all-in-one solve the acoustics and the turbulent flow field. These disadvantages makes this method non-applicable to large industrial cases and other techniques have risen, namely the separation of the acoustic generation and propagation. In that direction, the second and third approach tries to model the sound

generation based on an incompressible manner for low Mach number cases, based on the assumption that the generation and propagation are decoupled. The last claim is valid only in one-way coupled cases, in which energy is being transfer only from the flow to the acoustics and not the other way around. Most of the flows of interest in low Mach number cases are one-way coupled, expect cases related to resonant effects were two-way coupling is evident. In the latter case a compressible approach should be used to model the noise generation. The main difference of the second and third approach is the propagation of the noise. On the one hand, one can use an integral formulation of an acoustic analogy to propagate the noise, which is more straightforward and computationally less demanding and, on the other hand, the acoustic analogy on its differential form or the Linear Euler Equations needs to be solved. Besides the difference in computational cost, solving the acoustic analogy numerically as a differential equation includes all the physics of noise propagation, namely reflection, refraction and interaction of acoustic waves; physics that is left out in the integral formulation. The advantage of the integral methods is that, for simple geometries, such as the side mirror and the A-pillar of a vehicle, in which no reflections are expected, have proven to be accurate and much faster.

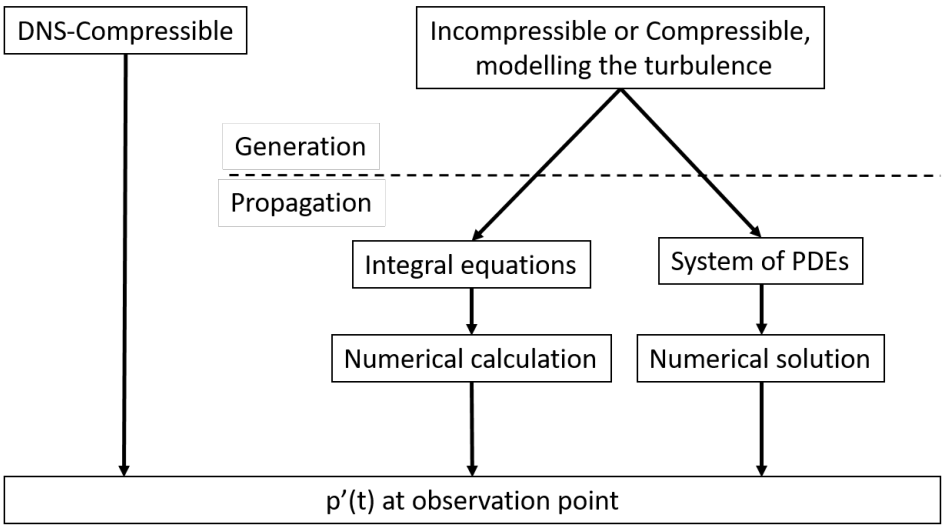

Figure 1.3: *Different CAA approaches used to calculate the acoustic noise at a receiver at the farfield.*

1.4 Purpose and Structure of the Thesis

The purpose of this diploma thesis is to tackle the problem of wind noise evaluation of conventional car vehicles. To that end, two aeroacoustic noise evaluation methods have been programmed in the OpenFOAM environment. The first of them, is the Curle's integral method able to predict the acoustic pressure signal at a receiver;

this signal is induced aerodynamically by the flow on a surface. These unsteady pressure fluctuations on the surface are the input the Curle's method. The second method, the ENP method is based on the Curle's acoustic analogy and has the total acoustic power radiating to the far field from a car geometry and an acoustic source map on the surface as output.

This thesis includes the following chapters:

Chapter 2: The Navier-Stokes equations, solved to predict the flow field along with the different approaches of turbulence modeling are outlined.

Chapter 3: Includes the theory of the Curle's acoustic analogy and the ENP method, along with some notes on their numerical implementation in OpenFOAM.

Chapter 4: Both the Curle's integral and the ENP method are applied in automotive cases and their validity is tested.

Chapter 5: Conclusions about the methods used and suggestions for future research are summarized.

Chapter 2

The CFD Analysis

2.1 About turbulence

As described in [11], Lewis Richardson summarized the process of a turbulent flow in one of his papers as:

Big whirls have little whirls
that feed on their velocity,
and little whirls have lesser whirls
and so on to viscosity.

A turbulent flow is chaotic and contains many small eddies which contains eddies by themselves. Due to this chaotic nature the exact, time accurate flow quantities on a turbulent flow are impossible to be predicted until now. In order to evaluate their mechanical structures, involved in turbulent flows, engineers have tried to extract statistical properties of the quantities of interest. This effort resulted in many different approaches to turbulence modeling.

Lewis F. Richardson in the 1920s and latter Andrey Kolmogorov at 1941 made a breakthrough on the understanding of turbulence with the theory of the energy cascade. According to the energy cascade theory, the larger eddies contains most of the kinetic energy, whereas the smallest eddies are responsible for the viscous dissipation of turbulent kinetic energy. Kolmogorov stated that the transfer of energy originates from the low wavenumber towards the high wavenumbers. This transfer brings turbulent kinetic energy from the large scales to the small scales, at which viscous friction dissipates it. Kolmogorov's hypothesis led to the following

universal form for the energy spectrum:

$$E(k) = C\epsilon^{2/3}k^{-5/3} \tag{2.1}$$

where E the turbulent kinetic energy, k the wavenumber of the eddies, ϵ the dissipation rate and C a constant ($C = 1.5$, experimentally observed), viewed also in fig. 2.1.

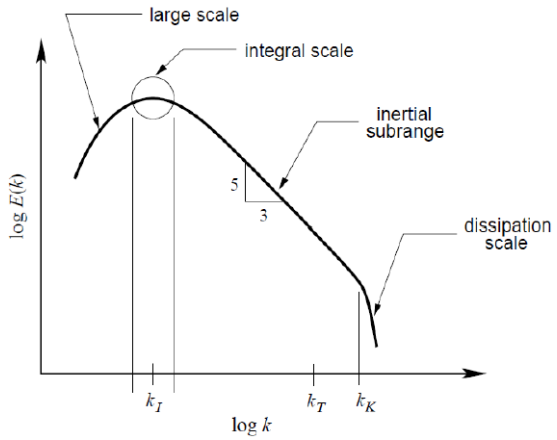

Figure 2.1: *Energy cascade. From [12]*

.

2.2 Navier-Stokes equations

The Navier-Stokes equations for incompressible Newtonian fluids, namely the continuity and the momentum equation are given by:

$$\frac{\partial \upsilon_j}{\partial x_j} = 0 \tag{2.2}$$

$$\frac{\partial \upsilon_i}{\partial t} + \upsilon_j \frac{\partial \upsilon_i}{\partial x_j} = \frac{\partial p}{\partial x_i} + \frac{\partial}{\partial x_j}\left[\nu\left(\frac{\partial \upsilon_i}{\partial x_j} + \frac{\partial \upsilon_j}{\partial x_i}\right)\right] \tag{2.3}$$

where a twice repeated index means summation according to the Einstein convention, υ_i stand for the velocity components, p the pressure and ν the kinematic viscosity.

To directly solve these equations and account for the turbulence, very fine mesh, depending on the Reynolds number of the flow, and proper numerical schemes and methods are needed, making this approach possible only in small research cases of low Reynolds number. For this reason, turbulence needs to be modeled.

2.3 Reynolds-Averaged Navier-Stokes Equations

For the majority of the cases, one of the simplest and reliable model of turbulence comes from applying Reynolds or time-averaging on the original equations of state. This leads to the Unsteady Reynolds Averaged Navier-Stokes (URANS) equations. The term "unsteady" comes in contrast with the term "averaged". To make things clear (fig. 2.2), the time-averaging of the NS equations is applied to the smaller time scales while the model is still able to predict the larger time unsteadiness of the flow field. The unsteady mean flow equations are written as:

$$R^p = -\frac{\partial \upsilon_j}{\partial x_j} \tag{2.4}$$

$$R_i^v = \frac{\partial \upsilon_i}{\partial t} + \upsilon_j \frac{\partial \upsilon_i}{\partial x_j} - \frac{\partial}{\partial x_j}\left[(\nu + \nu_t)(\frac{\partial \upsilon_i}{\partial x_j} + \frac{\partial \upsilon_j}{\partial x_i})\right] + \frac{\partial p}{\partial x_i} \tag{2.5}$$

In the above equations, the Boussinesq hypothesis has been used to model the Reynolds stresses resulting in an additional unknown field, namely, the turbulent viscocity ν_t. According to this hypothesis,

$$\tau'_{ij} = -\rho\overline{\upsilon'_i\upsilon'_j} = \rho\nu_t(\frac{\partial \overline{\upsilon_i}}{\partial x_j} + \frac{\partial \overline{\upsilon_j}}{\partial x_i}) - \frac{2}{3}k\delta_{ij} \tag{2.6}$$

whereby $k = \frac{1}{2}\overline{\upsilon'_i\upsilon'_i}$ and τ'_{ij} means Reynolds stress.

In order to "close" the system of equations, a model for the turbulent viscosity is needed. For one-equation turbulence models, the last term $-\frac{2}{3}k\delta_{ij}$ is generally ignored.

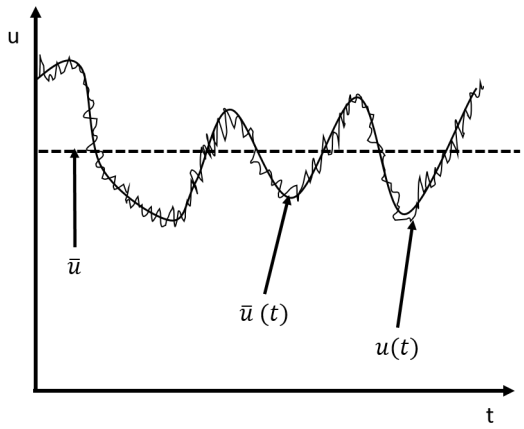

Figure 2.2: *Representation of the steady mean value $\overline{u}$, the unsteady mean value $\overline{u}(t)$ and the instantaneous value $u(t)$.*

2.3.1 The Spalart-Allmaras Turbulence Model

The Spalart-Allmaras is a one-equation mixing-length turbulence model [13]. Its equation (eq. 2.9) solves for a new viscocity-like variable, the Spalart-Allmaras variable, or $\tilde{\nu}$. When solved, the turbulent viscosity is explicitly computed through:

$$\nu_t = \tilde{\nu} f_{v1} \tag{2.7}$$

$$f_{v1} = \frac{X^3}{X^3 + C_{v1}^3}, \quad X = \frac{\tilde{\nu}}{\nu} \tag{2.8}$$

The PDE of the Spalart-Allmaras model is the following:

$$\frac{\partial \tilde{\nu}}{\partial t} + \frac{\partial (\tilde{\nu} v_j)}{x_j} = C_{b1}(1 - f_{t2})\tilde{S}\tilde{\nu} + \frac{1}{\sigma}\left[\frac{\partial}{x_j}\left((\nu + \tilde{\nu})\frac{\tilde{\nu}}{x_j}\right) + C_{b2}\frac{\partial \tilde{\nu}}{\partial x_i}\frac{\partial \tilde{\nu}}{\partial x_i}\right] - \left[C_{w1} f_w - \frac{C_{b1}}{\kappa^2} f_{t2}\right]\left(\frac{\tilde{\nu}}{d}\right)^2 \tag{2.9}$$

Quantities $\sigma = 2/3, C_{b1} = 0.1355, C_{b2} = 0.622, \kappa = 0.41, C_{w1} = 3.239, C_{v1} = 7.1$ are turbulence constants, d is the distance of each field point from the nearest wall and $\tilde{S}, f_{t2}, f_w$ are computed using the following equations:

$$\tilde{S} = \Omega + \frac{\tilde{\nu}}{\kappa^2 d^2} f_{v2} \tag{2.10}$$

$$\Omega = \sqrt{2 W_{ij} W_{ij}} \tag{2.11}$$

$$W_{ij} = \frac{1}{2}\left(\frac{\partial v_i}{\partial x_j} - \frac{\partial v_j}{\partial x_i}\right) \tag{2.12}$$

$$f_{v2} = 1 - \frac{X}{1 + X f_{v1}} \tag{2.13}$$

$$f_w = g\left[\frac{1 + c_{w3}^6}{g^6 + c_{w3}^6}\right]^{1/6} \tag{2.14}$$

$$g = r + c_{w2}(r^6 - 6) \tag{2.15}$$

$$r = min\left[\frac{\tilde{\nu}}{\tilde{S}\kappa^2 d^2}, 10\right] \tag{2.16}$$

$$f_{t2} = c_{t3} e^{-c_{t3} X^2} \tag{2.17}$$

In the RANS equations, the time derivative term is missing from both, the momentum equation (eq. 2.5), and the Spalart-Allmaras equation (eq. 2.9).

2.4 Large Eddy Simulation (LES)

In contrast to the RANS formulation, the Large Eddy Simulation [14] is trying to approach the DNS, resolving most of the scales. Specifically, the LES approach is trying to solve for the larger length scales which contain 80% of the energy and model the rest scales, which cannot be resolved due to the inappropriate mesh size, with a sub-grid scale (SGS) model. It's clear that, for this model to be accurate, an extensive effort should be placed on mesh generation. The first step taken in order to describe the LES equations is to use a filtering process. The filter splits the flow domain into two regions, the resolved and the modeled.

Applying the filter, each flow quantity f is represented by a resolved and a residual part [15],

$$f = \tilde{f} + f' \tag{2.18}$$

and the filtering process is represented mathematically in physical space as a convolution product. The filtered part of a variable $f(\vec{x})$, $\vec{x}$ being a vector of space is defined by:

$$\tilde{f}(\vec{x}) = \int_{-\infty}^{\infty} G(\vec{x} - \vec{x'}, \Delta) f(x') d^3\vec{x'} \tag{2.19}$$

where the kernel G is characteristic of the filter used and is associated with the cut-off scale Δ. The kernel is a localized function or function with compact support (i.e. the function is large only when $|\vec{x} - \vec{x'}|$ is small) and must satisfy the condition:

$$\int_{-\infty}^{\infty} G(\vec{x}) d^3\vec{x} = 1 \tag{2.20}$$

so that $\tilde{\alpha} = \alpha$, α being a constant.

Although, the filter's kernel is based on spatial filtering, temporal filtering is also implied, since the dynamics of Navier-Stokes equations make it possible to associate a characteristic time scale with a length scale [16]. A graphical representation of the filtering process, in the one-dimensional space is shown in fig. 2.3. The filtered equations are given by:

$$-\frac{\partial \widetilde{v_j}}{\partial x_j} = 0 \tag{2.21}$$

$$\frac{\partial}{\partial t}(\widetilde{v_i}) + \frac{\partial \widetilde{v_i v_j}}{\partial x_j} + \frac{\partial \widetilde{p}}{\partial x_i} - \frac{\partial}{\partial x_j}\left[\nu\left(\frac{\partial \widetilde{v_i}}{\partial x_j} + \frac{\partial \widetilde{v_j}}{\partial x_i}\right)\right] \tag{2.22}$$

Term $\widetilde{v_i v_j}$ in eq. 2.22 is not in the usual form of $\widetilde{v_i}\widetilde{v_j}$, which could easily be dis-

cretized. This term can be modeled as:

$$\begin{aligned}\widetilde{(\widetilde{v}_i\widetilde{v}_j + v_i v_j - \widetilde{v}_i\widetilde{v}_j)} &= \widetilde{(\widetilde{v}_i\widetilde{v}_j + (\widetilde{v}_i + {v_i}')(\widetilde{v}_j + {v_j}') - \widetilde{v}_i\widetilde{v}_j)} \\ &= \widetilde{(\widetilde{v}_i\widetilde{v}_j)} + \left(\widetilde{(\widetilde{v}_i\widetilde{v}_j - \widetilde{v}_i\widetilde{v}_j)}\right) + \left(\widetilde{(v_i'\widetilde{v}_j)} + \widetilde{(\widetilde{v}_i v_j')}\right) + \left(\widetilde{(v_i'v_j')}\right) \\ &= \widetilde{(\widetilde{v}_i\widetilde{v}_j)} + \tau_{SGS}\end{aligned}$$

The term τ_{SGS} represents the subgrid scale stresses and needs to be modeled.

For the practical application of some SGS models, implicit filtering is employed by the grid itself. Nevertheless, there are some models in which explicit filtering is needed to filter the smallest resolved scales corrupted by numerical error.

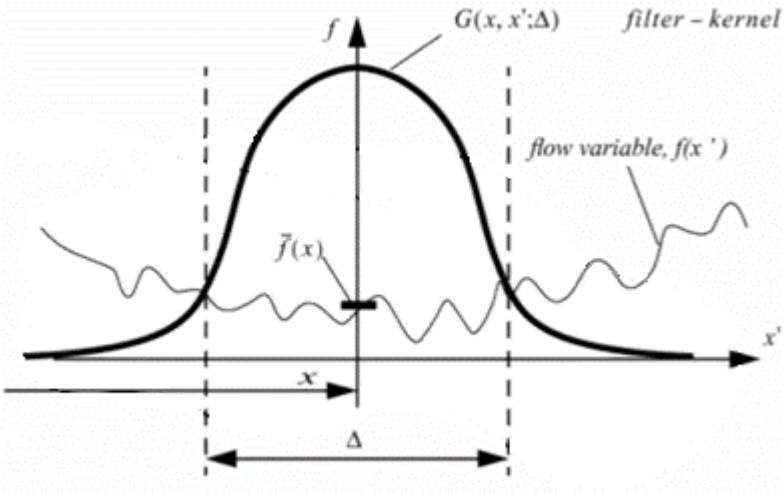

Figure 2.3: *One-dimensional representation of an arbitary filter function. The filter is being applied to a flow variable $f(x)$, x being the distance in one dimension, G the filter kernel in space location x, with characteristic length Δ and x' a local coordinate system with center the center of the kernel. The outcome is the filtered variable $\overline{f}(x)$. From [15].*

2.5 DES based on Spalart-Allmaras model(DES-SA)

In general, the LES formulation requires very fine grids and as a result the computational time is increased a lot. For this reason, a hybrid RANS-LES method, the Detached Eddy Simulation method, which combines the speed of the RANS with

the accuracy of the LES have been developed [17]. What makes the hybridization easy is the similarity of the URANS equations, eqs. 2.4, 2.5 with the LES equations, eqs. 2.21, 2.22; these are practically the same. These equations are solved together with the Spalart-Allmaras model eq. 2.9, which is modified to play the role of the sub-grid scale model in LES mode. The last term in eq. 2.9, which represents the destruction of $\tilde{\nu}$ depending on the wall distance d, is replaced by

$$\tilde{d} = min(d, C_{DES}\Delta) \tag{2.23}$$

where the constant $C_{DES} = 0.65$ by means of isotropic turbulence and Δ the characteristic grid size, usually chosen as

$$\Delta = max(\Delta x, \Delta y, \Delta z) \tag{2.24}$$

for anisotropic grids. If $d < C_{DES}\Delta$, which is the case close to the wall (fig. 2.4), parameter $\tilde{d}$ is equal to the wall distance d, resulting in the original RANS-SA model. Away from the wall, where the characteristic grid size Δ is increasing, $\tilde{d}$ equals $C_{DES}\Delta$. As a results, SA model turns into an LES one-equation SGS model. A reduced length scale increases the destruction term and, hence, yields a reduced eddy viscosity. Figure 2.4 illustrates the switch from the RANS to the LES mode when the local grid size is greater than the distance from the wall.

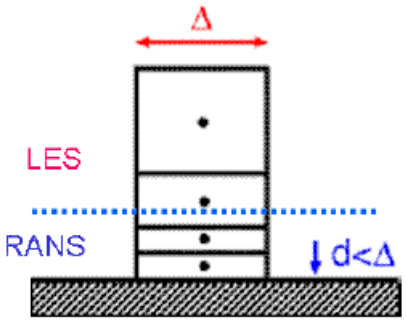

Figure 2.4: *Illustration of the switch between RANS and LES in the DES approach as discussed in the text. From [18].*

The term Detached Eddy Simulation illustrates the fact that this model is blending LES away from the boundaries, to resolve the detached eddies, with a RANS for the near wall flow. The latter aims to a suitable description of the near wall flow in a statistical sense, which only requires fine grid in the wall normal direction, contrary to LES, in which fine grid in all directions is needed.

2.5.1 Delayed Detached Eddy Simulation method (DDES)

The original formulation of the DES was very sensitive to the mesh size, resulting in early transition to LES mode close to the wall if the mesh was not proper. In order to avoid this behavior, a shielding function f_d was added to the definition of the dissipation length-scale,

$$\tilde{d} = d - f_d max(0, d - \Psi C_{DES}\Delta) \tag{2.25}$$

$$f_d = 1 - tanh[(8r_d)^3] \tag{2.26}$$

where r_d is given by

$$r_d = \frac{\nu_t + \nu}{\kappa^2 d^2 \sqrt{\left(\frac{\partial v_i}{\partial x_j}\right)^2}} \quad or \quad \frac{\tilde{\nu}}{\kappa^2 d^2 S} \tag{2.27}$$

in which κ is the Karman constant and d the distance from the wall.

Parameter r_d, borrowed from the S-A model (chapter 2.3.1) and modified, equals 1 in the logarithmic layer, and falls to 0 gradually towards the end of the boundary layer. Function f_d was designed to be 1 in the LES region (away from the wall, where $r_d << 1$) and 0 elsewhere (fig. 2.5). In that way, it forces DES to solve attached boundary layers in RANS mode ($\tilde{d} = d$) irrespective of the grid resolution. The dependency on the solution through the f_d intents to prevent the early switch to LES mode and, thus, the new model was named Delayed Detached Eddy Simulation(DDES) [19]. The additional dependency on the solution, although beneficiary in general, can result in a sensitivity of mean flow values to the initial conditions, as stated in [18].

Coefficient Ψ equals

$$\Psi^2 = min\left[10^2, \frac{1 - \frac{c_{b1}}{c_{w1}\kappa^2 f_w^*}[f_{t2} + (1 - f_{t2})f_{v2}]}{f_{v1} max(10^{-10}, 1 - f_{t2})}\right] \tag{2.28}$$

and represents a low-Reynolds number correction, introduced in order to compensate the activation of the low-Reynolds number terms of SA model in LES mode, where all the notations are the same as in the SA model (chapter 2.3.1) and $f_w^* = 0.424$.

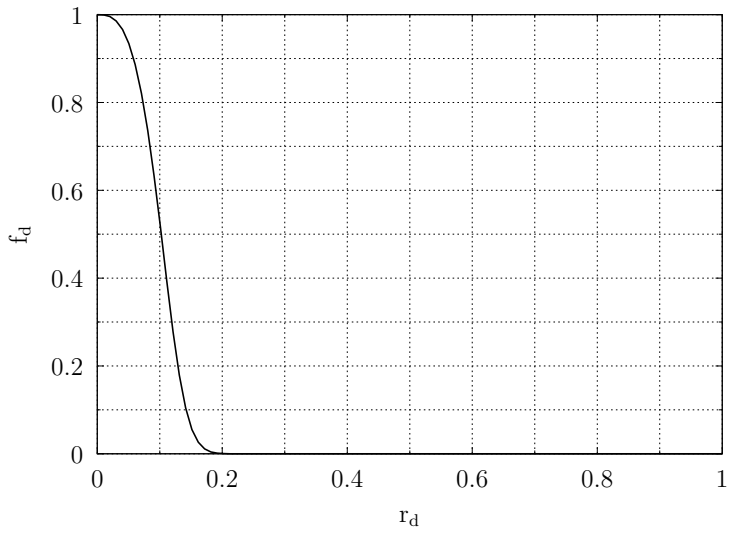

Figure 2.5: *A plot of the shielding function f_d in terms of the r_d parameter.*

Chapter 3

The Aeroacoustic Analysis

3.1 Acoustic Analogies

In the acoustic analogies, the Navier-Stokes equations are rearranged in such a way that a wave operator, describing the propagation of the acoustic variable, is on the left-hand side of the equation and the quantities supposed to form the sources of the acoustic field are on the right-hand side, as

$$Lf = g \tag{3.1}$$

where $L = \frac{1}{\alpha_\infty^2}\frac{\partial^2}{\partial t^2} - \frac{\partial^2}{\partial x_i^2}$ is the wave operator, α_∞ the speed of sound, f the acoustic field variable and g the sources for field f. Outside of the source region, the right-hand side is zero and the field there obeys the homogeneous wave equation. In order to solve the acoustic analogy and compute the acoustic field, the source term g should be known *a priori*. Typically, this term is computed by the use of a CFD method.

3.1.1 Lighthill Equation

The first step in the field of aeroacoustics was done by Lighthill, with his first paper [20], in which he derived a PDE for the propagation of sound waves in a quiescent unbounded medium. It's derivation starts with the Navier-Stokes equations,

rearranging them to get a single equation for an acoustic variable

$$\frac{\partial^2 \rho'}{\partial t^2} - a_\infty^2 \frac{\partial^2 \rho'}{\partial {x_i}^2} = \frac{\partial^2 T_{ij}}{\partial x_i \partial x_j} \tag{3.2}$$

where $T_{ij} = \rho u_i u_j - \tau_{ij} + (p - a_\infty^2 \rho)\delta_{ij}$ represents the Lighthill tensor, in which ρ' stand for perturbation of density, p the pressure, τ_{ij} the viscous stresses, u_i the velocity and δ_{ij} the Kronecker delta. During the derivation of the above equation, no assumptions where made, and hence, it includes all the physics.

In a real world case where the medium is not quiescent, one has to "replace" the real flow field with a uniform medium at rest, where all the disturbances are represented by equivalent volume sources described by the right-hand side of eq. 3.2. Then, eq. 3.2 accepts an analytical solution and the density perturbations for a receiver in $\vec{x}$, at time t is given by

$$\rho(\vec{x}, t) - \rho_0 = \frac{1}{4\pi\alpha_\infty^2} \int_V \frac{1}{r} \frac{\partial^2 T_{ij}|_\tau}{\partial y_i \partial y_j} dV(\vec{y}) \tag{3.3}$$

where $T_{ij} = T_{ij}(\vec{y}, \tau)$, $r = |\vec{x} - \vec{y}|$ and $\tau = t - r/a_\infty$ is the retarded time. The integral in the above equation is taken over all the volume sources domain $V(\vec{y})$, $\vec{y}$ being the source location. Fig. 3.1 illustrates the above concept of the Lighthill's integral.

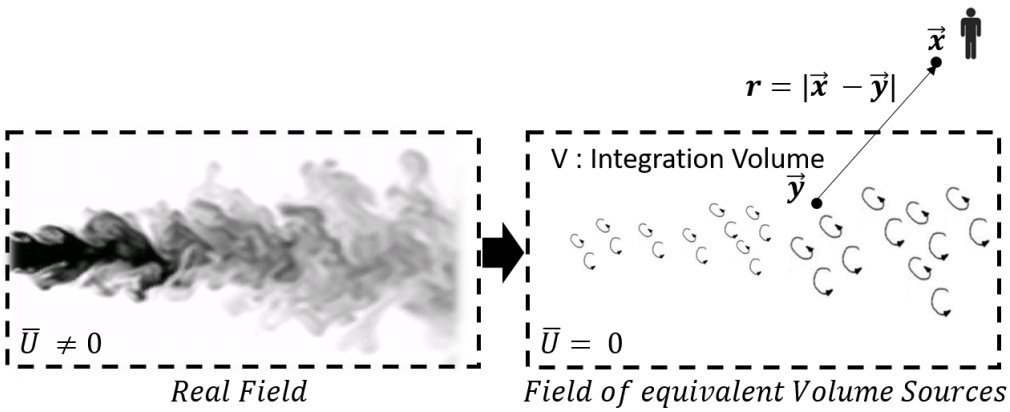

Figure 3.1: *Illustration of the Lighthill's Integral. The real field is replaced by a quiescent medium with a distribution of volume noise sources. The acoustic variable on a receiver at $\vec{x}$ results from an integration of the sources into volume V.*

3.1.2 Curle's Equation

If present, solid surfaces will alter the sound generation and radiation. The surfaces may act as sources of sound, changing the radiating characteristics of the flow. The

first attempt to find a theory for these phenomena was published by Curle [21] and Ffowcs-Williams and Hawkings [22] who extended Curle's theory to account for surfaces in arbitrary motion. According to Curle's theory, the general solution to eq. 3.2 on a bounded by solid surfaces domain is

$$\rho(\vec{x},t)-\rho_0=\frac{1}{4\pi\alpha_\infty^2}\frac{\partial^2}{\partial x_i\partial x_j}\int_V\frac{T_{ij}|_\tau}{r}dV(y)-\frac{1}{4\pi\alpha_\infty^2}\frac{\partial}{\partial x_i}\int_{S_W}\frac{n_j}{r}(p\delta_{ij}-\tau_{ij})|_\tau dS(y) \tag{3.4}$$

where n, the normal unit vector of the solid surface S_W and the rest nomenclature is the same used in eq. 3.3.

Similar to the procedure followed in the Lighthill's equation, the flow field can be replaced by an equivalent medium at rest ($\overline{U}=0$), consisted of a volume and a surface source distribution, as can be seen in fig. 3.2. The volume integral in eq. 3.4 is taken over the volume containing the equivalent volume sources, and the surface integral over the rigid surface of the body, consisted of surface sources.

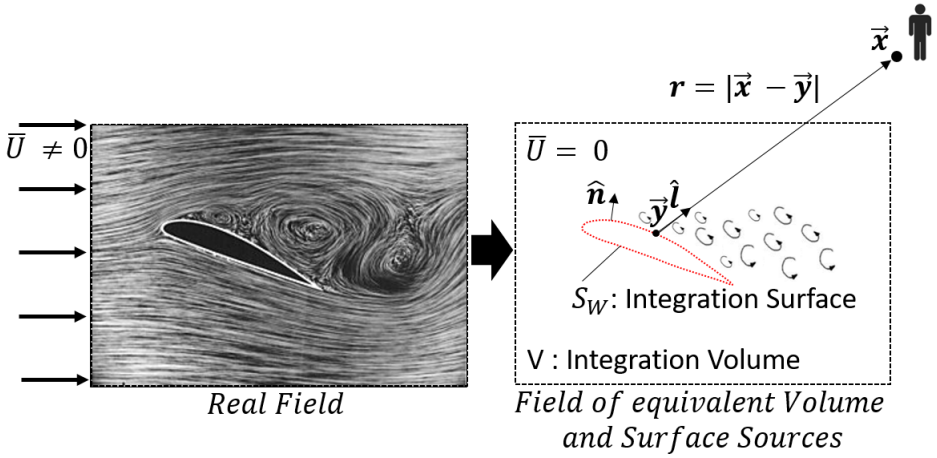

Figure 3.2: *Illustration of Curle's Integral. The real field is replaced by a quiescent medium with a distribution of volume and surface noise sources. The acoustic variable at a receiver at $\vec{x}$ results from an integration of the sources at volume V and surface S_W.*

It is important to notice that, in Curle's theory, the equivalent volume and surface sources, incorporate not only the generation of sound but also its convection with the flow, its propagation with variable speed, its dissipation by conduction and viscosity and the effect of reflection and refraction at solid boundaries [21].

Curle's equation (eq. 3.4) can be manipulated further in a way that the derivatives are inside the integral and with temporal derivatives of the source term instead of spatial ones [23],[24]. For a function $f(\tau)$, where $\tau = t - r/\alpha_\infty$ is the retarded time,

the spatial derivative can be converted to a temporal one by

$$\frac{\partial}{\partial x_i}\left[\frac{f(\tau)}{r}\right] = -\frac{\partial r}{\partial x_i}\left[\frac{\dot{f}}{\alpha_\infty r} + \frac{f}{r^2}\right]_\tau = -l_i\left[\frac{\dot{f}}{\alpha_\infty r} + \frac{f}{r^2}\right]_\tau \tag{3.5}$$

where the subscript $|_\tau$ or $[\quad]_\tau$, when used, means computation at the retarded time, l_i the unit vector pointing from the source location $\vec{y}$ to the receiver location $\vec{x}$, and the dot on top of a variable $\dot{f}$ means temporal derivative.

► **Proof of eq. 3.5**

$$\begin{aligned}
\frac{\partial}{\partial x_i}\left[\frac{f(\tau)}{r}\right] &= \frac{1}{r}\frac{\partial}{\partial x_i}\big[f(\tau)\big] + f(\tau)\frac{\partial}{\partial x_i}\left(\frac{1}{r}\right) \\
&= \frac{1}{r}\frac{\partial \tau}{\partial x_i}\frac{\partial f(\tau)}{\partial \tau} + f(\tau)\left(-\frac{1}{r^2}\right)\frac{\partial r}{\partial x_i} \\
&= \frac{1}{r}\left(-\frac{1}{\alpha_\infty}\frac{\partial r}{\partial x_i}\right)\frac{\partial f(\tau)}{\partial \tau} - \frac{\partial r}{\partial x_i}\frac{1}{r^2}f(\tau) \\
&= -\frac{\partial r}{\partial x_i}\left[\frac{\dot{f}(\tau)}{\alpha_\infty r} + \frac{f(\tau)}{r^2}\right] = -l_i\left[\frac{\dot{f}}{\alpha_\infty r} + \frac{f}{r^2}\right]_\tau \blacktriangleleft
\end{aligned}$$

Based on the above, Curle's equation (eq. 3.4) can be re-written as

$$\begin{aligned}
\rho(\vec{x},t) - \rho_0 &= \frac{1}{4\pi}\frac{\partial}{\partial x_i}\int_V -l_j\left[\frac{\dot{T}_{ij}}{\alpha_\infty r} + \frac{T_{ij}}{r^2}\right]_\tau dV(y) - \frac{1}{4\pi}\int_{S_W} -l_i n_j\left[\frac{\dot{p}\delta_{ij} - \dot{\tau}_{ij}}{\alpha_\infty r} + \frac{p\delta_{ij} - \tau_{ij}}{r^2}\right]_\tau dS(y) \\
&= \frac{1}{4\pi}\int_V \left(l_i l_j\left[\frac{\ddot{T}_{ij}}{\alpha_\infty^2 r} + 2\frac{\dot{T}_{ij}}{\alpha_\infty r^2} + 2\frac{T_{ij}}{r^3}\right]_\tau - \frac{\partial l_j}{x_i}\left[\frac{\dot{T}_{ij}}{\alpha_\infty r} + \frac{T_{ij}}{r^2}\right]_\tau\right) dV(y) \\
&\quad + \frac{1}{4\pi}\int_{S_W} l_i n_j\left[\frac{\dot{p}\delta_{ij} - \dot{\tau}_{ij}}{\alpha_\infty r} + \frac{p\delta_{ij} - \tau_{ij}}{r^2}\right]_\tau dS(y)
\end{aligned} \tag{3.6}$$

The term $\partial l_j/\partial x_i$ is expanded as

$$\frac{\partial l_j}{\partial x_i} = \frac{\partial}{\partial x_i}\left[\frac{x_j - y_j}{r}\right] = \frac{\delta_{ij} - l_i l_j}{r} \tag{3.7}$$

Inserting this into eq. 3.6 yields

$$\begin{aligned}
\rho(\vec{x},t) - \rho_0 &= \frac{1}{4\pi}\int_V \left[\frac{l_i l_j}{\alpha_\infty^2 r}\ddot{T}_{ij} + \frac{3l_i l_j - \delta_{ij}}{\alpha_\infty r^2}\dot{T}_{ij} + \frac{3l_i l_j - \delta_{ij}}{r^3}T_{ij}\right]_\tau dV(y) \\
&\quad + \frac{1}{4\pi}\int_{S_W} l_i n_j\left[\frac{\dot{p}\delta_{ij} - \dot{\tau}_{ij}}{\alpha_\infty r} + \frac{p\delta_{ij} - \tau_{ij}}{r^2}\right]_\tau dS(y)
\end{aligned} \tag{3.8}$$

3.1.3 Curle's Surface Integral Method

For a low Mach number flow, even for a car cruising at 120 km/h i.e. Mach $\cong 0.09$, an incompressible solver can be used to compute the source terms accounted on Curle's integral (eq. 3.8). For such a case, as stated in section 1.2.1 dipole sources, represented by the surface integral, are more dominant than the quadrupole ones, given by the volume integral. Also, if the Reynolds number is high, the pressure terms are more important than the stresses. Based on the above, and the high storage cost of saving the volume sources and viscous stresses, only the surface integral and, inside that, the pressure and its time derivative are accounted for in the Curle's integral method implemented. If the flow is isentropic in the region of the receiver $\vec{x}$, the acoustic variable in equation 3.4 can be changed from density to pressure, as $\rho(\vec{x},t) - \rho_0 = (p(\vec{x},t) - p_0)/\alpha_\infty^2$ and as a result Curle's surface integral equation is given by

$$p(\vec{x},t) - p_0 = \frac{1}{4\pi} \int_{S_W} l_i n_i \left[\frac{\dot{p}}{\alpha_\infty r} + \frac{p}{r^2} \right]_\tau dS(y) \tag{3.9}$$

Spatial Discretization

Eq. 3.9 can be discretized as

$$p(\vec{x},t) - p_0 = \sum_{faces} \frac{1}{4\pi} \int_{face} l_i n_i \left[\frac{\dot{p}}{\alpha_\infty r} + \frac{p}{r^2} \right]_\tau dS(y) \tag{3.10}$$

where three-dimensional space and the solid surfaces are also discretized and consisted of volume elements (cells) and surface elements (faces), respectively. In a CFD cell-centred fashion, the discrete flow solution is stored at the centers of the cells for volume and at the center of the faces for surface elements. (fig. 3.3)

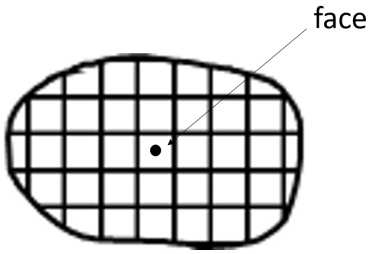

Figure 3.3: *Illustration of a discretized body surface, consisted of surface elements (faces).*

If the surface discretization is fine enough, the flow variables and distance r can be

assumed constant over a face's center and eq. 3.10 results to

$$p(\vec{x},t) - p_0 = \sum_{faces} \frac{l_i n_i A_f}{4\pi} \left[\frac{\dot{p}_{f.c.}}{\alpha_\infty r_c} + \frac{p_{f.c.}}{r_c^2} \right]_\tau \tag{3.11}$$

where A_f the face area, r_c the distance from the receiver to the center of the face, and $p_{f.c.}$, $\dot{p}_{f.c.}$ the pressure and its time derivative on the face's center respectively.

Time Discretization

Eq. 3.11, can be written as

$$p(\vec{x},t) - p_0 = \sum_\kappa f^{(\kappa)}(\tau) \tag{3.12}$$

$$f^{(\kappa)}(\tau) = \frac{l_i n_i A_f}{4\pi} \left[\frac{\dot{p}_{f.c}}{\alpha_\infty r_c} + \frac{p_{f.c.}}{r_c^2} \right]_\tau$$

where κ sums over all faces that radiate sound, $f^{(\kappa)}$ (computed at the retarded time $\tau = t_n - r/\alpha_\infty$) is the source term of that element and $t_n = n\Delta t$, $n \in \mathbb{Z}^*$ the discretized time of the receiver. In the same manner, the discretized time of the source is $\tau_l = l\Delta\tau$, $l \in \mathbb{Z}^*$, where $\mathbb{Z}^*$ denotes the set of non-negative integers. For each element, the contribution to the noise at the receiver is

$$\Delta p^{(\kappa)}(\vec{x},t_n) = f^{(\kappa)}(\tau) = f^{(\kappa)}(t_n - \frac{r}{\alpha_\infty}) \tag{3.13}$$

The source term Δp_n will only be available at the discrete times of the source τ_l and an interpolation in time for $t_n - r/\alpha_\infty \in (\tau_l, \tau_{l+1}]$, yields

$$\Delta p_n^{(\kappa)} = \left[1 - \frac{\left(n\Delta t - \frac{r}{\alpha_\infty}\right) - \tau_l}{\Delta\tau} \right] f_l^{(\kappa)} + \left[\frac{\left(n\Delta t - \frac{r}{\alpha_\infty}\right) - \tau_l}{\Delta\tau} \right] f_{l+1}^{(\kappa)} \tag{3.14}$$

where $\Delta p_n^{(\kappa)} = \Delta p^{(\kappa)}(\vec{x},t_n)$ and $f_l^{(\kappa)} = f^{(\kappa)}(\tau_l)$. It is convenient to choose $\Delta t = \Delta\tau$; then

$$\Delta p_n^{(\kappa)} = \left[1 - \left(n - \frac{r}{\alpha_\infty \Delta t} - l \right) \right] f_l^{(\kappa)} + \left[n - \frac{r}{\alpha_\infty \Delta t} - l \right] f_{l+1}^{(\kappa)} \tag{3.15}$$

The choice of $\Delta t = \Delta\tau$ combined with relation $t_n - r/\alpha_\infty \in (\tau_l, \tau_{l+1}]$ lead to $l < n - r/(\alpha_\infty \Delta t) \leq l+1$ or similarly $l + r/(\alpha_\infty \Delta t) < n \leq l + 1 + r/(\alpha_\infty \Delta t)$ and, hence, when using a floor function $R^-(\Theta)$, that gives as output the greatest integer less

than or equal to Θ, $\Theta \in \mathbb{R}$,

$$n = R^{-}(l + 1 + \Theta) = l + 1 + R^{-}(\Theta) \tag{3.16}$$

where $\Theta = r/(\alpha_\infty \Delta t)$. Based on that, time interpolation eq 3.15 yields

$$\Delta p_n^{(\kappa)} = \left[\Theta - R^{-}(\Theta)\right] f_l^{(\kappa)} + \left[1 - (\Theta - R^{-}(\Theta))\right] f_{l+1}^{(\kappa)} \tag{3.17}$$

The concluding remark of eq. 3.17 is that the element κ at source time l contributes to the signal at the observer location only at times t_n and t_{n-1} as

$$\Delta p_n^{(\kappa)} = [\Theta - R^{-}(\Theta)] f_l^{(\kappa)}$$

$$\Delta p_{n-1}^{(\kappa)} = [1 - (\Theta - R^{-}(\Theta))] f_l^{(\kappa)}$$

The main advantage of this is that the retarded time signals can be computed while running the code without massive storage of data.

3.2 Exterior Noise Power

Based on the definition of sound power, eq. 1.6, and utilizing CFD acquired data, the Exterior Noise Power (ENP) method have been developed in [25]. The concept of using the radiated power, as an integral of the acoustic intensity, to rank machines regarding their radiating noise is not new; it is a usual experimental practice [26].

Simplifying Curle's equation (eq 3.9) for a far-field receiver at $\vec{x}$, neglecting terms for which the distance between the receiver and the source scales with $1/r^2$, the acoustic pressure is given by:

$$p_\alpha(\vec{x}, t) = p(\vec{x}, t) - p_0 = \frac{1}{4\pi} \int_{S_W} l_i n_i \left[\frac{\dot{p}(\vec{y}, t - r/\alpha_\infty)}{\alpha_\infty r}\right] dS(\vec{y}) \tag{3.18}$$

where y_i is a point on the vehicle surface, r the distance between $\vec{x}$ and $\vec{y}$, α_∞ the speed of sound, S_W the vehicle surface and n the normal vector on that surface. Also, a twice repeated index means summation according to the Einstein convention.

In the far-field, the propagation of acoustic waves can be regarded as locally planar. The acoustic intensity for planar waves is given by:

$$I = \frac{p_\alpha(\vec{x}, t)^2}{\rho \alpha_\infty} \tag{3.19}$$

The Exterior Noise Power around the vehicle is defined as the acoustic power radiated to the farfield and can be calculated as an integral of the acoustic intensity over a closed surface that encloses the vehicle at large distance.

$$W(t) = \oiint \frac{p_\alpha(\vec{x},t)^2}{\rho\alpha_\infty} dS_{Cl}(\vec{x}) \tag{3.20}$$

where $\oiint$ denotes this integration over a closed surface at the farfield.

Choosing this surface to be a sphere with its origin on the center of gravity of the car as seen in fig. 3.4 and replacing the p_a inside the integral by its Curle's representation (eq. 3.18) the ENP is given by

$$\begin{aligned} W(t) = \frac{1}{16\pi^2\rho c^3} \oiint \Bigg(\int_{S_W} \frac{l_i}{r} \dot{p}(\vec{y}, t - r/\alpha_\infty) n_i dS(\vec{y}) \Bigg) \\ \Bigg(\int_{S_W} \frac{l'_j}{r'} \dot{p}(\vec{y'}, t - r'/\alpha_\infty) n_j dS(\vec{y'}) \Bigg) dS_{Cl}(\vec{x}) \end{aligned} \tag{3.21}$$

where y and y' measurement points on the surface of the car. The outer integral integrates over the closed surface surrounding the car and the two surface integrals inside that, integrate on the vehicle surface. For far-field positions, the car can be regarded as a point; then, the approximation $l_i l'_j = (x_i - y_i)(x_j - y'_j)/r/r' \approx x_i x_j / r^2$ stands and ENP takes the form

$$W(t) = \frac{1}{16\pi^2\rho\alpha_\infty^3} \oiint \int_{S_W} \int_{S_W} \frac{x_i x_j}{r^4} \dot{p}(\vec{y},\tau) \dot{p}(\vec{y'},\tau) n_i n'_j dS(\vec{y'}) dS(\vec{y}) dS_{Cl}(\vec{x}) \tag{3.22}$$

where $\tau = t - r/\alpha_\infty$ the retarded time. A local area around each measurement point y can be defined, for which the surface pressure fluctuation at each measurement point y' belonging to that area, correlates with the surface pressure fluctuation of the measurement point y. This area is referred to as correlation area, $S(y)_{correlation}$. Based on measurements in turbulent flows, this area in high frequency range is very small and the following approximations are established:

$$\begin{aligned} \vec{y'} &\approx \vec{y} \\ n'_i &\approx n_i \\ x'_i &\approx x_i \\ \dot{p}(\vec{y'},\tau) &\approx \dot{p}(\vec{y},\tau) \end{aligned}$$

if the measurement point y' belongs to the correlation area of point y. Using the above relationships and applying time-averaging, the average acoustic power is given

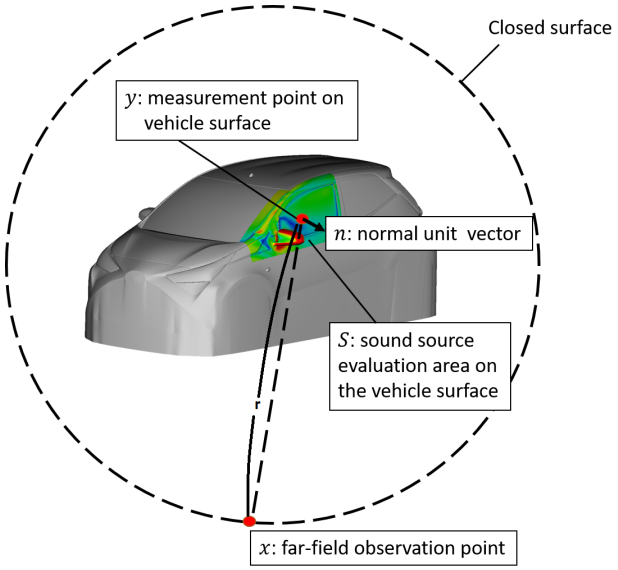

Figure 3.4: *A view of the spherical surface enclosing the car at the farfield.*

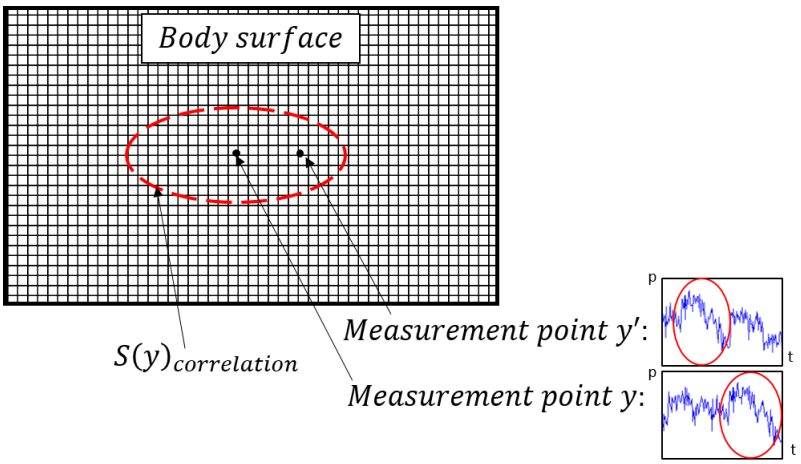

Figure 3.5: *Illustration of the correlation area $S(y)_{correlation}$ at the measurement point y. The surface pressure fluctuation of each point, that belongs to $S(y)_{correlation}$ (red area) correlates with the surface pressure fluctuation of y.*

by

$$\overline{W(t)} = \frac{1}{16\pi^2\rho\alpha_\infty^3} \oiint_{S_W} \frac{(x_i n_i)^2}{r^4} \overline{[\dot{p}(y,\tau)]^2} S(\vec{y})_{correlation} dS(\vec{y}) dS_{Cl}(\vec{x}) \tag{3.23}$$

The above equation (eq. 3.23) is based on the fact that time-averaging of uncorrelated signals equals zero. Also, considering that the enclosing surface is a sphere,

$$\oiint \frac{(x_i n_i)^2}{r^4} dS_{Cl}(x) = \frac{4\pi}{3} \tag{3.24}$$

Substituting eq. 3.24 into eq. 3.23 results in

$$\overline{W(t)} = \frac{1}{12\pi\rho\alpha_\infty^3}\int_{S_W} \overline{[\dot{p}(\vec{y},\tau)]^2} S(\vec{y})_{correlation} dS(\vec{y}) \tag{3.25}$$

In order to avoid computation at retarded time and because wind noise is often discussed in frequency bands, the ENP equation can be transformed into the frequency domain, in which taking advantage of the Fourier transform identity for time derivative

$$\overline{[\dot{p}(y,\tau)]^2} = 4\pi^2 f^2 P(\vec{y})_f^2 \tag{3.26}$$

in which $P(\vec{y})_f^2$ the power spectrum of the surface pressure fluctuations at measurement point y, yields:

$$W_f = \int_{S_W} \frac{\pi f^2}{3\rho\alpha_\infty^3} P(\vec{y})_f^2 S(\vec{y})_{correlation} dS(\vec{y}) \tag{3.27}$$

The integrand quantity is denoted as the exterior noise power distribution (ENPD) within a frequency band and is given by:

$$I_f(\vec{y}) = \frac{\pi f^2 P(\vec{y})_f^2 S(\vec{y})_{correlation}}{3\rho\alpha_\infty^3} \tag{3.28}$$

Based on that, the ENP index on a certain frequency band comes up as the integral of the ENPD over the vehicle surface.

$$\overline{W}_f = \int_{S_W} I_f(\vec{y}) dS(\vec{y}) \tag{3.29}$$

The calculation of the new index requires the detailed information of the correlation area of surface pressure fluctuations at all measurement points. This information can be computed analytically utilizing the coherence function

$$coh(\vec{y},\vec{y'})_f = \frac{|G_{yy'}|_f^2}{P(\vec{y})_f^2 P(\vec{y'})_f^2} \tag{3.30}$$

where $|G_{yy'}|_f^2$ the cross-correlation of the surface pressure fluctuation signal between measurement point y and y' and $P(\vec{y})_f^2$,$P(\vec{y'})_f^2$ the power spectrum of surface pressure fluctuation at measurement point y and y' respectively. From the definition of the coherence function (eq. 3.30), $0 \leq coh(\vec{y},\vec{y'})_f \leq 1$ ($coh(\vec{y},\vec{y'})_f = 1$ meaning perfectly correlated and $coh(\vec{y},\vec{y'})_f = 0$ uncorrelated), it is clear that the definition of $S(\vec{y})_{correlation}$ in that manner is computationally prohibitive, because this would

require to compute eq. 3.30 for every y, with every other measurement point y' at the surface.

To simplify the computations, a work-around is to model the correlation area. If the correlation area be modeled as a disk of diameter $L(\vec{y})_{correlation}$, the approximation below is made for the correlation area:

$$S(\vec{y})_{correlation} \cong \frac{\pi L(\vec{y})^2_{correlation}}{4} \cong \frac{\pi k^2 \overline{U}(\vec{y})^2}{4f^2} \tag{3.31}$$

where $\overline{U}$ is the convective mean velocity in the neighborhood of measurement point y, k a constant f the frequency in which we regard the correlation area. The basis for the approximation is the fact that a signal of surface pressure fluctuation is shifted by $\overline{U}$. The coherence function (eq. 3.30) can be neglected approximately at $y' = \pm L(\vec{y})_{correlation}$.

Finally, the ENPD and ENP are respectively:

$$I_f(\vec{y}) = \frac{\pi^2 k^2 P(\vec{y})^2_f \overline{U}(\vec{y})^2}{12\rho\alpha^3_\infty} \tag{3.32}$$

$$\overline{W}_f = \int_{S_W} \frac{\pi^2 k^2 P(\vec{y})^2_f \overline{U}(\vec{y})^2}{12\rho\alpha^3_\infty} dS(\vec{y}) \tag{3.33}$$

According to eq. 3.33, for a frequency band with central frequency f, the ENP emanating from a part of the solid body (car), is computed as an integral of the Power Spectrum of surface pressure fluctuation in that frequency band, scaled by the local mean convection velocity.

3.2.1 Computational Procedure

From eq. 3.33, the computation of the ENP index requires three quantities to be known *a priori*:

1. $P(y)^2_f$: The Power Spectrum of the unsteady pressure fluctuation on the surface of the car.
2. $\overline{U(y)}$: The mean local convective velocity, called mean adjacent to the wall velocity.
3. k : The constant k, used to calibrate the model which approximates the correlation area $S_{correlation}$.

The way these quantities are accounted for in the method implemented in OpenFOAM is presented in the following paragraphs.

Power Spectrum of the Unsteady Pressure Fluctuations

The unsteady pressure fluctuations on the car surfaces are predicted by the DDES-SA turbulence model of OpenFOAM described in 2.5.1. An FFT algorithm was implemented in OpenFoam based on the library LIBROW [27], and Welch's method was used to compute the Power Spectrum [28]. The solver developed is also able to integrate the spectrum frequency bands to get the $1st$ or $1/3rd$ octave band spectrum.

Mean Local Convective Velocity

As a first representation of convective velocity, the mean velocity of the first off-wall cell, namely $U_{Adjacent}$ was used in the programmed software. Although this choice is an easy solution, it makes the adjacent velocity dependent on the mesh size and a different representation needs to be tested.

Coefficient k

Solving eq. 3.31 for the constant k yields

$$k = \sqrt{\frac{4f^2 S(y)_{correlation}}{\pi \overline{U}(y)^2}} \tag{3.34}$$

where the $S(y)_{correlation}$ is calculated analytically as the area around y that the coherence function eq. 3.30 is smaller than 0.5. In a simplified manner, the coefficient k can be chosen as $k = 1$ to the extent that this is just a scaling factor, affecting only the absolute value of ENP and not the relative contribution of the different parts.

The procedure followed in order to compute the ENP index on different bands and the relative contribution of each part is presented in figure 3.6. According to that, as a first step an unsteady simulation is conducted with the DDES-SA turbulence model of OpenFOAM. When the solution is statistically converged, the unsteady surface pressure fluctuations on the area of interest are stored and the velocity field is averaged. As a post-process, the unsteady pressure fluctuation signal is transformed to the frequency domain, through an FFT algorithm and the narrow bands are integrated in the $1st$ or $1/3rd$ octave bands. The ENPD sound intensity

map is computed over the surface of the car from eq. 3.32 and, finally, through its integration per part and frequency band a table describing the ENP contribution of each part is acquired.

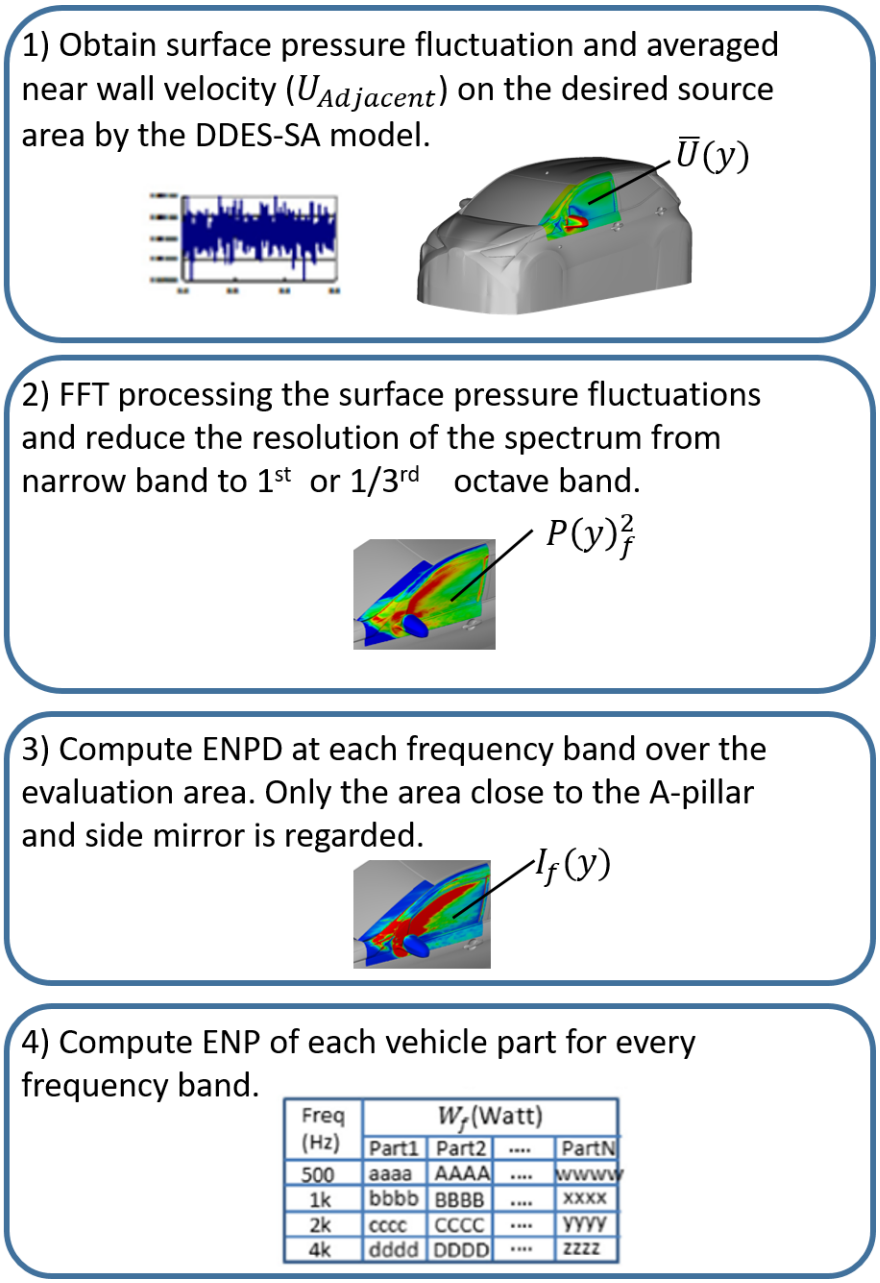

Figure 3.6: *ENP calculation workflow.*

Chapter 4

Applications

4.1 The "Generic Mirror on a Flat Plate" case

In this chapter, an unsteady simulation is implemented in the case of a generic side-mirror on a flat plate, as proposed in [29], and the acoustic pressure signal is computed in some distant receivers utilizing the Curle's surface integral method. In addition, pressure fluctuations on the surface of the mirror and the flat plate are compared with experimental and simulation data. The simulation and the experimental data are extracted from [29]. Simulation data in [29] was acquired using a commercial code, with the DES turbulence model, a second-order upwind biased scheme for the momentum equation, CFD mesh hex-dominated with $5.83 \cdot 10^6$ elements and the simulation was run for 0.5 sec, and then for another 0.52 s to store the unsteady pressure fluctuations, later used in the Curle's integral. In these runs the timestep was $\Delta t = 2 \cdot 10^{-5}$ sec.

4.1.1 Case Setup

The mirror geometry is a simplified one, built from a half cylinder with a quarter sphere on top and is placed on a flat plate. The sphere's and the cylinder's diameter D is the same. Fig. 4.1 shows the geometry of the mirror and table 4.1 the characteristics of the simulation. The surface pressure fluctuations are monitored in 7 sensor positions on the mirror's and plate's surface (fig. 4.2) and the acoustic pressure are computed at 5 microphone positions (fig. 4.3). The exact location of the sensors and the microphones are tabulated in Appendix B.

Variable	Value
Diameter	$D = 0.2m$
Velocity	$U = 39\frac{m}{s}$
Reynolds Number	$Re_D = 5.2 \cdot 10^5$

Table 4.1: *Generic Mirror on a Flat Plate. Characteristics of the geometry and data of the simulation.*

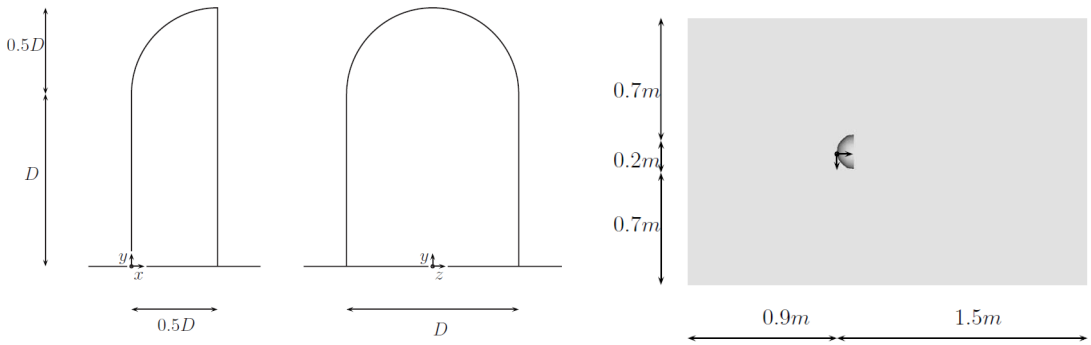

(a) *Side and front view of the mirror* **(b)** *Top view of the mirror and plate*

Figure 4.1: *Generic Mirror on a Flat Plate. Mirror and plate geometry. From [29].*

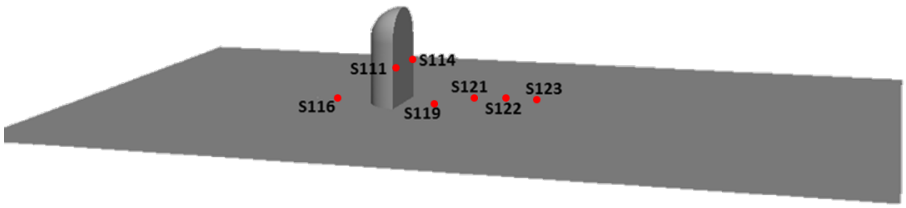

Figure 4.2: *Generic Mirror on a Flat Plate. Locations of the pressure sensors on the mirror's and plate's surface.*

4.1.2 CFD Mesh

The computational domain is rectangular with inlet 30D wide x 15D high, 15D upstream the front side of the mirror and outlet 30D downstream (fig. 4.4). Three refinement boxes have been placed close to the mirror and in its wake in order to accurately predict the flow field while keeping the number of the cells low. The mesh consists of $6.3 \cdot 10^6$ polyhedral cells with 5 prism layers on the mirror's and plate's surface. The average $y^+ = 27.3$ and the max $y^+ = 42.2$ on the mirror surface and average $y^+ = 63.7$ and max $y^+ = 118.3$ on the plate' s surface, allow the use of wall functions with the Spalart-Allmaras turbulence model, both in the steady and unsteady cases. The y^+ contours on the mirror' s and plate' s surface are presented in fig. 4.5.

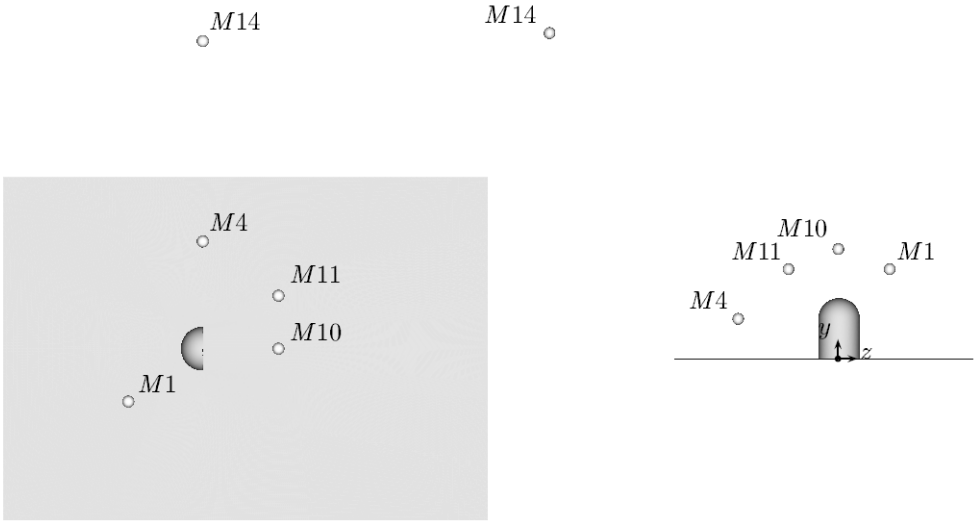

Figure 4.3: *Generic Mirror on a Flat Plate. Locations of the microphones on which acoustic pressure will be computed. From [29].*

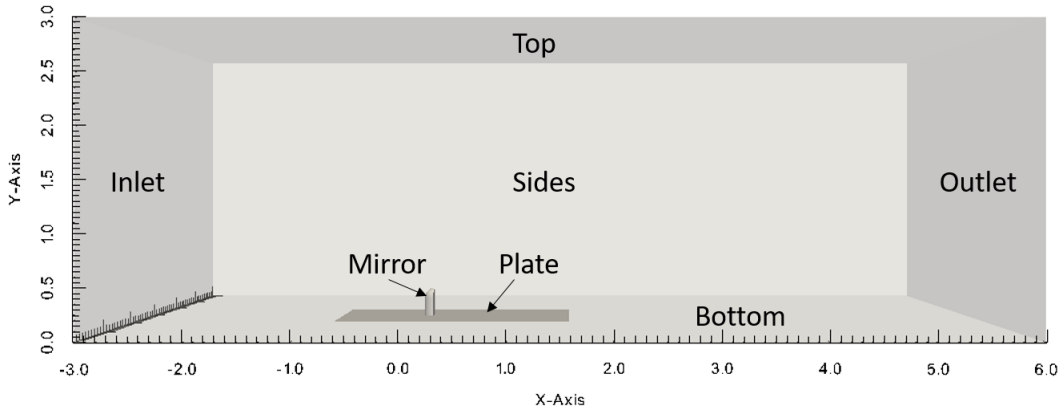

Figure 4.4: *Generic Mirror on a Flat Plate. View of the computational domain.*

4.1.3 Boundary Conditions

The boundary conditions for the velocity and pressure are presented in table 4.2.

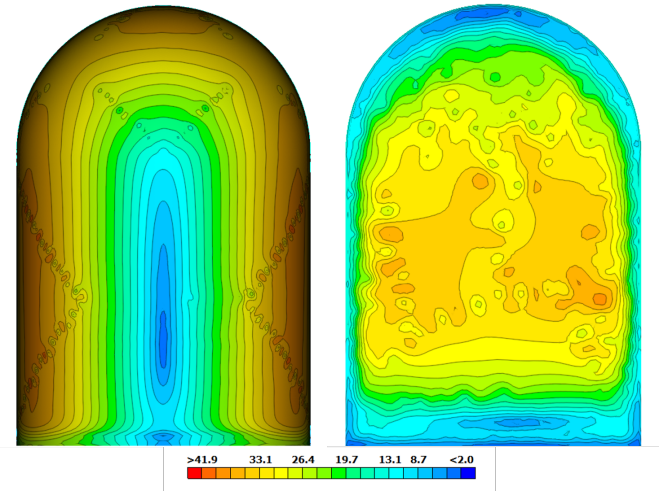

(a) *Mirror's front and back view*

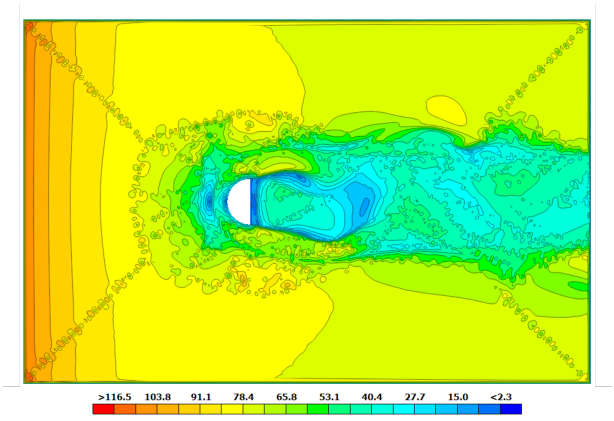

(b) *Plate*

Figure 4.5: *Generic Mirror on a Flat Plate. Computation based on RANS. Three different y^+ views.*

Boundary Conditions		
Boundary	**Velocity**	**Pressure**
Inlet	Dirichlet $\vec{U} = (39, 0, 0)m/s$	zero Neumann
Outlet	zero Neumann	zero Dirichlet
Mirror	zero Dirichlet	zero Neumann
Plate	zero Dirichlet	zero Neumann
Sides,Top	symmetry	symmetry
Bottom	Dirichlet $\vec{U} = (39, 0, 0)m/s$	zero Neumann

Table 4.2: *Generic Mirror on a Flat Plate. Boundary conditions for pressure and the velocity.*

4.1.4 Aerodynamic Results

Steady RANS simulation

First, a steady simulation utilizing the Spalart-Allmaras high-Re turbulence model was conducted in order to acquire a physical initialization. The convergence of the drag coefficient with the solver iterations is presented in fig. 4.6 and the dimensionless residuals in fig. 4.7. As seen in both figures, the convergence is moderate and the residuals fluctuate and, most probably, this is an indication of unsteadiness. The deviation of the drag from its mean value after 18000 iterations is less than 0.05% of the mean value and the residuals of the governing equation have reduced by more than 3 orders of magnitude. A mean value of $C_D = 0.5243$ is computed by averaging the drag coefficient starting from iteration 16000, when the solution has converged, till iteration 18710.

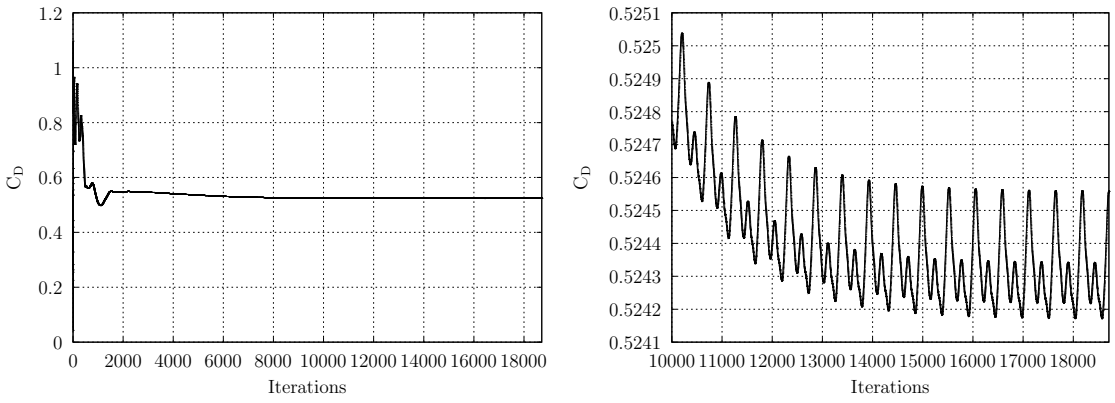

(a) *Total* **(b)** *Last iterations*

Figure 4.6: *Generic Mirror on a Flat Plate. Computation based on the RANS equations. Convergence of the drag coefficient in terms of the number of iterations of the steady solver.*

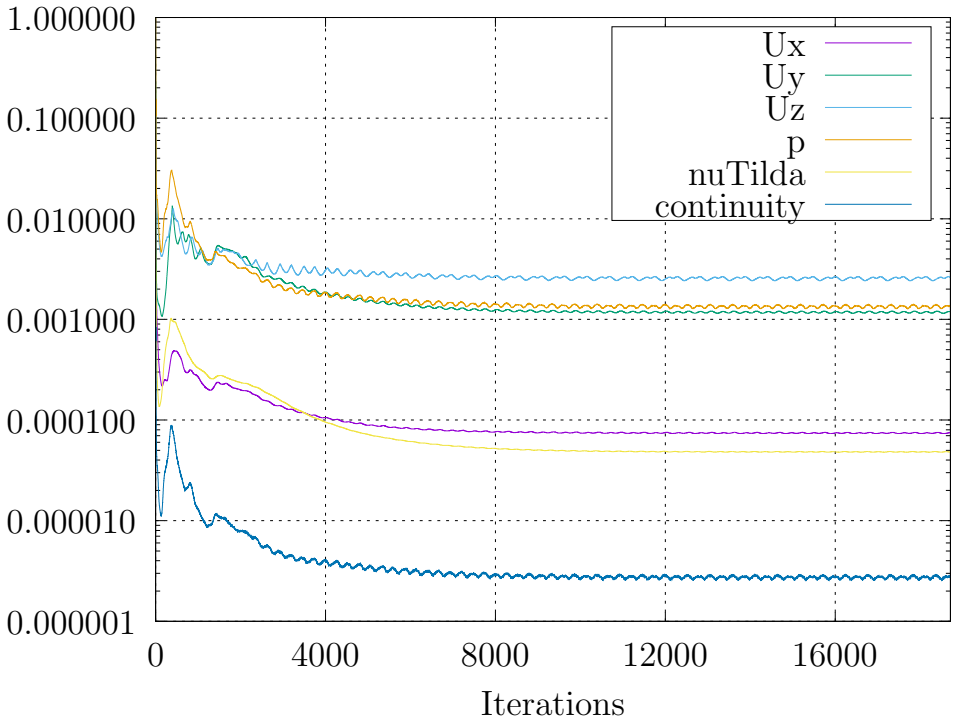

Figure 4.7: *Generic Mirror on a Flat Plate. Computation based on the RANS equations. Dimensionless residuals of the governing equations.*

URANS simulation

Due to the debatable convergence of the RANS simulation, results are not dependable and the URANS model is tried as well. Fig. 4.8 presents the evolution the dimensionless residuals, which seems to converge more over simulation time and, thus, the computed drag value (fig. 4.9) is expected to be closer to the reference value from [29]. URANS could be used to acquire the necessary surface pressure fluctuations although the unsteady phenomena are weakly described in the solution.

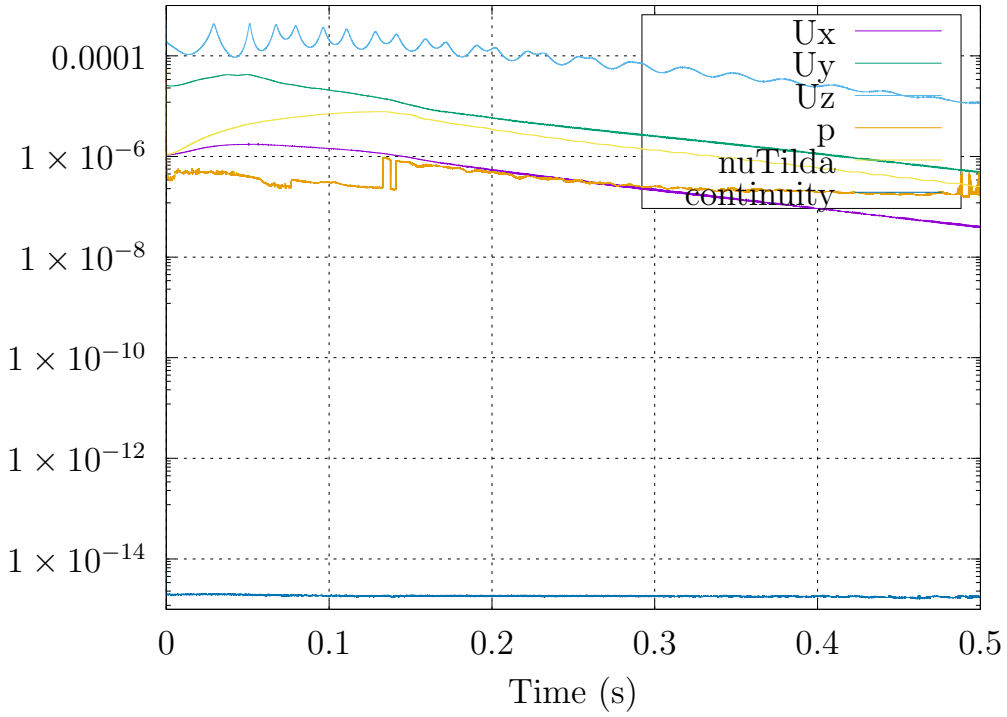

Figure 4.8: *Generic Mirror on a Flat Plate. Computation based on the URANS equations. Evolution of dimensionless residuals of the governing equations.*

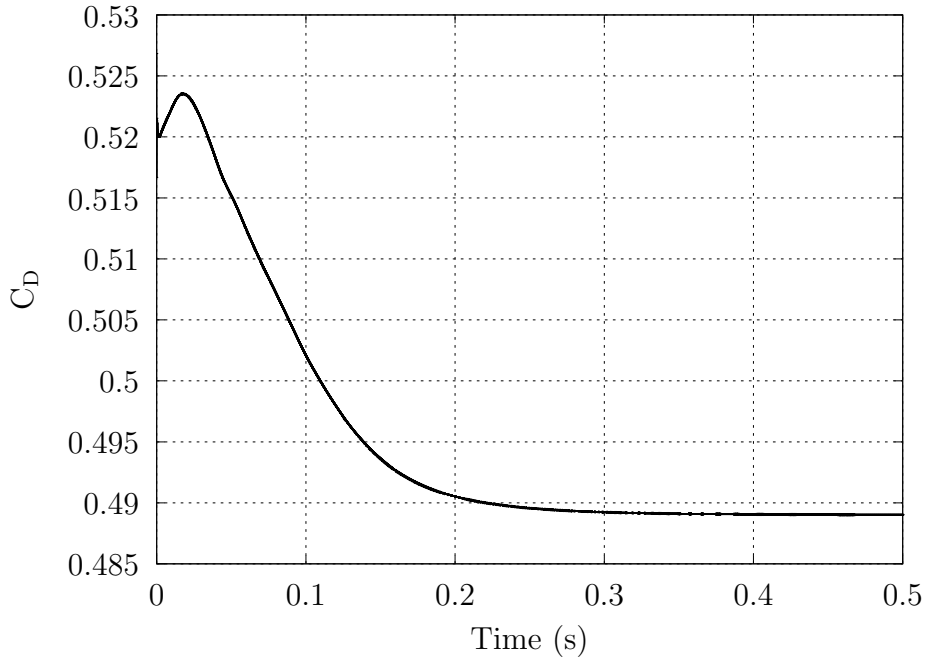

Figure 4.9: *Generic Mirror on a Flat Plate. Computation based on the URANS equations. Evolution of the computed drag coefficient.*

Unsteady DDES simulation

DDES is an unsteady model, which has proven to be more accurate than the conventional RANS model or URANS model, when a proper mesh is used. The unsteady DDES simulation was conducted in three phases:

1. Start the DDES simulation with time step $dt = 10^{-4}$ sec in order to quickly flush the initial transient. Run for physical time $t = 0.1sec$. The flow solution was initialized by a converged RANS flow solution.

2. Decrease of the time step to $dt = 2 \cdot 10^{-5}$ sec, in order to increase the accuracy and run for additional time $t = 0.4sec$, to better converge the flow statistics.

3. Run for another $t = 0.4sec$ with the same dt, to store the required data and average the flow field.

The evolution of the drag coefficient is presented in fig. 4.10 and the dimensionless residuals of the governing equations in fig. 4.11. The residuals of the unsteady equations fluctuate, as could be expected, but their mean value seems fixed.

Table 4.3 compares the drag coefficient computed utilizing the DDES model with different numerical schemes for the convection term of the momentum equation, the (steady) RANS and the URANS model with the value computed in [30]. The DDES computed C_D correlates satisfactory with the reference value of [30], contrary to the values computed by RANS and URANS. The DEShydrib scheme for the convection results are closer to the reference, followed by the limitedLinear and the linearUpwind scheme. Fig. 4.12, compares the static pressure coefficient on different sensors on the mirror surface acquired through a RANS, URANS and DDES simulations with experimental data [29]. Figs 4.13 and 4.15 illustrate velocity magnitude isolines, for the DDES and RANS models, on the symmetry plane and on a horizontal plane at $y = 0.5D$. The same comparison is presented in figs. 4.14, 4.16 for the pressure field contour lines. It is clear that RANS and DDES predict different flow fields, mostly in the wake. The resolved unsteady flowfield is presented in fig. 4.17.

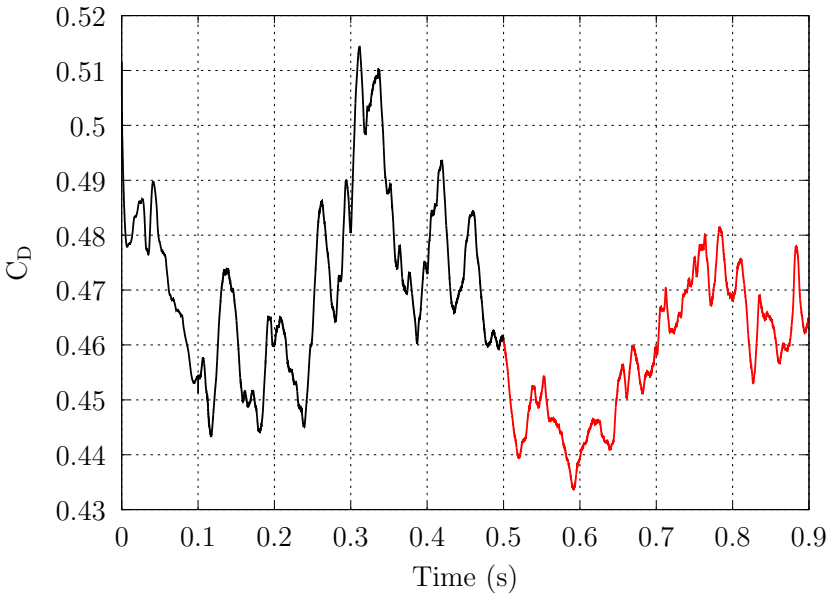

Figure 4.10: *Generic Mirror on a Flat Plate. Computation based on the DDES equations. Evolution of the computed drag coefficient. The data line colored red corresponds to the last* 0.4 *s of the simulation, in which averaging of flow variables and coefficients is applied.*

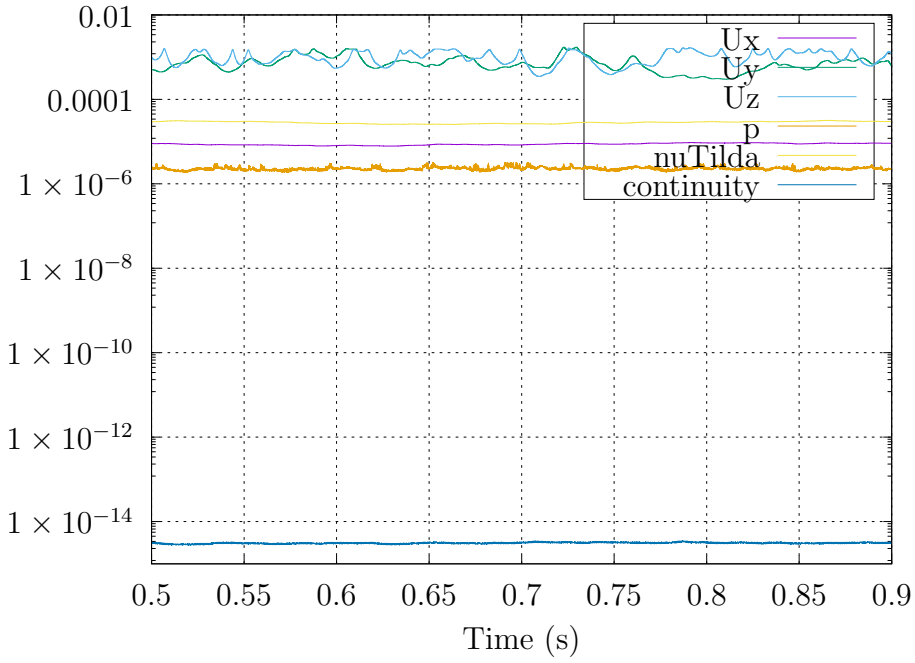

Figure 4.11: *Generic Mirror on a Flat Plate. Computation based on the DDES equations. Evolution of dimensionless residuals of the governing equations.*

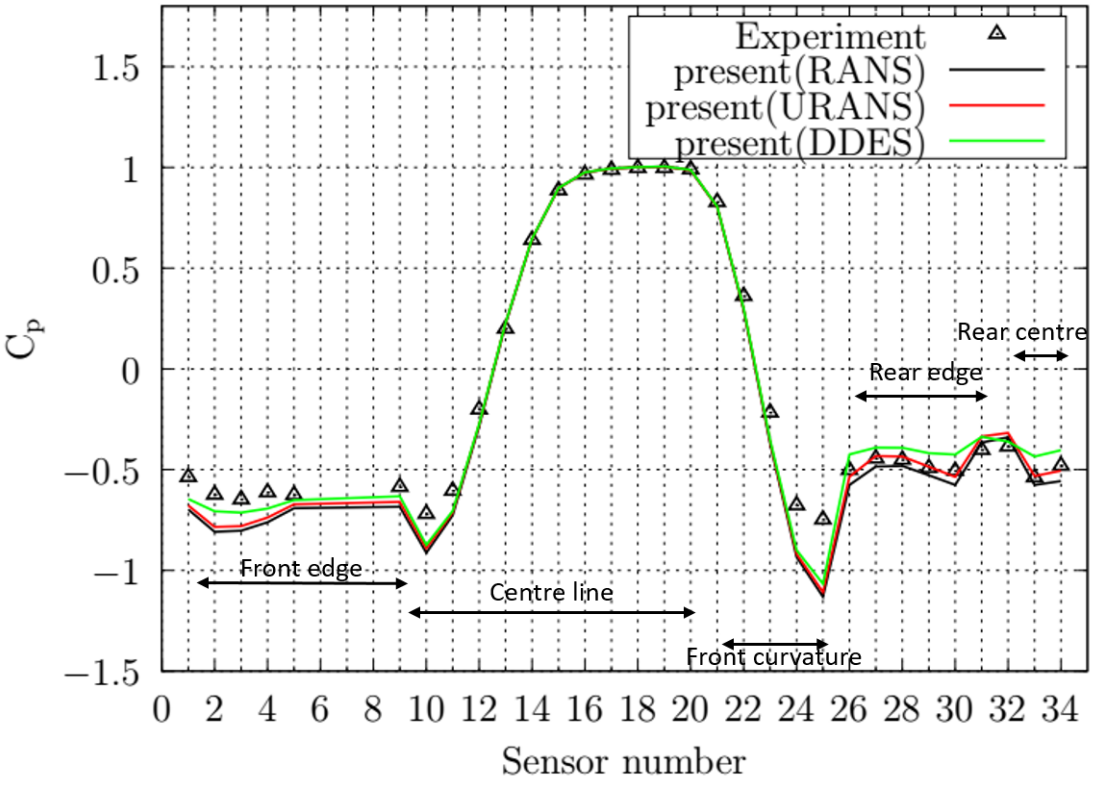

Figure 4.12: *Generic Mirror on a Flat Plate. Comparison of the static pressure coefficient C_p, based on experimental data, present RANS, URANS and DDES simulation, on many sensors on the mirror's surface. For the unsteady data C_p stands for the averaged coefficient.*

	C_D	$\frac{C_D - C_{D(ref)}}{C_{D(ref)}}\%$
Ref. value, simulation [30]	0.4437	–
RANS	0.5243	18.17%
URANS	0.4952	11.61%
DDES-linearUpwind	0.45507	2.56%
DDES-limitedLinear	0.43625	1.678%
DDES-DEShybrid	0.4475	0.856%

Table 4.3: *Generic Mirror on a Flat Plate. Comparison of the drag coefficient computed with, a steady RANS-SA, an unsteady URANS-SA and an unsteady DDES-SA solver with a reference value from the simulation results presented in [30]. For the DDES-SA case, the effect of three different schemes for the momentum's convection is tested.*

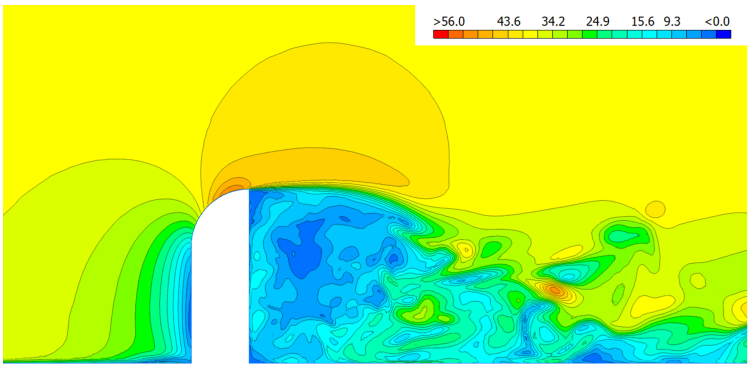

(a) *DDES, instantaneous velocity u*

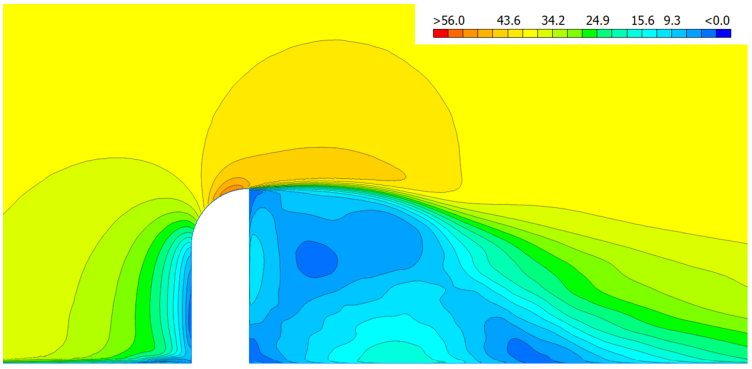

(b) *DDES, averaged velocity* $\overline{u}$

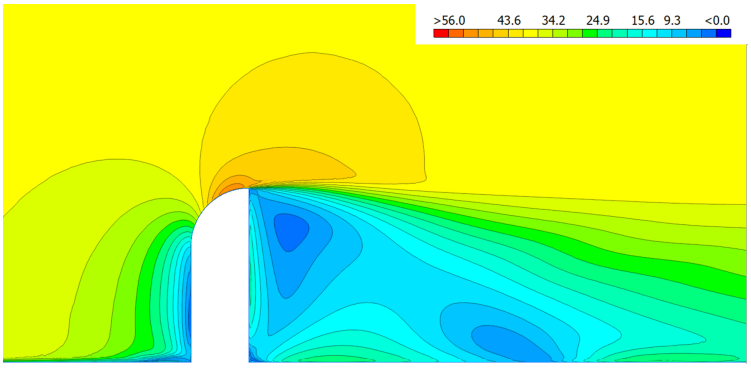

(c) *RANS, last iteration solution u*

Figure 4.13: *Generic Mirror on a Flat Plate. Comparison of (a) the instantaneous and (b) averaged velocity contour lines, from the DDES, with (c) the velocity contour lines on the last iteration of the RANS solver, on the symmetry plane.*

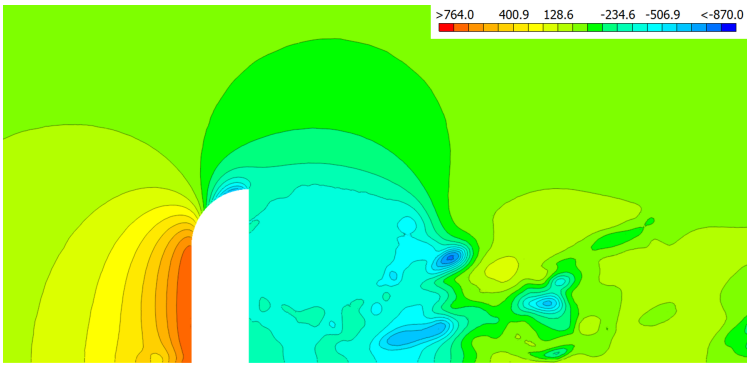

(a) *DDES, instantaneous pressure p*

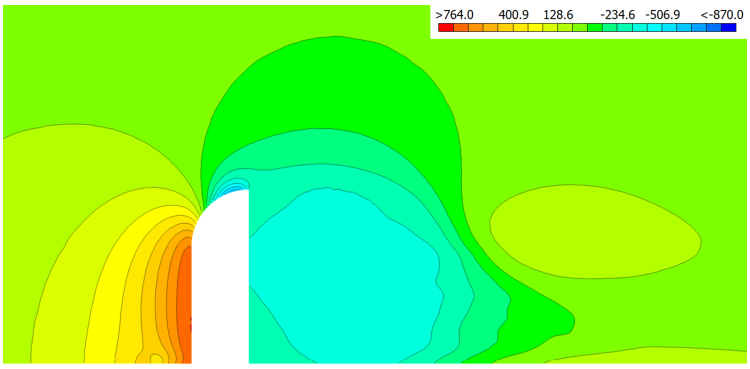

(b) *DDES, averaged pressure* $\overline{p}$

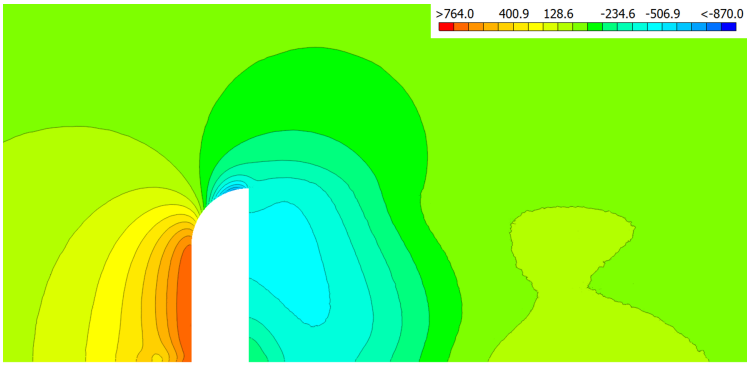

(c) *RANS, last iteration solution p*

Figure 4.14: *Generic Mirror on a Flat Plate. Comparison of (a) the instantaneous and (b) averaged pressure contour lines, from the DDES, with (c) the pressure contour lines on the last iteration of the RANS solver, on the symmetry plane.*

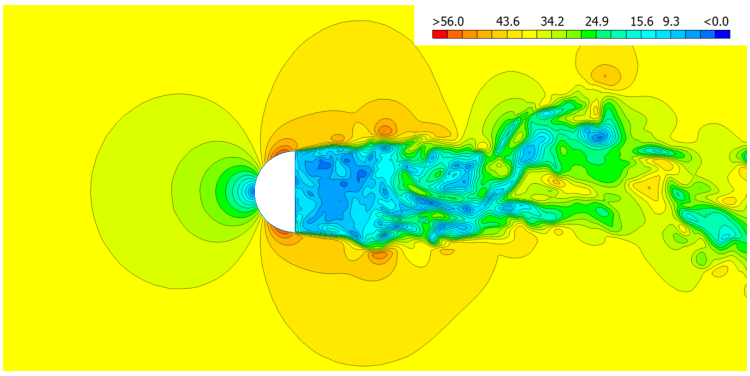

(a) *DDES, instantaneous velocity u*

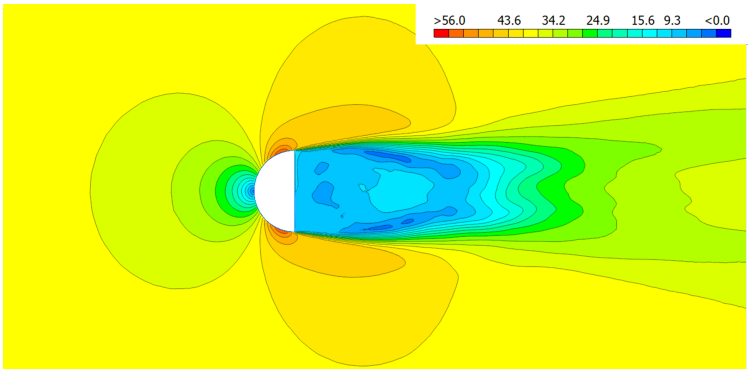

(b) *DDES, averaged velocity* $\overline{u}$

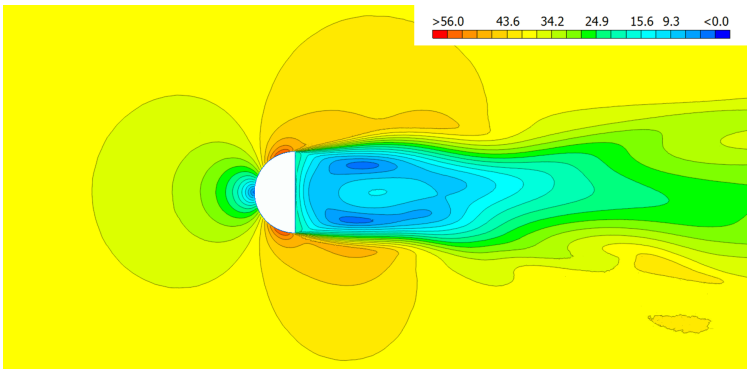

(c) *RANS, last iteration solution u*

Figure 4.15: *Generic Mirror on a Flat Plate. Comparison of (a) the instantaneous and (b) averaged velocity contour lines, from the DDES, with (c) the velocity contour lines on the last iteration of the RANS solver, on a horizontal plane at* $y = 0.5D$.

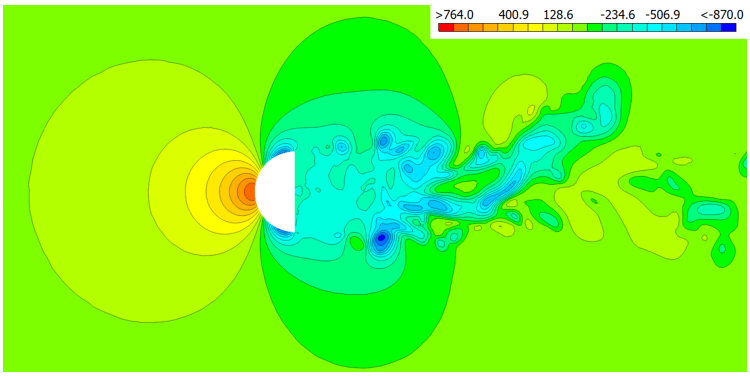

(a) *DDES, instantaneous pressure p*

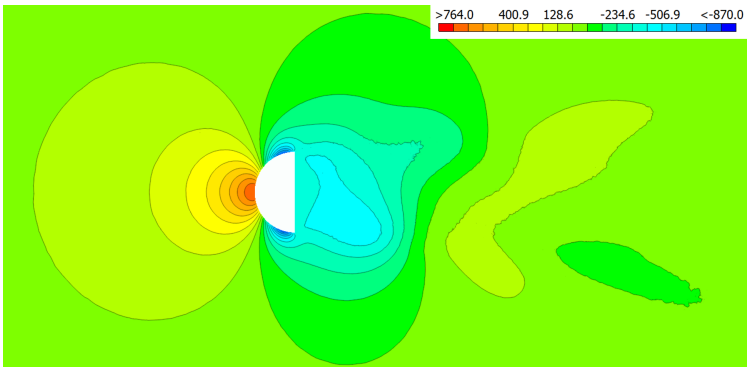

(b) *DDES, averaged pressure* $\overline{p}$

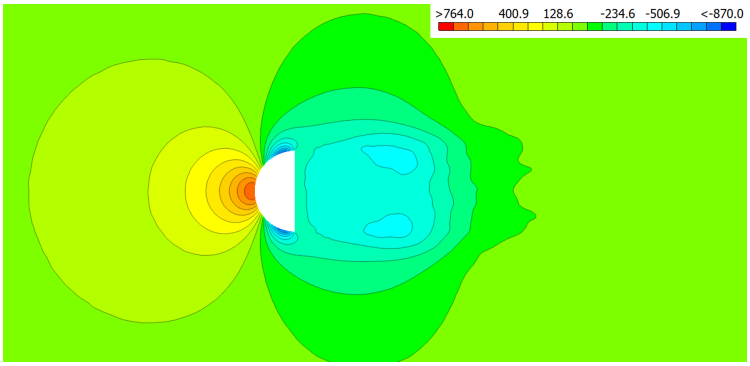

(c) *RANS, last iteration solution p*

Figure 4.16: *Generic Mirror on a Flat Plate. Comparison of (a) the instantaneous and (b) averaged pressure contour lines, from the DDES, with (c) the pressure contour lines on the last iteration of the RANS solver, on a horizontal plane at* $y = 0.5D$.

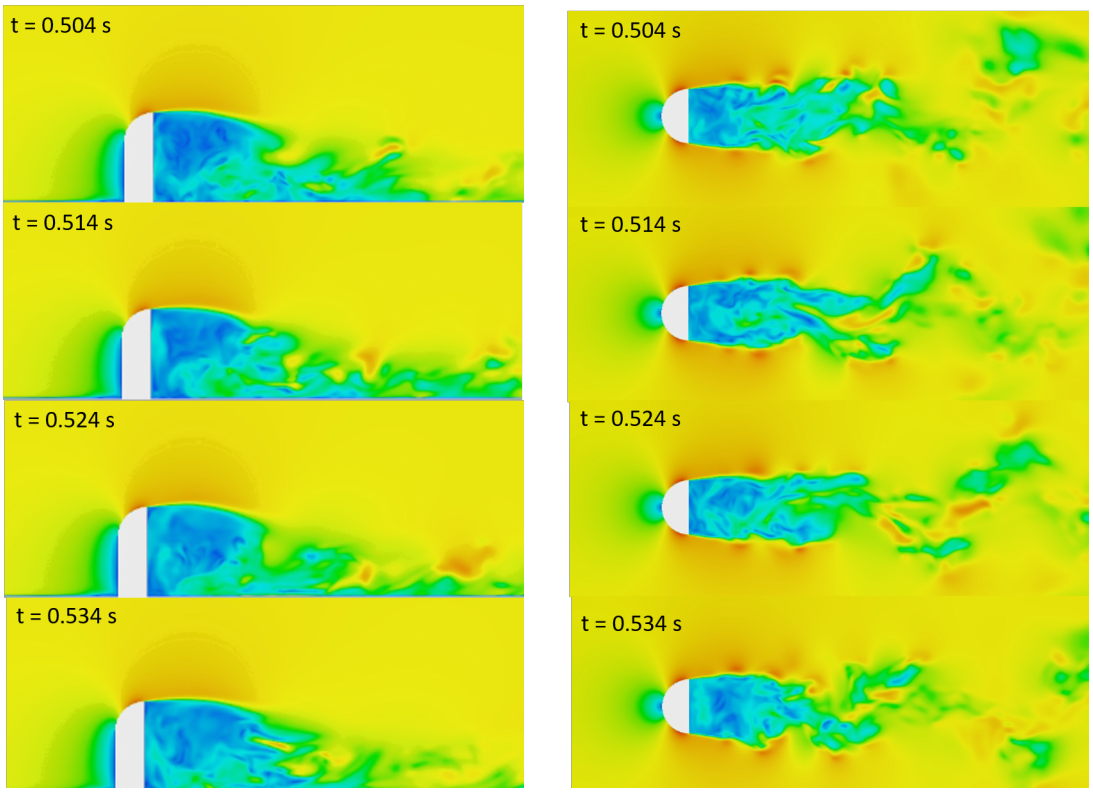

(a) *Symmetry Plane.*

(b) *Section on a horizontal plane at* $y = 0.5D$.

Figure 4.17: *Generic Mirror on a Flat Plate. Four different snapshots of the velocity magnitude field based on the DDES model in two section planes, the symmetry and a horizontal plane at* $y = 0.5D$.

In figs. 4.18 and 4.19, the RMS value of the pressure fluctuations on the plate and mirror is presented. It is clear that the magnitude of the pressure fluctuations on the plate's surface is greater than on the mirror itself and, thus, the plate's contribution to the noise at the microphones, as described by the Curle's integral, should be greater. The low levels of p_{RMS} in the front side of the mirror, translate to mostly steady flow of the incoming flow. It is the separation of the flow and the turbulent structures that make the flow unsteady in the wake.

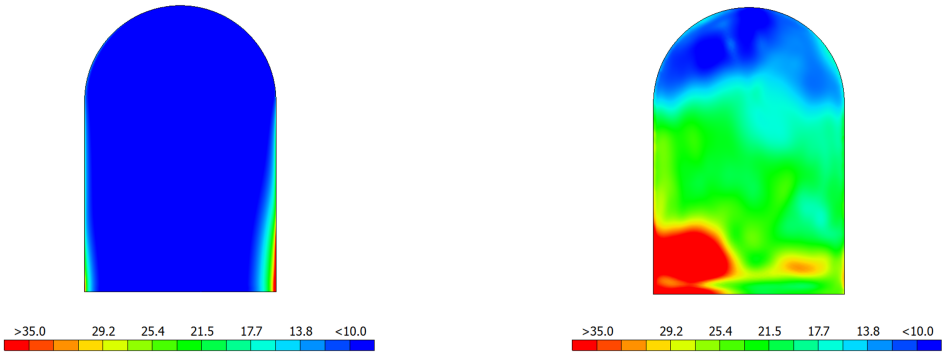

(a) *Front view* **(b)** *Back view*

Figure 4.18: *Generic Mirror on a Flat Plate. Computation based on DDES. Root Mean Square value of the pressure fluctuations p_{rms} on the mirror's surface.*

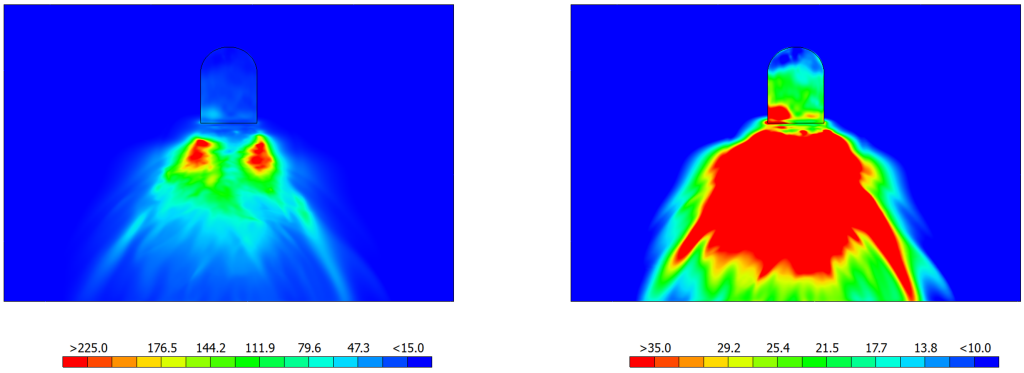

Figure 4.19: *Generic Mirror on a Flat Plate. Computation based on DDES. Root Mean Square value of the pressure fluctuations p_{rms} on the plate's surface.*

4.1.5 Acoustic Results

Although the unsteady pressure fluctuations on the surface of the body are of hydrodynamic nature, they act also as sources for sound waves that propagate away from the surface.

Comparison of Surface Pressure Fluctuations Spectrum

A comparison of the surface pressure fluctuations spectrum on different sensor positions with experimental data and simulations is presented in figs. 4.20, 4.21. The unsteady pressure fluctuations acquired over the last 0.4 sec of the solver are transformed to the frequency domain through an FFT algorithm and integrated over 10

Hz frequency bands. Pressure Level (PL) (section 1.1.1) in dB is defined as:

$$PL = 10log_{10}(\frac{\hat{p_f}^2}{p_{ref}^2}) \tag{4.1}$$

where $\hat{p_f}^2$ is the level of the power spectrum of the pressure fluctuations on the frequency band with central frequency f and $p_{ref} = 2 \cdot 10^{-5}$ a reference value.

In most of the sensor positions, the pressure fluctuation levels agree, up to some frequency, with the reference's simulation data [29]. Both the numerical schemes tested seem to converge well with the measurements, with the linearUpwind scheme being slightly better.

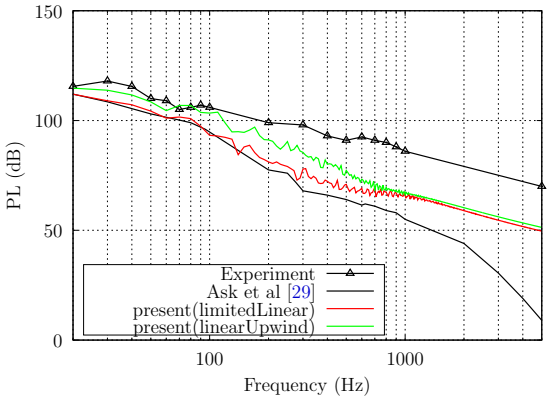

(a) *Pressure level (dB) spectrum at sensor S111.*

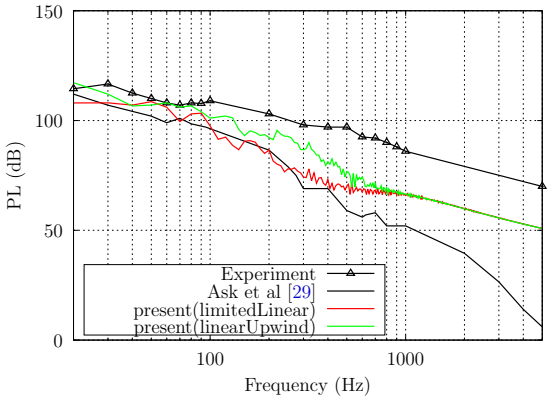

(b) *Pressure level (dB) spectrum at sensor S114.*

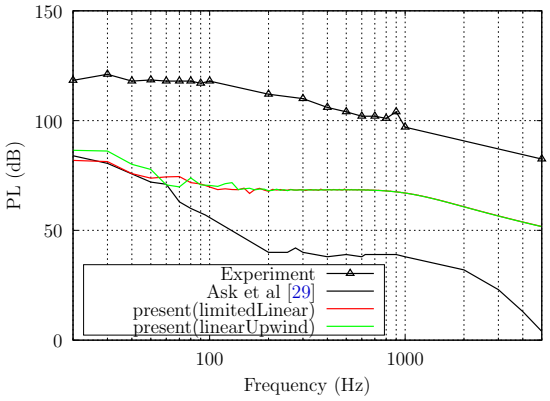

(c) *Pressure level (dB) spectrum at sensor S116.*

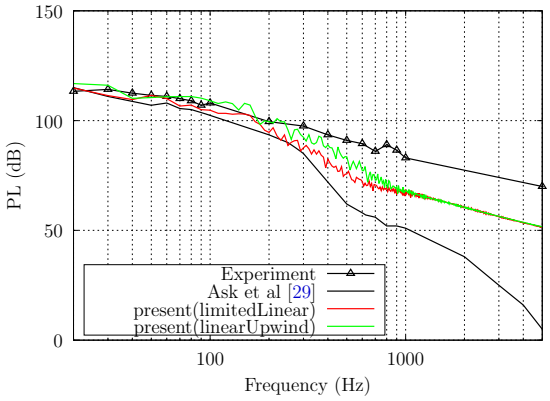

(d) *Pressure level (dB) spectrum at sensor S119.*

Figure 4.20: *Generic Mirror on a Flat Plate. Pressure level (dB) spectrum at sensors S111, S114, S116, S119.*

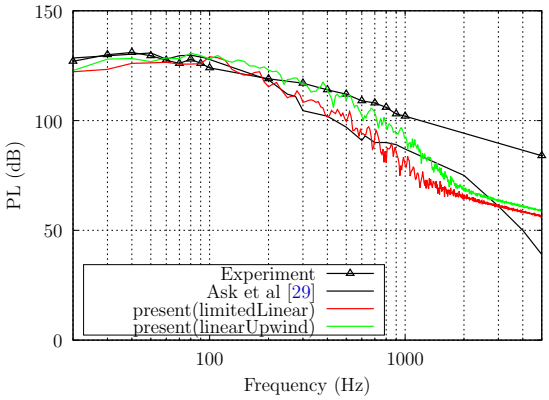

(a) *Pressure level (dB) spectrum at sensor S121.*

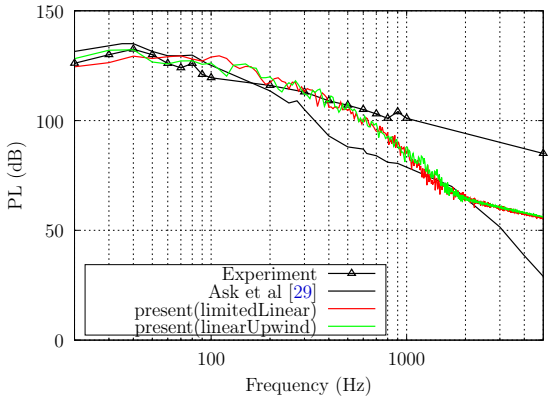

(b) *Pressure level (dB) spectrum at sensor S122.*

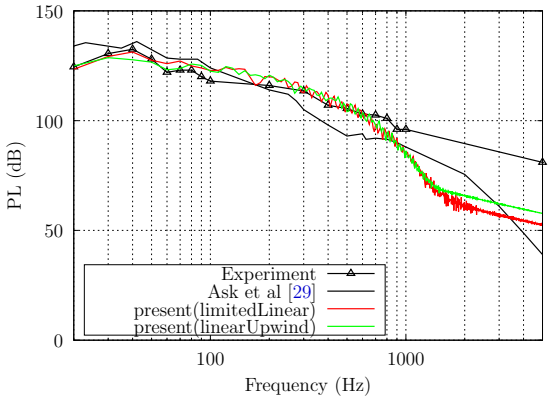

(c) *Pressure level (dB) spectrum at sensor S123.*

Figure 4.21: *Generic Mirror on a Flat Plate. Pressure level (dB) spectrum at sensors S121, S122, S123.*

Comparison of Acoustic Pressure Fluctuations Spectrum

Utilizing the Curle's surface integral and the stored unsteady surface pressure fluctuations on the mirror's and plate's surface, acquired with the linearUpwind scheme for the momentum, the acoustic pressure signal and the resulting power spectrum was computed on five microphone positions. A comparrison with experimental and simulation data [29] is presented in fig. 4.22, where for the simulation data Curle's surface integral method was also used. SPL is also computed from eq. 4.1, but a different name is used to distinguish the pressure computation based on Curle's approach (SPL) from that computed by the solver itself (PL). For microphones M1, M10 and M11 the present implementation of Curle's integral show better convergence to the experimental data than the simulation results of [29]. For microphone

M4, the convergence to measurements is worse and for microphone M14, both simulations miss-match the measurements.

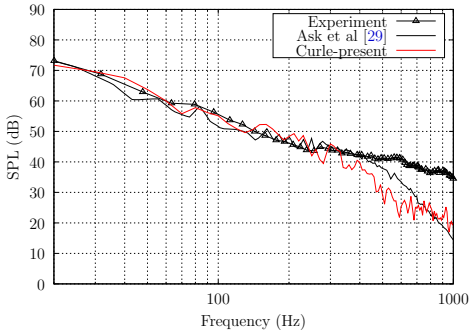

(a) *Sound Power level (dB) spectrum at mic M1.*

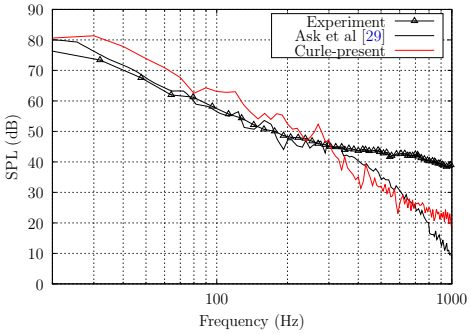

(b) *Sound Power level (dB) spectrum at mic M4.*

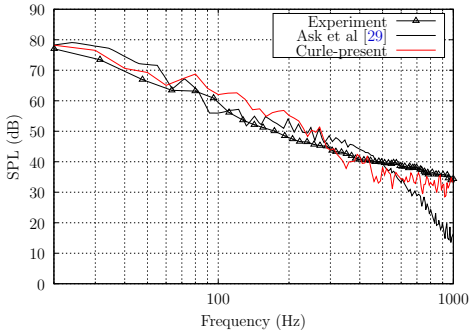

(c) *Sound Power level (dB) spectrum at mic M10.*

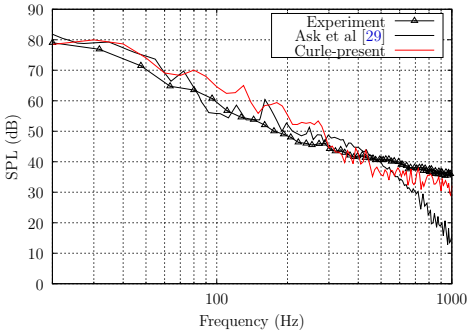

(d) *Sound Power level (dB) spectrum at mic M11.*

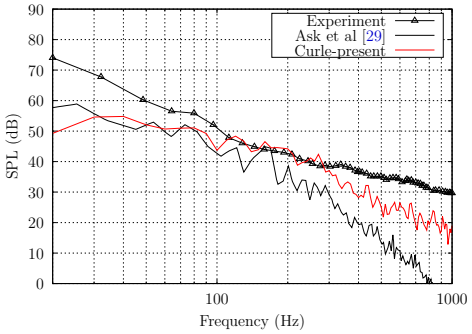

(e) *Sound Power level (dB) spectrum at mic M14.*

Figure 4.22: *Generic Mirror on a Flat Plate. Sound Power level (dB) spectrum at microphones M1, M4, M10, M11, M14.*

Side to the previous comparison, the hydrodynamic PL as predicted by the incom-

pressible DDES-SA solver is compared with the Curle's integral result in three of the five microphone positions. Results in fig. 4.23 show that, for all the microphones, the Curle's integral is more accurate in predicting the PL, up to a certain frequency, than the solver itself, which on its side is losing accuracy due to the coarser CFD mesh at the area of calculation and the interpolations used.

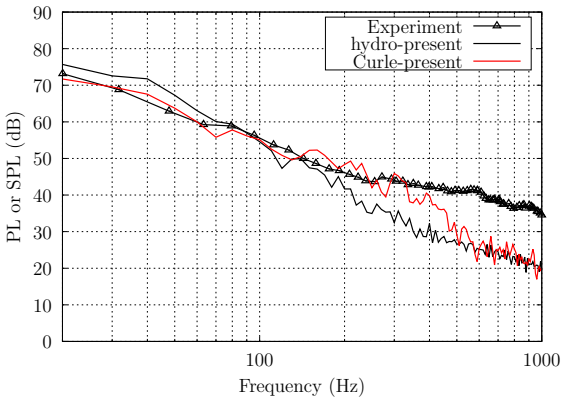

(a) *Sound Power level (dB) spectrum at mic M1.*

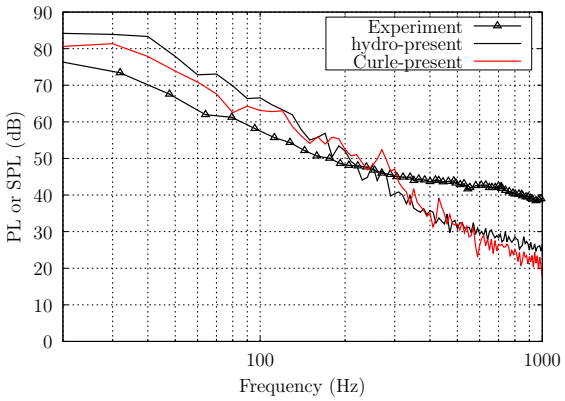

(b) *Sound Power level (dB) spectrum at mic M4.*

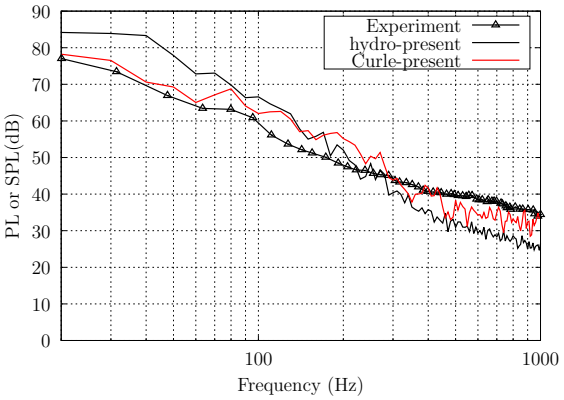

(c) *Sound Power level (dB) spectrum at mic M10.*

Figure 4.23: *Generic Mirror on a Flat Plate. SPL and PL (dB) spectrum at microphones M1, M4, M10. Comparison of the DDES calculated SPL with the Curle's integral result and the experimental one.*

4.2 Application to a Production Car

In this chapter, the ENP method is applied to a production car. The change of ENP index is tested on the baseline and in a modification of the former; the modified

having 5 additional ribs attached to its body (fig. 4.25, 4.26). The ribs have been placed in the area of the side glass, knowing that they will generate noise, in order to test if the method can recognize their effect. For both geometries wind tunnel testing was conducted on the semi-anechoic S2A GIE wind tunnel (fig. 4.24) and the interior noise levels have been measured. Also, a phased array beamforming technique for exterior noise source identification was applied. In order to take into account only the contribution of the upper part of the car to the interior noise and exclude the leak sources from the measurement, the underbody of car was closed with cardboard and all the gaps were completely sealed with tape (fig. 4.27). In addition, the wipers and the antenna of the car had been removed. The effect of the underbody on the interior noise is dominant on medium and low frequencies under 2000 Hz and at that range dominates the spectrum [31]. The above procedure aims to evaluate only the dipole sources on the A-pillar and side mirror area, radiating sound to the interior and has been followed by many researchers during measurements [32], [33].

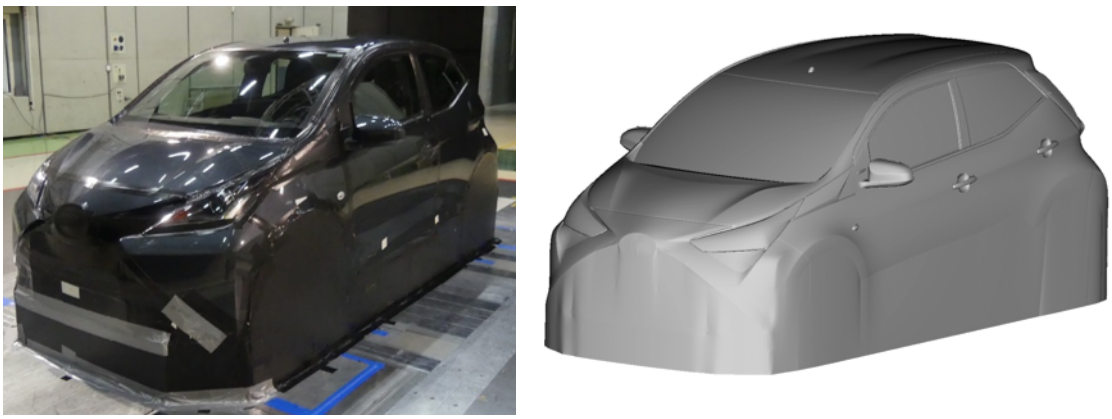

Figure 4.24: *Application to a Production Car. A view of the actual car on the wind tunnel (left) and the simulated geometry (right).*

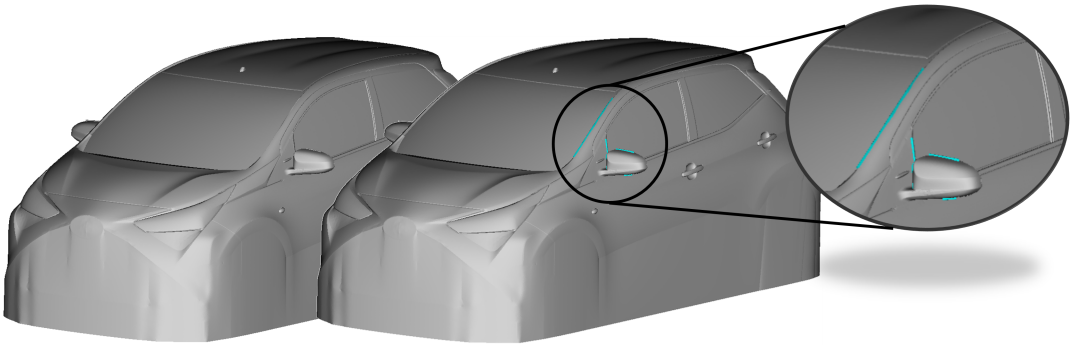

Figure 4.25: *Application to a Production Car. A view of the two simulated geometries; the baseline (left) and the modified car (right).*

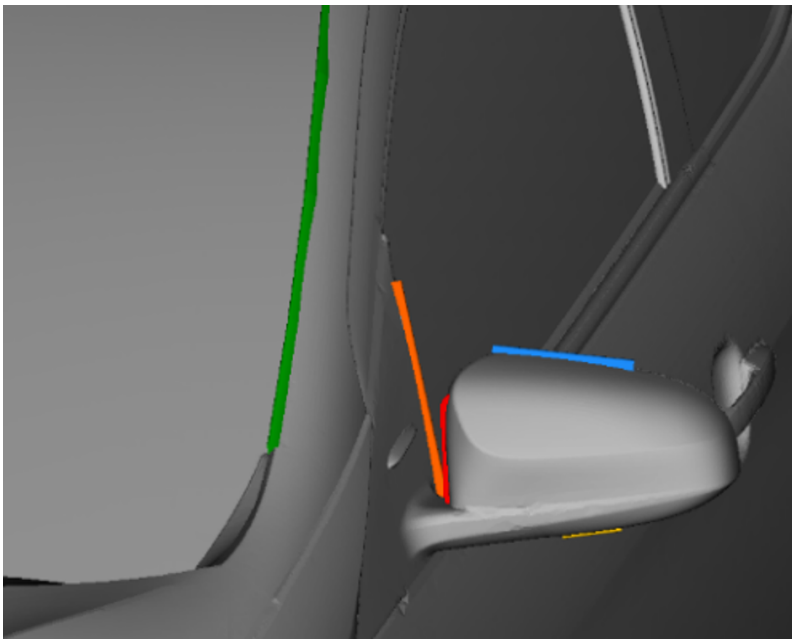

Figure 4.26: *Application to a Production Car. Modifications on the baseline car geometry. Five additional ribs are added, namely the mirror top (blue), the mirror bottom (yellow), the mirror side (red) and the A-pillar rib (green).*

Figure 4.27: *Application to a Production Car. Two views of the car with the skirt used to completely seal the underbody in the wind tunnel.*

4.2.1 CFD Mesh

In the CFD simulations that follow, only half of the car was simulated, taking advantage of the obvious symmetry. This simplification is expected to introduce some error in the vicinity of the symmetry plane for a DDES simulation. Nevertheless, this choice seems logical regarding the computational cost of solving a full car and is further supported by the fact that the flow field of interest, away of the symmetry plane (the A-pillar and mirror area), will be affected less [34].

For both geometries, mesh refinement boxes are used (fig. 4.29) in the area of the A-pillar and the side glass, resulting in $34 \cdot 10^6$ volume elements to discretize the fluid flow and $2.8 \cdot 10^6$ surface elements to represent the car's surface. For the modeling of the boundary layer close to the wall, wall functions are used combined with the Spalart-Allmaras turbulence model, so five prism layers were constructed with average $y^+ \approx 15 - 30$ at the first cells off the wall to accurately predict the flow. The virtual wind tunnel geometry is presented in fig. 4.28.

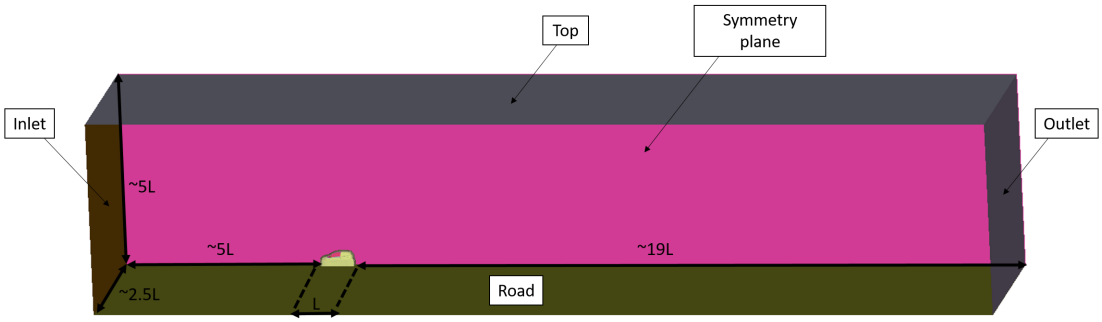

Figure 4.28: *Application to a Production Car. The virtual windtunnel configuration.*

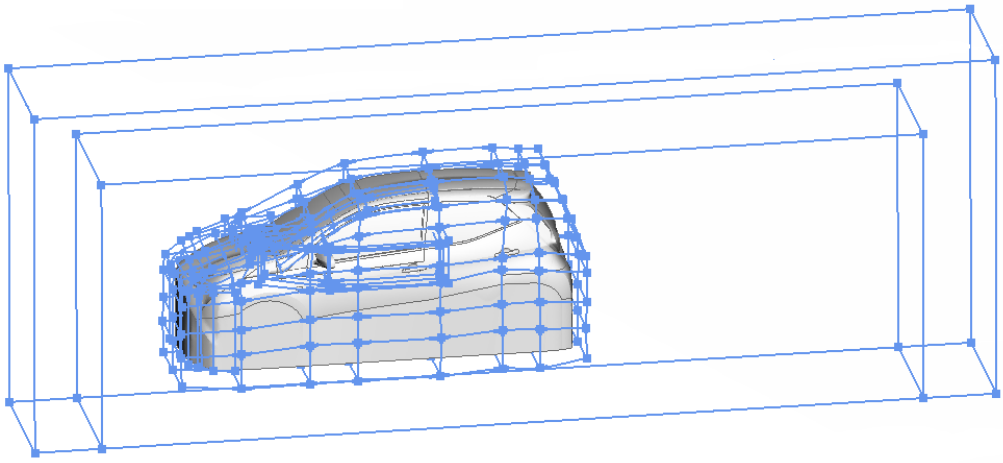

Figure 4.29: *Application to a Production Car. The mesh refinement boxes used in the mirror and A-pillar region.*

4.2.2 Boundary Conditions

The boundary conditions for velocity and pressure used in this case are presented in table 4.4.

Boundary Conditions		
Boundary	**Velocity**	**Pressure**
Inlet	Dirichlet $\vec{U} = (33.3, 0, 0)m/s$	zero Neumann
Outlet	zero Neumann	zero Dirichlet
Car surface, Road	zero Dirichlet	zero Neumann
Side, Top, Symmetry plane	symmetry	symmetry

Table 4.4: *Application to a Production Car. Boundary conditions for pressure and the velocity.*

4.2.3 Aerodynamic Results

Unsteady DDES Simulation

Prior to the acoustic calculations, based on the ENP method, the unsteady flow field around the car needs to be solved and the surface pressure fluctuation field on the desired surfaces needs to be stored. For both geometries, the DDES-SA turbulence model was used and the unsteady simulation was conducted as follows:

1. Initializing from a converged RANS solution, solve using the DDES-SA model with time step $dt = 10^{-4}$ sec in order to quickly flash the initial transient. Run for physical time $t = 0.5sec$.

2. Decrease the time step in half, $dt = 5 \cdot 10^{-5}$ sec to increase the accuracy and run for additional time $t = 1.0sec$ until the flow is statistically converged.

3. Run for another $t = 0.5sec$, to store the surface pressure fluctuation data on the desired surfaces (fig. 4.40) and average the velocity field.

The evolution of the dimensional residuals of the governing equations over simulation time for the baseline car are presented in fig. 4.30 and the evolution of the normalized drag coefficient for both the baseline and the modified geometry in fig. 4.31.

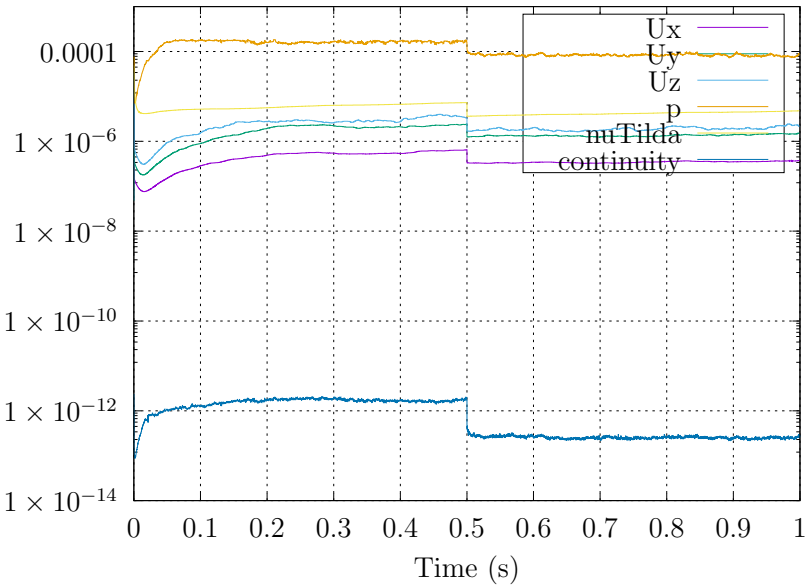

Figure 4.30: *Application to a Production Car. Dimensionless residuals of the governing equations over simulation time.*

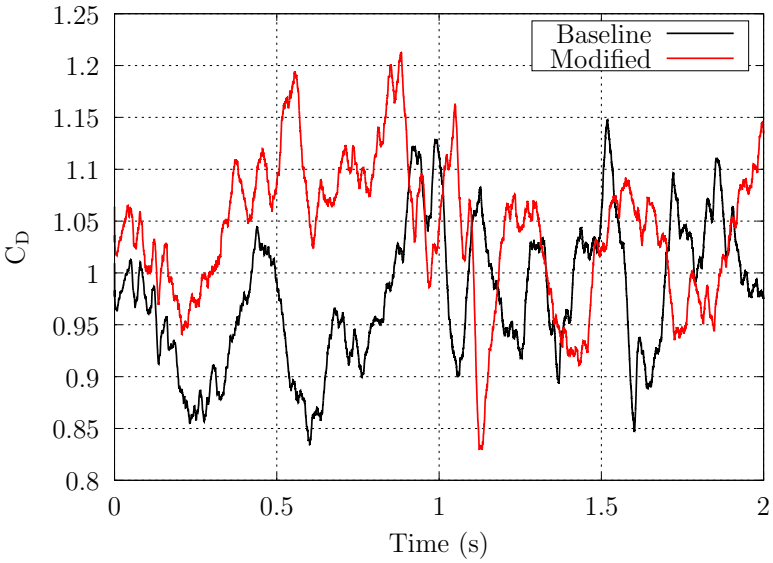

Figure 4.31: *Application to a Production Car. Evolution of the computed, normalized drag coefficient for both geometries over simulation time.*

The separation region at the A-pillar and side mirror area is greater in the modified geometry than in the baseline. This is visualized in fig. 4.32, where two views of the total pressure coefficient $c_{p,Total} = 0$ isosurface are presented. In the modified geometry, the flow is separated in most of the side window surface, as also seen in figs. 4.33, 4.34.

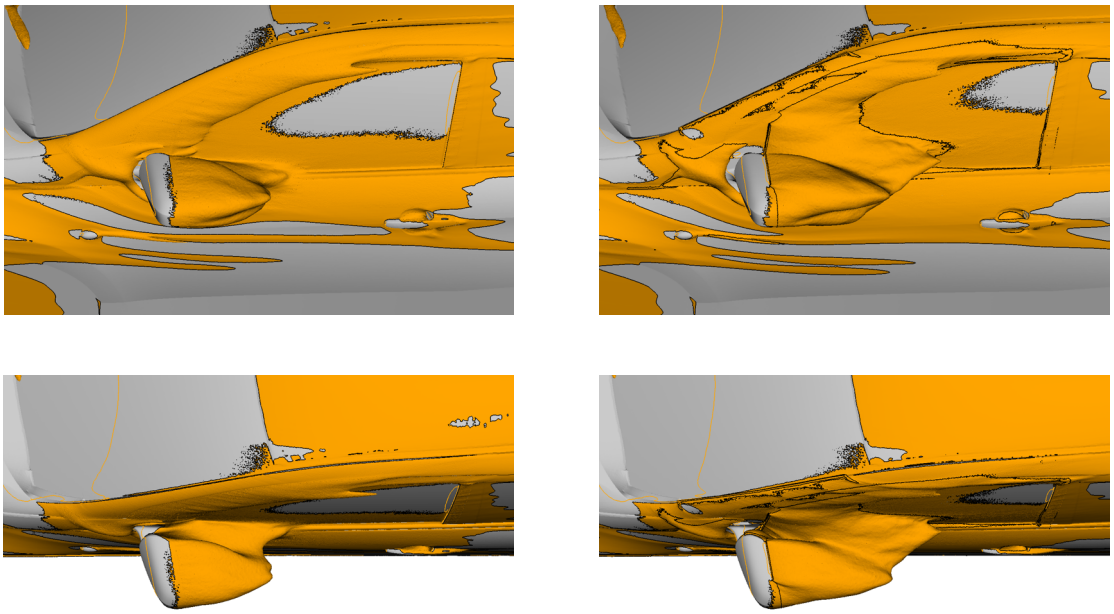

(a) *Baseline* **(b)** *Modified*

Figure 4.32: *Application to a Production Car. Comparison of separation region illustrated by the total pressure coefficient isosurfaces* $c_{p,Total} = 0$*, between baseline car (left) and modified (right).*

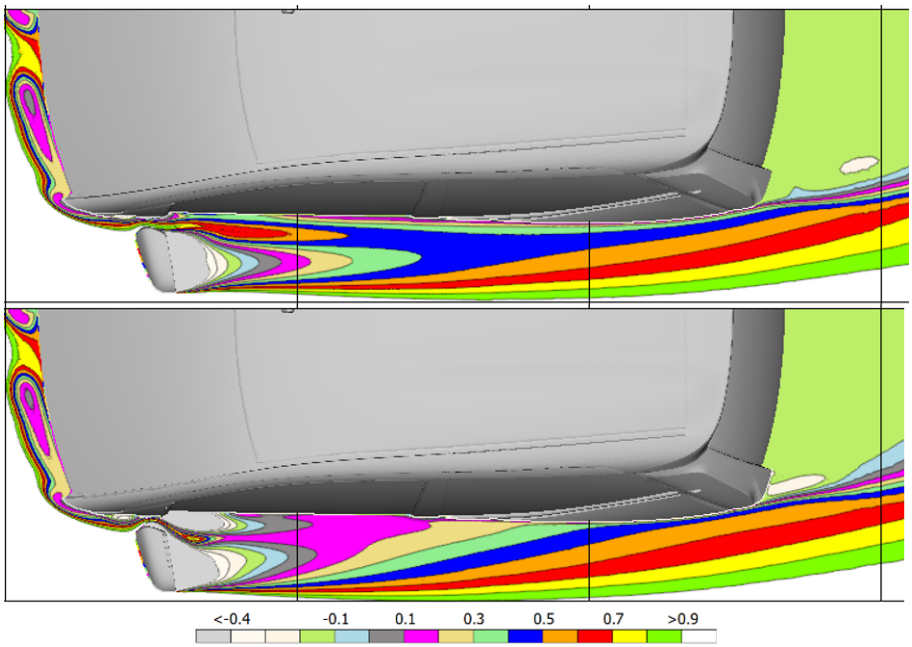

Figure 4.33: *Application to a Production Car. Comparison of* $c_{p,Total}$ *contours between baseline and modified geometries respectively, at a horizontal section cutting the mirror.*

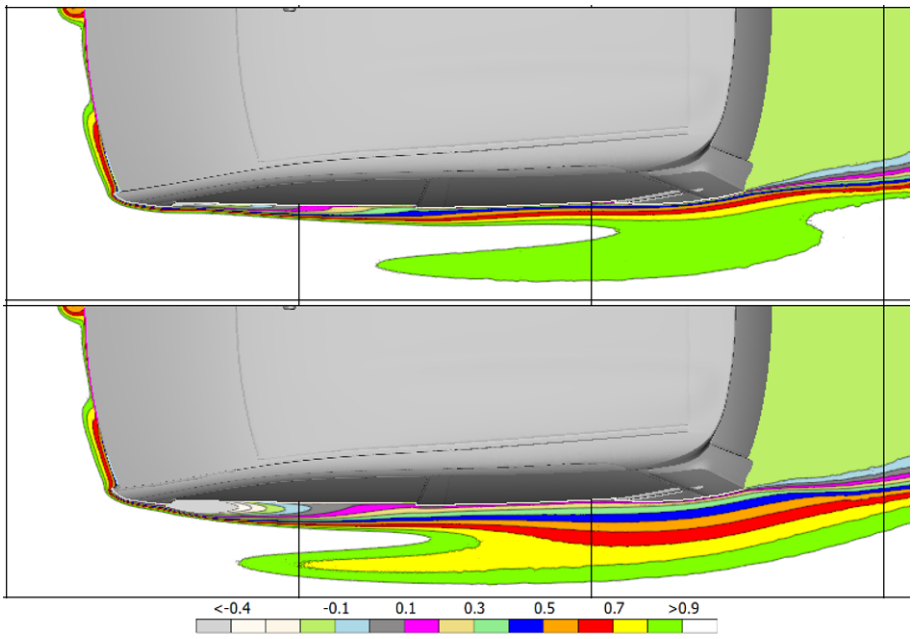

Figure 4.34: *Application to a Production Car. Comparison of $c_{p,Total}$ contours between baseline and modified geometries respectively, at a horizontal section cutting the A-pillar.*

The flow separation in the side glass in the modified geometry is enhanced due to the effect of the side window rib, acting as a barrier guiding the flow away. This changes the wake of the mirror as seen in fig. 4.35. In this figure, the Line Integral Convolution (LIC[1]) representation of the streamlines of the flowfield are presented.

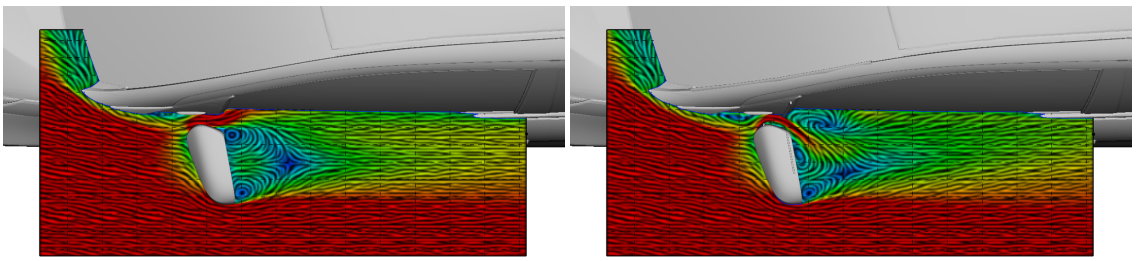

(a) *Baseline* **(b)** *Modified*

Figure 4.35: *Application to a Production Car. LIC lines at a horizontal plane at the vicinity of the car's mirror for the baseline and the modified case respectively.*

The use of the DDES with a symmetry plane close to the simulated geometry is partially justified by the comparison of the mean field quantities from DDES simulation

[1]The LIC representation is a way of visualizing the flow field by coloring the pixels of the image that reside on the same streamline of the flow with similar levels of the greyscale palette.

with experimental data (figs. 4.37, 4.38). In order to acquire the flowfield on the mirror wake experimentally, a scan was conducted with a omnidirectional 18 hole probe 4.36, averaging the measured data in time. As a result, the measured average field quantities can be compared with the averaged RANS solution and averaged DDES solution on the same plane.

Figure 4.36: *Application to a Production Car. The L-shaped 18 hole omnidirectional probe used to measure the mirror's wake. From [35].*

Fig. 4.39, showing 6 snapshots of the DDES acquired velocity magnitude flowfield on a section at the height of the mirror, illustrates the resolved unsteady flowfield by the DDES model.

4.2.4 ENP Method Results

Having the unsteady pressure data stored, the ENP method is applied. Fig. 4.40 shows the area in which the ENP method is applied and the sub-surfaces that contribute to the total ENP are marked with different colors. Namely FR-PLR stands for the A-pillar, SW for Side window, FR-DOOR is the upper part of the side door under the side window, MIRROR is the mirror geometry, QTR-SW the triangle side to the side window, including the mirror stay, FR-WS the windshield and HOOD a small part of the lower A-pillar.

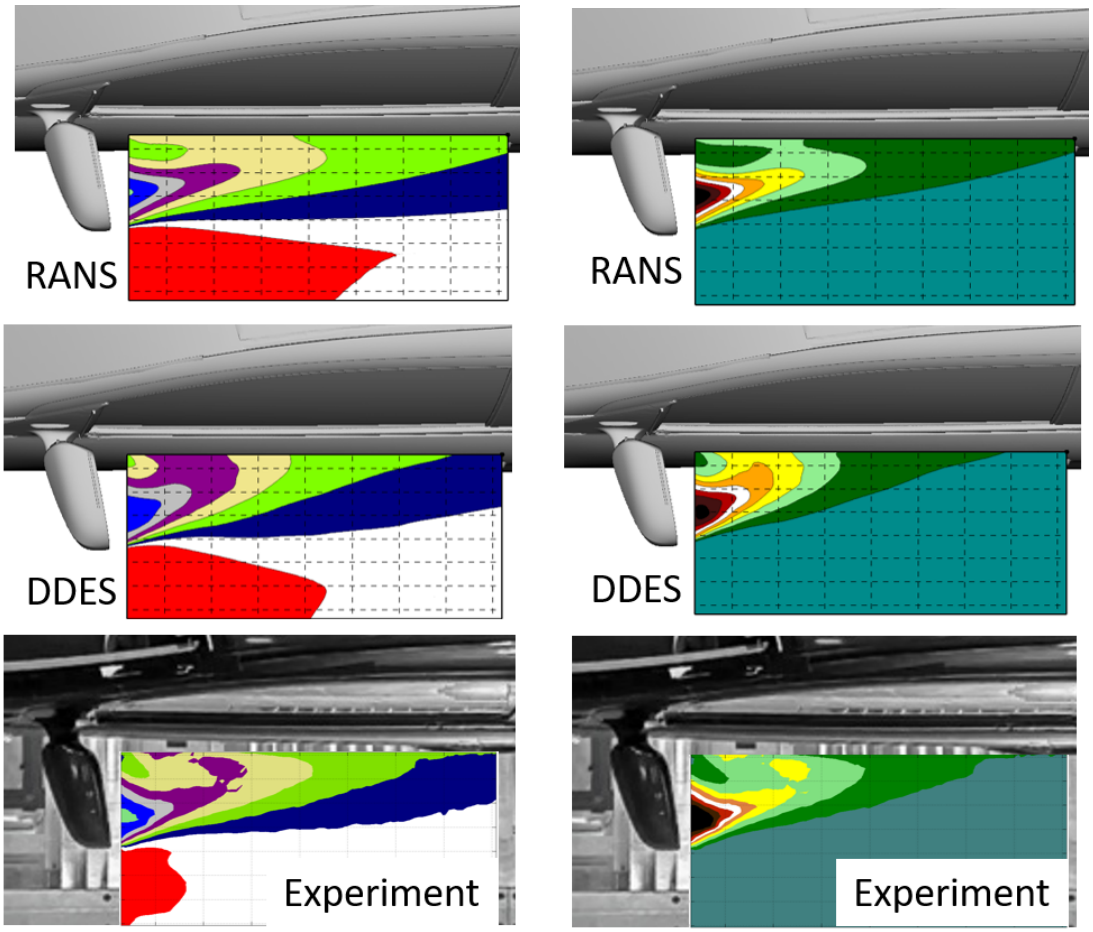

(a) $\frac{U_x}{U_\infty}$ **(b)** $\left(\frac{U_\infty - U_x}{U_\infty}\right)^2$

Figure 4.37: *Application to a Production Car. Comparison of the averaged normalized velocity isolines from the RANS and the DDES model with experimental data, on a section plane on the mirror wake (modified geometry).*

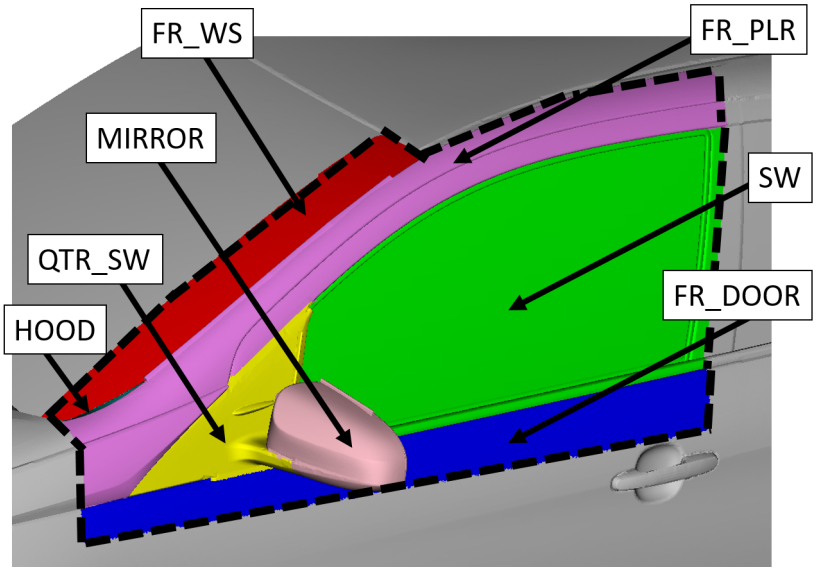

Figure 4.40: *Application to a Production Car. A view of the car area, in which the ENP method will be implemented. The different parts contributing to ENP are colored.*

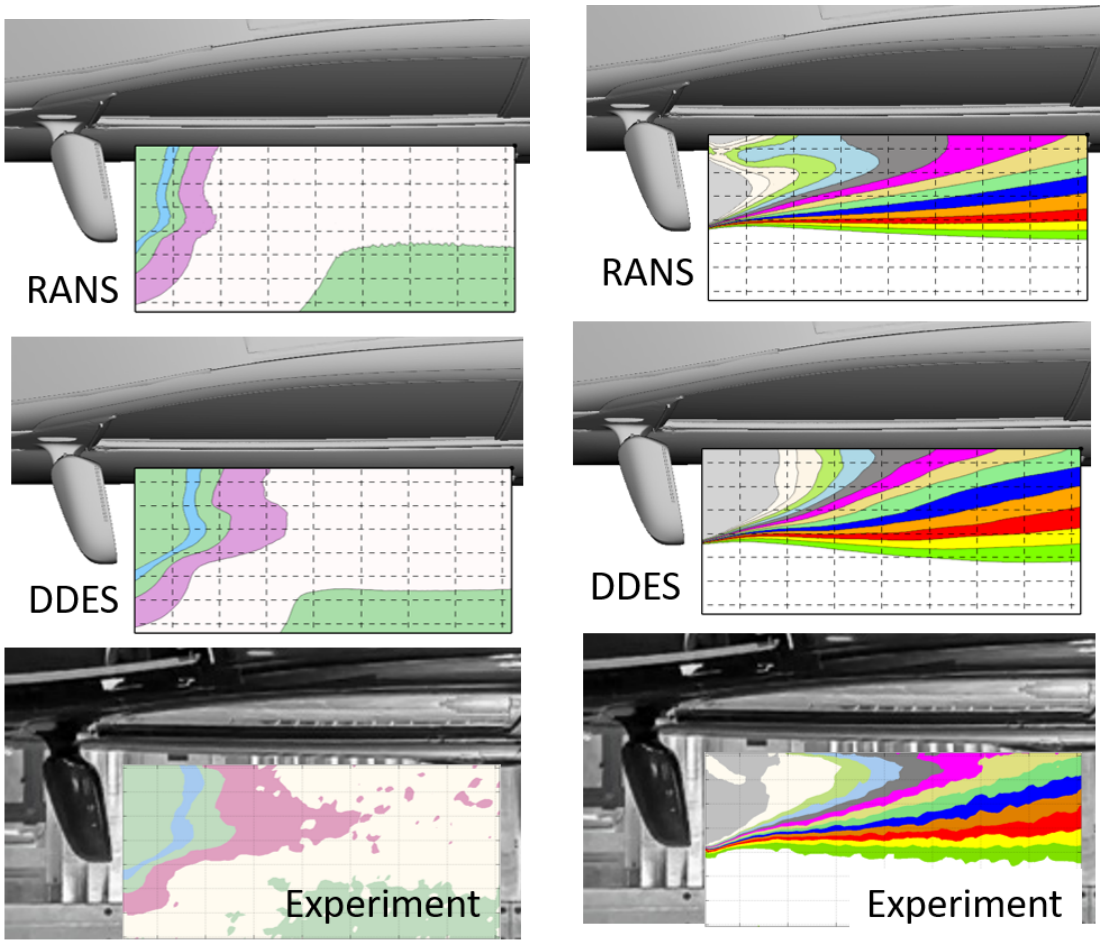

(a) $c_{p,static}$ **(b)** $c_{p,total}$

Figure 4.38: *Application to a Production Car. Comparison of the averaged static and total pressure coefficient isolines form the RANS and the DDES model with experimental data, on a section plane on the mirror wake (modified geometry).*

Fig. 4.41 presents the contribution of each part to the total ENP index. Looking at the 500-4000 Hz bar char it is clear that, for the baseline geometry, the most dominant part is the QTR-SW followed by the SW and the FR-PLR, in contrast with the modified geometry in which FR-PLR is the most noisy part followed by the QTR-SW and SW part. In both cases, QTR-SW has an important effect on farfield radiated acoustic power. The noise sources are visualized through the ENPD intensity map in fig. 4.42. Noise source contribution can be studied as a whole in a wider band of $500-4000$ Hz or in more detail looking at the $1st$ octave band results.

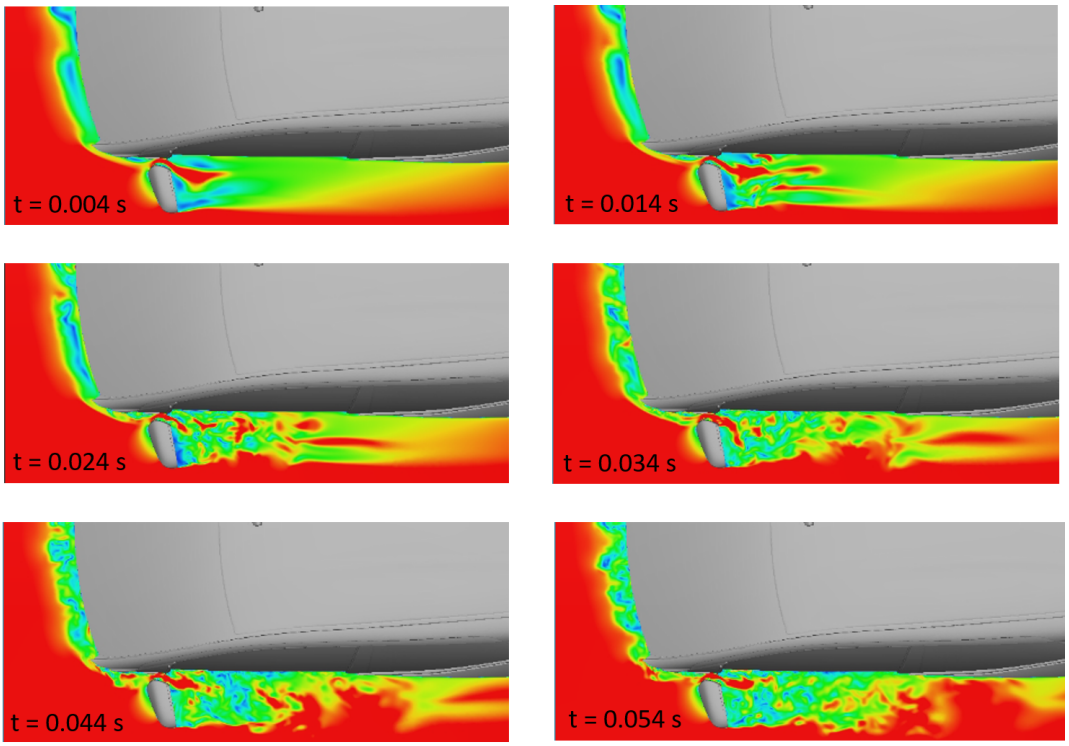

Figure 4.39: *Application to a Production Car. Six different snapshots of the velocity magnitude field based on the DDES model on a horizontal section plane passing through the middle of the side mirror.*

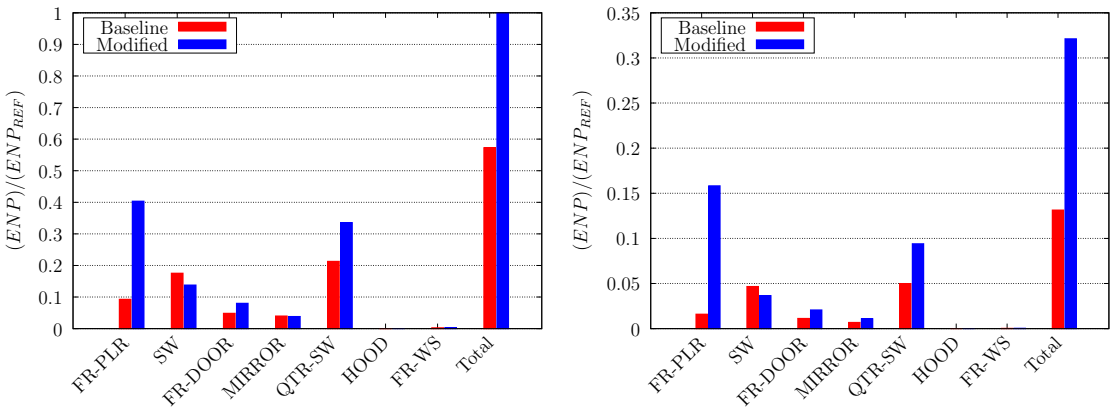

(a) $500 - 4000Hz$ **(b)** $1000Hz$

Figure 4.41: *Application to a Production Car. Comparison of ENP contribution of each part at the frequency range of 500-4000Hz and at 1000 Hz. The ENP results are scaled with the value of the Total ENP at 500-4000 Hz.*

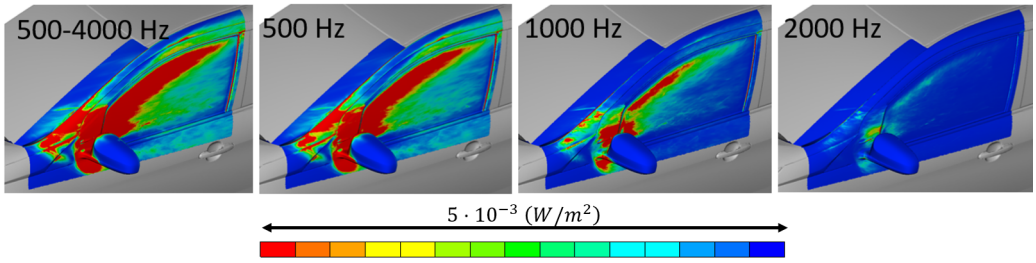

(a) *Baseline*

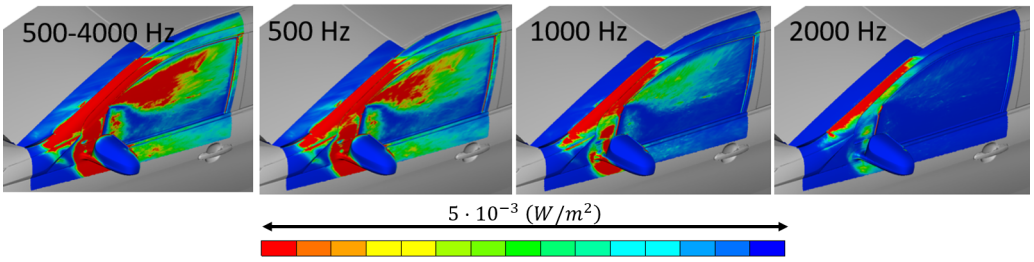

(b) *Modified*

Figure 4.42: *Application to a Production car. ENPD at 500-4000Hz, 500Hz, 1KHz, 2KHz.*

The distribution of ENPD shown in fig. 4.41, between the different parts of the geometry is visualized on the ENPD map (fig. 4.43) at 1000 Hz. This map is computed as a product of the pressure fluctuations spectrum and the UAdjacent velocity. Based on this, the study of its components (figs. 4.44, 4.45) gives some insight on the noise source mechanisms.

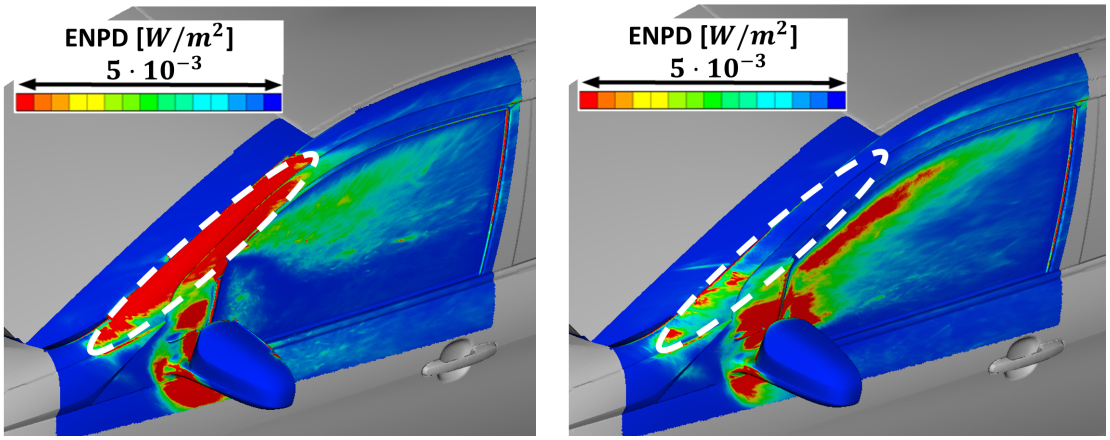

(a) *Modified* **(b)** *Baseline*

Figure 4.43: *Application to a Production Car. A comparison of the ENPD map at* 1000 *Hz, between the modified and the baseline geometry. The highlighted area is the area of the higher ENPD values of the modified geometry.*

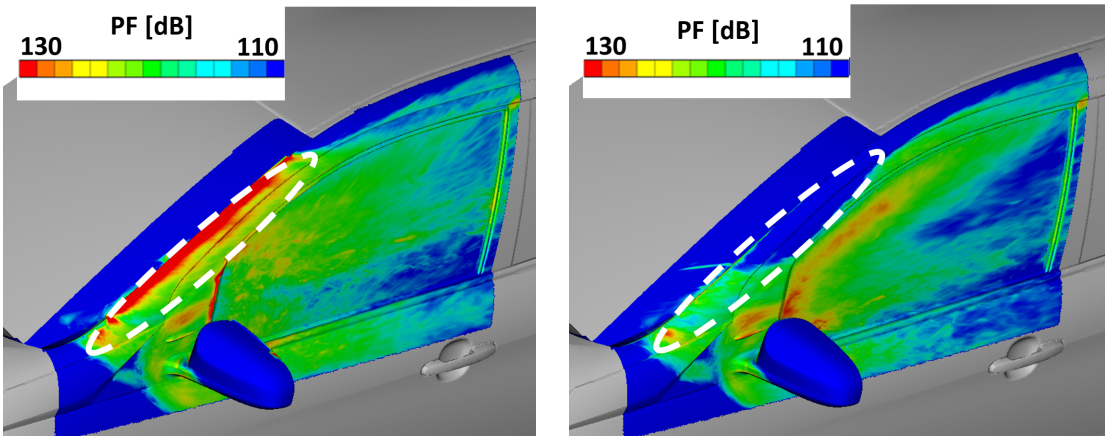

(a) *Modified* **(b)** *Baseline*

Figure 4.44: *Application to a Production Car. A comparison of the PF map at* 1000 *Hz, between the modified and the baseline geometry. The highlighted area is the area of the higher ENPD values of the modified geometry.*

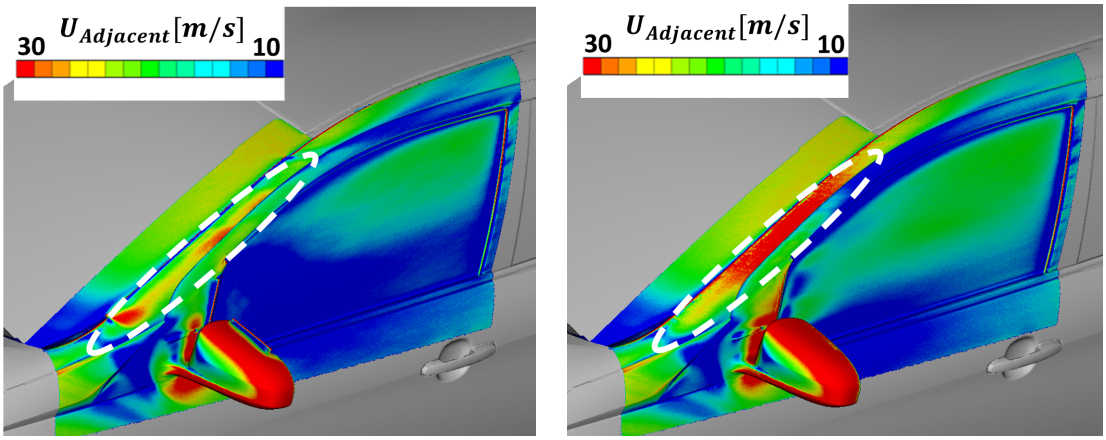

(a) *Modified* **(b)** *Baseline*

Figure 4.45: *Application to a Production Car. A comparison of the UAdjacent velocity map, between the modified and the baseline geometry. The highlighted area is the area of the higher ENPD values of the modified geometry.*

In fig. 4.46, the change in the ENP index from the modified to the baseline geometry is compared with the interior noise[2] change and the change in the beamforming measurements[3]. The trend of the change is the same for all the indices (interior,

[2]The interior noise is measured with a microphone close to the driver's ear inside the cabin. The value compared is the power spectrum value at the frequency band of interest (Appendix A.2).

[3]Beamforming is an experimental technique which measures the sound on the farfield with a set of microphones and using an algorithm, describing sound propagation, "back-propagates" the noise on a plane close to the geometry of interest, coloring it with respect to its noise source intensity (Appendix A.1).

Beamforming and ENP), a difference being noticed in the absolute value of the change and of noise level itself.

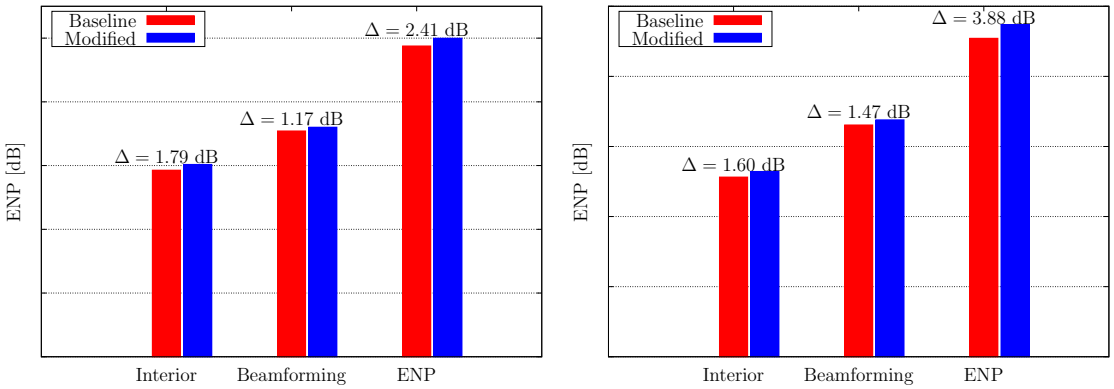

(a) $500 - 4000Hz$ **(b)** $1000Hz$

Figure 4.46: *Application to a Production Car. Comparison of total Interior noise, beamforming integrated value and ENP between the baseline (red) and the modified geometry (blue).*

Chapter 5

Summary - Conclusions

5.1 Summary

In this thesis, two aeroacoustic methods are programmed in the openFOAM environment and their validity is tested. The two methods are the Curle's Integral Method and the Exterior Noise Power (ENP) method. Both, methods require the unsteady pressure fluctuation on the surface of the body to be known. For the acquisition of these unsteady data, the DDES-SA model is used.

Each method is applied to a different case. In the first case, the "Generic Side Mirror on a Flat Plate", the Curle's integral is used to predict the noise on five mid-field receiver locations, for which the Sound Pressure Level (SPL) is compared with experimental data. Side to that, the hydrodynamic pressure fluctuation on the surface of the mirror and plate, computed by the DDES model, are also compared with measurements. For this computation, two numerical schemes for the momentum equation are tested, the linearUpwind and the limitedLinear.

The second case presented is an application of the ENP method to a Production Car. In this case, the baseline geometry of the car and a modification of the former are tested. An unsteady DDES simulation is conducted for both of them, and based on the unsteady pressure fluctuation data acquired, the ENPD source map and the ENP index are computed.

5.2 Conclusions

Through the extended analysis of the two simulated cases and the study of the two methods some conclusions are derived.

Curle's Integral Method

For the Curle's Integral method, it was proven through comparison with the experimental data that:

- The DDES-SA model, is able to predict the unsteady pressure fluctuation on an aerodynamic body, up to a certain frequency.
- The linearUpwind and the limitedLinear scheme tested, show similar behavior in predicting the power distribution of the unsteady pressure fluctuations on the frequency domain, with the linearUpwind scheme being slightly better.
- The simplified version of the Curle's integral, accounting only for the pressure and its time derivative on the surface of the body is proven to be accurate in the Generic Mirror case. The compared SPL spectrum matches the experimental data for most of microphone positions.
- The simplified version of the Curle's integral can be used as a model to predict mid-far field radiated noise, induced by simple geometries in flow of low Mach high Reynolds numbers.

ENP Method

Upon applying the ENP Method on a Production car some statements for the method can be made:

- At first, ENP index is able to qualitatively capture the increase or decrease of the far field radiated noise as a result of a shape modification. This was proven through comparison of the ENP value, computed for the two geometries and, with interior noise measurements and far-field measurements of the beamforming technique. The change in these three indices, has the same sign and similar magnitude.
- The ENPD source intensity map serves as a useful tool in the understanding of the mechanisms behind noise generation.

5.3 Proposals for Future Work

Finally, some matters regrading the future use and improvement of the methods are mentioned:

- The effect of the neglected terms of Curle's analogy can be measured and quantified.
- The Curle's integral method can be tested on more detailed geometries.
- The effect of the grid size to mesh cut-off frequency can be studied.
- A different approach could be used to model the local convective mean velocity, used in the ENP model to make it independent of the mesh.
- Further validation of the current implementation of the ENP method could be done, through comparison with the previous implementation of the method by TMC.
- The continuous adjoint method [36],[37],[38],[39] to the ENP model, as a tool to compute the sensitivity derivatives of the ENP index with respect to the geometry shape can be used. This tool could be used to optimize production cars for low noise emissions.

Appendix A

Experimental Methods in Acoustics

A.1 Phased Array Beamforming technique

A.1.1 General

Beamforming is an experimental technique used to locate acoustic sources, utilizing a microphone array [40]. A microphone array is a set of microphones, the signals of which are combined in such a way that sound from a specified point is amplified and sound from other directions is attenuated, taking advantage of the phase difference of the signals. A benefit of the use of a microphone array over other sound localization techniques is the short measurement time needed, keeping in the same time the noise source resolution high. During the measurements, each one of microphones records a signal and, then, an algorithm is responsible to back propagate the sound on a plane and color it with respect to the source noise intensity level.

In all phased array beamforming algorithms, a model is needed to describe the source characteristics and propagation. In the simplest case this model can be the convective wave equation, under the assumption of planar wave propagation of the noise,

$$\nabla^2 p - \frac{1}{\alpha_\infty^2}\big(\frac{\partial}{\partial t} + \vec{U}\cdot\nabla\big)^2 p = 0 \tag{A.1}$$

where α_∞ is the speed of sound and the sound is assumed to propagate through a medium with uniform flow $\vec{U}$.

The above model is the simplest one. For the majority of the cases a higher accuracy model is needed, so enhanced models with monopole, dipole and quantrupole point source descriptions are used to model the noise propagation. Some models also, account for the effect of the wind tunnel shear layer and for possible reflections on the tunnel's ground, increasing further the accuracy.

Given the model for the noise propagation, the algorithm solves a minimization problem for the objective function

$$J = |p - \alpha g(\vec{\xi_i})| \tag{A.2}$$

which represents the absolute difference of the measured noise signals on the microphone array p with the model description of that signal g. This is solved for every discrete point $\vec{\xi_i}$ on the source plane of choice, giving values to the source amplitude α. Coloring the pixels of an image representing the source plane with different colors of a palette regarding the values of α, a map for the sources of noise is acquired.

A.1.2 S2A GIE Wind Tunnel Beamforming Configuration

In fig. A.1 the experimental setup that supports the beamforming acoustic testing on the S2A GIE acoustic windtunnel in France is presented. The current setup consists of 64 microphones on the side/vertical array and 88 microphones on the top/horizontal array. The frequency range of the output acoustic intensity map is 630-8000 Hz and the source separation capability is 17 cm at 2KHz. The two planes available for noise source localization are presented on figure A.2.

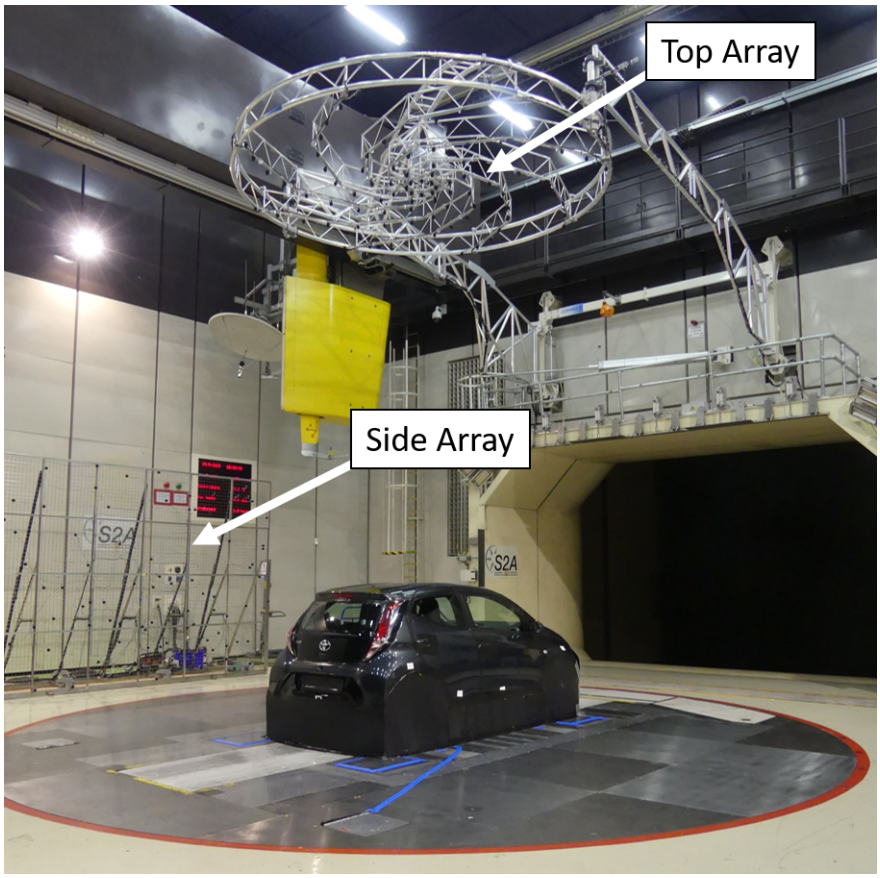

Figure A.1: *A view of the two microphone arrays, top and side, of the S2A GIE windutnnel.*

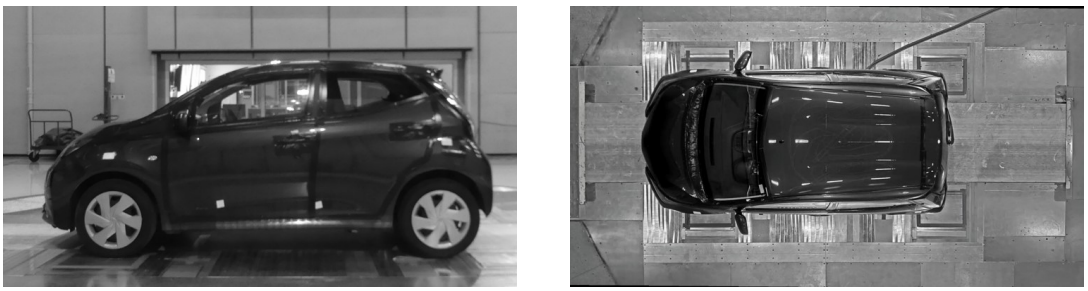

Figure A.2: *The two planes available for noise source localization; side plane A1(left) and top plane A2(right).*

A.1.3 Integration of Beamforming Map

For comparison of different geometry configurations according to their radiating noise, except from comparison the resulting noise source maps, a single value for

each frequency can be extracted integrating the sound intensity in a sub-area of the map. The integration area, that is being used in this thesis is presented in fig. A.3.

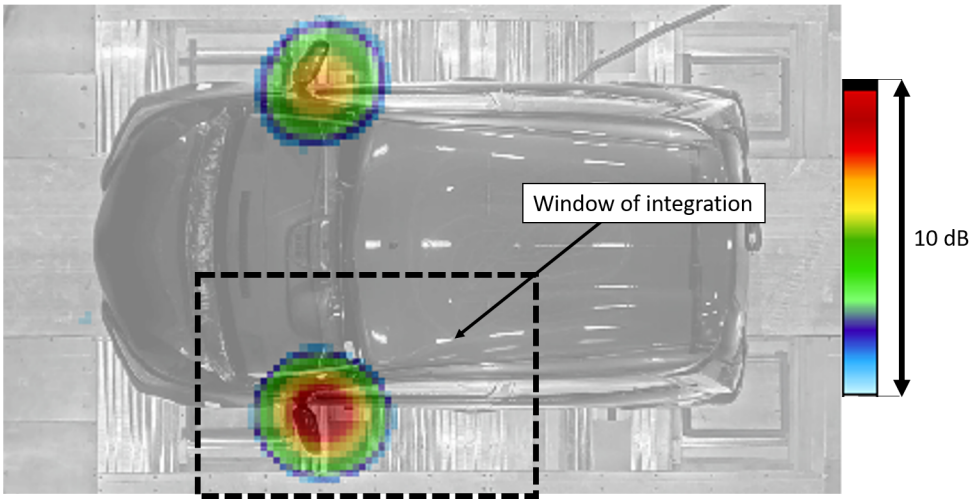

Figure A.3: *A view of the noise intensity map, produced by the phased array beamforming technique at* 1000 *Hz frequency band. The figure also presents the window of integration, used to extract one value for the beamforming map per frequency band.*

A.2 Interior Noise Measurements

The interior noise results is acquired through measurements with a microphone close to the driver's ear. The setup used is presented in fig. A.4

Figure A.4: *A view of the microphone position in the interior of the car, close to driver's left ear. From [35].*

Appendix B

Sensors and microphone positions

The following tables give the location of the sensors and the microphones, used in the "Generic Mirror on a Flat Plate" case. The origin of the coordinate system is on the symmetry plane at the base of the mirror front face.

Positions of the instantaneous pressure sensors			
Sensor Id	x	y	z
S111	0.5D	0.61D	0.425D
S114	0.5D	0.61D	-0.425D
S116	-0.6D	0	0
S119	1D	0	0
S121	1.4945D	0	-0.6045D
S122	1.992D	0	-0.657D
S123	2.389D	0	-0.709D

Positions of the microphones			
Mic Id	x	y	z
M1	-1.24D	2.23D	1.2345D
M4	0.5D	1D	-2.5D
M10	2.265D	2.729D	0
M11	2.265D	2.23D	-1.2345D
M14	0.5D	8.075D	-7.1725D

Positions of mean pressure sensors over mirror			
Sensor Id	x	y	z
S1	0.468D	0.3335D	-0.499D
S2	0.468D	0.6665D	-0.499D
S3	0.468D	0.8335D	-0.499D
S4	0.468D	1D	-0.499D
S5	0.468D	1.129D	-0.482D
S6	0.468D	1.2495D	-0.432D
S7	0.468D	1.432D	-0.2495D
S8	0.468D	1.482D	-0.129D
S9	0.468D	1.499D	0
S10	0.3705D	1.483D	0
S11	0.25D0	1.433D	0
S12	0.1465D	1.3535D	0
S13	0.067D	1.25D	0
S14	0.017D	1.1295D	0
S15	0	1D	0
S16	0	0.833D	0
S17	0	0.6665D	0
S18	0	0.5D	0
S19	0	0.3335D	0
S20	0	0.1665D	0
S21	0.017D	0.6665D	-0.1295D
S22	0.067D	0.6665D	-0.25D
S23	0.1465D	0.6665D	-0.3535D
S24	0.25D	0.6665D	-0.433D
S25	0.3705D	0.6665D	-0.483D
S26	0.5D	0.75D	0.425D
S27	0.5D	1.4215D	-0.0555D
S28	0.5D	1.337D	-0.2585D
S29	0.5D	1.0555D	-0.4215D
S30	0.5D	0.75D	-0.425D
S31	0.5D	0.25D	-0.425D
S32	0.5D	0.25D	0
S33	0.5D	1D	0
S34	0.5D	1.25D	0

Bibliography

[1] J. Delfs: *Lecture notes in Grundlagen der Aeroakustik(Basics of Aeroacoustics)*. DLR, October 2016.

[2] N. Oettle and D. Sims-Williams: *Automotive aeroacoustics: An overview*. In Proceedings of the Institution of Mechanical Engineers, Part D: Journal of Automobile Engineering, 231(9):1177–1189, 2017.

[3] Wikibooks: *Aeroacoustics/acoustic sources — wikibooks, the free textbook project*, 2018. https://en.wikibooks.org/w/index.php?title=Aeroacoustics/Acoustic_Sources&oldid=3469573, [Online; accessed 13-February-2019].

[4] A.D. Pierce: *Acoustics: An Introduction to Its Physical Principles and Applications*. Acoustical Society of America, 1989.

[5] D. A. Russell, J. P. Titlow, and Ya Juan Bemmen: *Acoustic monopoles, dipoles, and quadrupoles: An experiment revisited*. American Journal of Physics, 67(8):660–664, 1999.

[6] N. Oettle: *The Effects of Unsteady On-Road Flow Conditions on Cabin Noise*. PhD thesis, School of Engineering and Computing Sciences, Durham University, Durham, UK, 2013.

[7] F. Vanherpe, D. Baresh, Ph. Lafon, and M. Bordji: *Wavenumber-frequency analysis of the wall pressure fluctuations in the wake of a car side mirror*. In the 17th AIAA/CEAS Aeroacoustics Conference (32nd AIAA Aeroacoustics Conference). Portland, Oregon., 2011.

[8] F. Vanherpe, L. Olivas Duarte, and Ph. Lafon: *Sound vs. pseudo-sound contributions to the wind noise*. In the 18th AIAA/CEAS Aeroacoustics Conference (33rd AIAA Aeroacoustics Conference). Colorado Springs, CO., June 2012.

[9] R. Rizzuto, N. Paola, L. M. Lorefice, E. M. Ribaldone, and A. Barella: *Aeroacoustics in the automotive industry: a cost-efficient approach to flow induced noise simulation*. In International Conference on Vehicle Aerodynamics 2016: Aerodynamics by Design, Coventry, UK, September 21-22 2016.

[10] D. Blanchet and A. Golota: *Combining modeling methods to accurately predict wind noise contribution.* In *SAE Technical Paper*. SAE International, June 2015.

[11] P. Davidson: *Turbulence: An Introduction for Scientists and Engineers*. Oxford University Press, Oxford, 2015.

[12] J.M. McDonough: *Introductory Lectures on Turbulence*. Departments of Mechanical Engineering and Mathematics, University of Kentucky, 2007.

[13] Ph. Spalart and S. Allmaras: *A one-equation turbulence model for aerodynamic flows*. AIAA Paper 1992-439, 30th Aerospace Sciences Meeting and Exhibit, Reno, Nevada, USA, January 6–9 1992.

[14] A. Leonard: *Energy cascade in large-eddy simulations of turbulent fluid flows*. In *Turbulent Diffusion in Environmental Pollution*, pages 237–248, 1974.

[15] E. de Villiers: *The Potential of Large Eddy Simulation for the Modeling of Wall Bounded Flows*. PhD thesis, Thermofluids Section Department of Mechanical Engineering, Imperial College of Science, Technology and Medicine, London, July 2006.

[16] E. Garnier, N. Adams, and P. Sagaut: *Large Eddy Simulation for Compressible Flows*. Scientific Computation Series. Springer Netherlands, 2009.

[17] Ph. Spalart, W H Jou, M. Strelets, and S. Allmaras: *Comments on the feasibility of les for wings, and on a hybrid rans/les approach*. In *International Conference on DNS/LES, Aug. 4-8, 1997, Ruston, Louisiana.*, 1997.

[18] J. Fröhlich and D. von Terzi: *Hybrid LES/RANS methods for the simulation of turbulent flows*. In Progress in Aerospace Sciences Journal, 44(5):349 – 377, 2008.

[19] P. R. Spalart, S. Deck, M. L. Shur, K. D. Squires, M. Kh. Strelets, and A. Travin: *A new version of detached-eddy simulation, resistant to ambiguous grid densities*. In Theoretical and Computational Fluid Dynamics Journal, 20(3):181, May 2006.

[20] M. J. Lighthill, M. Herman, and A. Newman: *On sound generated aerodynamically i. general theory*. In Proceedings of the Royal Society of London. Series A. Mathematical and Physical Sciences, 211(1107):564–587, 1952.

[21] N. Curle and M. J. Lighthill: *The influence of solid boundaries upon aerodynamic sound*. In Proceedings of the Royal Society of London. Series A. Mathematical and Physical Sciences, 231(1187):505–514, 1955.

[22] J. E. Ffowcs Williams, D. L. Hawkings, and M. J. Lighthill: *Sound generation by turbulence and surfaces in arbitrary motion*. Philosophical Transactions of the Royal Society of London. Series A, Mathematical and Physical Sciences, 264(1151):321–342, 1969.

[23] J. Larsson: *Computational Aero Acoustics for Vehicle Applications*. Licentiate thesis, Departmet of Thermal and Fluid Dynamics, Chalmers University of Technology, Goteborg, Sweden, 2002.

[24] S. Sarkar and M. Y. Hussaini: *Computation of the acoustic radiation from bounded homogeneous flows*. In Jay C. Hardin and M. Y. Hussaini (editors): *Computational Aeroacoustics*, pages 335–355, New York, NY, 1993. Springer New York.

[25] V. Phan, H. Tanaka, T. Nagatani, M. Wakamatsu, and T. Yasuki: *A cfd analysis method for prediction of vehicle exterior wind noise*. SAE International Journal, Passeng. Cars - Mech. Syst., 10:286–298, March 2017.

[26] ISO 9614-1:1993: *Acoustics – determination of sound power levels of noise sources using sound intensity - part 1: Measurement at discrete points*. Standard, International Organization for Standardization, June 1993.

[27] S. Chernenko: *Librow - Fast Fourier Transform (FFT)*. http://www.librow.com/articles/article-10, [Online; accessed 18-February-2019].

[28] P. Welch: *The use of fast fourier transform for the estimation of power spectra: A method based on time averaging over short, modified periodograms*. IEEE Transactions on Audio and Electroacoustics, 15(2):70–73, June 1967.

[29] J. Ask and L. Davidson: *The sub-critical flow past a generic side mirror and its impact on sound generation and propagation*. In the 12th AIAA/CEAS Aeroacoustics Conference (27th AIAA Aeroacoustics Conference). Cambridge, Massachusetts., May 2006.

[30] J. Ask and L. Davidson: *A numerical investigation of the flow past a generic side mirror and its impact on sound generation*. Journal of Fluids Engineering, 131(6), May 2009.

[31] R. Powell, P. Moron, G. Balasubramanian, and B. Neuhierl et al: *Simulation of underbody contribution of wind noise in a passenger automobile*. SAE International Journal, Passeng. Cars - Mech. Syst., 6:1251–1261, May 2013.

[32] A. Kabat Vel Job and J. Sesterhenn: *Prediction of the interior noise level for automotive applications based on time-domain methods*. In Proceedings of the INTER-NOISE and NOISE-CON Congress and Conference, 253(2):6000–6010, 2016.

[33] B. Neuhierl, D. Schroeck, S. Senthooran, and P. Moron: *A computational aeroacoustic study of windshield wiper influence on passenger vehicle greenhouse windnoise*, June 2014.

[34] H. Yao, Z. Chroneer, and L. Davidson: *Simplifications applied to simulation of turbulence induced by a side view mirror of a full-scale truck using des*, April 2018.

[35] *S2A Wind Tunnels - Souffleries Aeroacoustiques Automobiles*. https://www.soufflerie2a.com/en/, [Online; accessed 26-February-2019].

[36] I.S. Kavvadias, E.M. Papoutsis-Kiachagias, and K.C. Giannakoglou: *On the proper treatment of grid sensitivities in continuous adjoint methods for shape optimization*. Journal of Computational Physics, 301:1–18, 2015, ISSN 0021-9991.

[37] D. I. Papadimitriou and K. C. Giannakoglou: *A continuous adjoint method with objective function derivatives based on boundary integrals for inviscid and viscous flows*. Computers & Fluids, 36(2):325–341, 2007.

[38] A.S. Zymaris, D.I. Papadimitriou, K.C. Giannakoglou, and C. Othmer: *Continuous adjoint approach to the spalart-allmaras turbulence model for incompressible flows*. Computers & Fluids, 38(8):1528 – 1538, 2009, ISSN 0045-7930.

[39] E. M. Papoutsis-Kiachagias and K. C. Giannakoglou: *Continuous adjoint methods for turbulent flows, applied to shape and topology optimization: Industrial applications*. Archives of Computational Methods in Engineering, 23(2):255–299, 2016, ISSN 1886-1784.

[40] P. Sijtsma: *Phased array beamforming applied to wind tunnel and fly-over tests*. In *SAE Technical Paper*. SAE International, October 2010.

Εθνικό Μετσόβιο Πολυτεχνείο
Σχολή Μηχανολόγων Μηχανικών
Τομέας Ρευστών
Μονάδα Παράλληλης Υπολογιστικής Ρευστοδυναμικής & Βελτιστοποίησης

Προγραμματισμός της Ακουστικής Αναλογίας του Curle και του Μοντέλου ENP για την Πρόλεξη του Αεροδυναμικά Επαγόμενου Εξωτερικού Θορύβου από Γεωμετρίες Αυτοκινήτου

Διπλωματική Εργασία

Ανδρέας Σπυρόπουλος

Επιβλέπων: Κυριάκος Χ. Γιαννάκογλου, Καθηγητής ΕΜΠ

Αθήνα, 2019

ΕΚΤΕΝΗΣ ΠΕΡΙΛΗΨΗ ΣΤΑ ΕΛΛΗΝΙΚΑ

Εισαγωγή

Τα τελευταία χρόνια, ο θόρυβος στα επιβατηγά αυτοκίνητα απο πηγές όπως ο κινητήρας και το σύστημα μετάδοσης κίνησης έχει μειωθεί αισθητά, αναδεικνύοντας άλλες πηγές θορύβου όπως ο αεροδυναμικά επαγόμενος, ο οποίος σε υψηλές ταχύτητες κυριαρχεί στο εσωτερικό. Δεδομένης της σημασίας του θορύβου στην ασφάλεια και την άνεση των επιβατών, η αξιολόγηση και η κατανόηση αυτών των αεροδυναμικών πηγών θορύβου αποτελεί καθοριστικό παράγοντα στην ανάπτυξη ποιοτικών και ανταγωνιστικών αυτοκινήτων.

Σκοπός αυτής της διπλωματικής εργασίας είναι ο προγραμματισμός και η πιστοποίηση γρήγορων και αξιόπιστων μεθόδων για την αξιολόγηση του αεροδυναμικού θορύβου επιβατηγών οχημάτων. Στην κατεύθυνση αυτή, προγραμματίστηκαν δύο υβριδικές μέθοδοι για την αξιολόγηση του εξωτερικού θορύβου, η αναλογία του Curle και το μοντέλο ENP. Και οι δύο μέθοδοι προϋποθέτουν τον εκ των προτέρων υπολογισμό και αποθήκευση της μη-μόνιμης πίεσης στην επιφάνεια του σώματος.

Το μοντέλο DDES

Ως πρώτο στάδιο και των δύο μεθόδων, επιλύεται η μη-μόνιμη τυρβώδης ροή με χρήση του υβριδικού μοντέλου DDES-SA [1]. Η υβριδοποίηση έγκειται στην επίλυση ττων Reynolds-Averaged Navier Stokes εξισώσεων κοντά στον τοίχο και των Large Eddy Simulation μακρυά, πετυχαίνοντας έτσι γρήγορη και υψηλής ακρίβειας επίλυση του μη-μόνιμου πεδίου. Συνδετικός κρίκος των δύο, είναι το μοντέλο Spalart-Allaras, το

οποίο λειτουργεί είτε στη συνήθη μορφή του είτε ώς ένα Συβ-Γριδ Σγαλε μοντέλο σε συνδιασμό με τις LES εξισώσεις. Εκτενέστερη αναφορά γίνεται στο κυρίως κείμενο της εργασίας στην αγγλική γλώσσα.

Αναλογία του Curle

Η πρώτη μέθοδος που προγραμματίστηκε, αποτελεί μία απλοποιημένη εκδοχή της αναλογίας του Curle [2] για ροές χαμηλού αριθμού Mach και υψηλού αριθμού Reynolds. Για αυτές τις περιπτώσεις, η ακουστική πίεση σε έναν απομακρυσμένο ακροατή στο $\vec{x}$ σε χρόνο t δίνεται από την ολοκλήρωση ισοδύναμων ακουστικών πηγών στην επιφάνεια του σώματος S, εκφρασμένες συναρτήσει της πίεσης p και της χρονικής της παραγώγου $\dot{p}$, ως

$$p(\vec{x},t) - p_0 = \frac{1}{4\pi}\int_S l_i n_i \left[\frac{\dot{p}}{\alpha_\infty r} + \frac{p}{r^2}\right] dS(\vec{y}) \tag{1}$$

όπου n το μοναδιαίο κάθετο διάνυσμα στην επιφάνεια του σώματος, l το μοναδιαίο διάνυσμα με κατεύθυνση από το σημείο ολοκλήρωσης $\vec{y}$ στην επιφάνεια προς τον ακροατή $\vec{x}$, r η απόσταση $\vec{y}$ και ακροατή $\vec{x}$ και α_∞ η ταχύτητα του ήχου.

Μέθοδος ENP

Η δεύτερη μέθοδος υπολογίζει τη συνολική ακουστική ισχύ του αεροδυναμικά επαγόμενου θορύβου [3], που εκπέμπεται στο επ΄ άπειρο όριο. Για μία ζώνη συχνοτήτων με κεντρική συχνότητα f, αυτή δίνεται από την σχέση

$$\overline{W}_f = \int_{S_W} \frac{\pi^2 k^2 P(\vec{y})_f^2 \overline{U}(\vec{y})^2}{12\rho\alpha_\infty^3} dS(\vec{y}) \tag{2}$$

όπου $P(\vec{y})_f^2$ η τιμή του φάσματος ισχύος στην ζώνη υπολογισμού, $\overline{U}(\vec{y})$ η μέση ταχύτητα κοντά στον τοίχο, με την οποία μεταφέρονται οι διαταραχές, ρ η πυκνότητα και α_∞ η ταχύτητα του ήχου.

Αυτή η μέθοδος έχει το πλεονέκτημα ότι η ολοκληρωτέα ποσότητα αναπαριστά την ένταση των πηγών θορύβου στην επιφάνεια του σώματος, που αν ‘τυπωθεί’ στην επιφάνεια αποτελεί ένα χρήσιμο εργαλείο οπτικοποίησης. Η διαδικασία που απαιτείται για τον υπολογισμό του δείκτη ENP και του εν λόγω χάρτη των πηγών θορύβου ENPD, παρουσιάζεται στο σχ. 1.

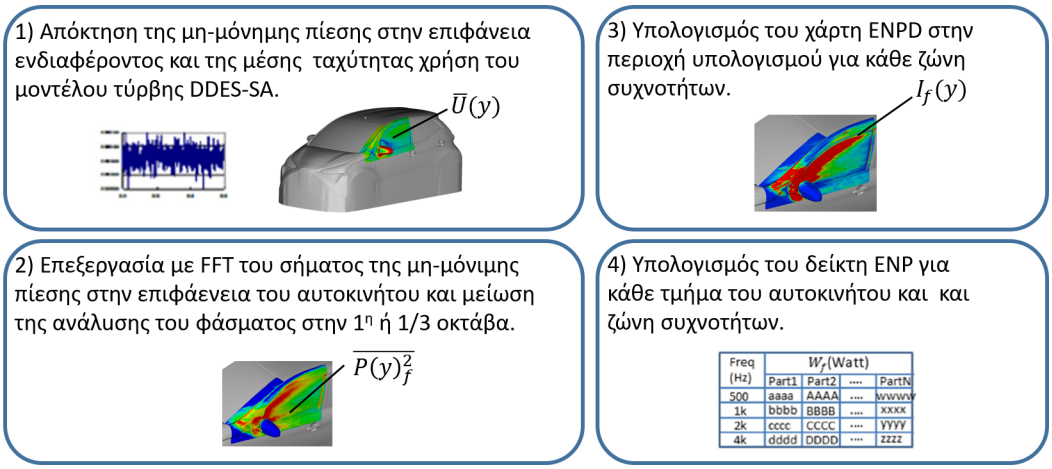

Σχήμα 1: *Διαδικασία υπολογισμού του δείκτη ENP.*

Εφαρμογές

Απλοποιημένος καθρέφτης σε επίπεδη πλάκα

Η πρώτη εφαρμογή, είναι ένας απλοποιημένος καθρέφτης πάνω σε μία επίπεδη πλάκα. Στον πίνακα 1 συγκρίνεται η τιμή του συντελεστή αντίστασης, υπολογισμένου με διάφορα μοντέλα με την τιμή αναφοράς. Έπειτα, παρουσιάζεται σύγκριση του φάσματος ισχύος της μη-μόνιμης πίεσης σε επιλεγμένες θέσεις στην επιφάνεια του καθρέφτη και της πλάκας, υπολογισμένου με το μοντέλο DDES, με πειραματικά δεδομένα και άλλες προσομοιώσεις (σχ. 4). Στο σχ. 6 φαίνεται σύγκριση του φάσματος ισχύος του θορύβου, υπολογισμένου με την αναλογία του Curle με πειραματικά δεδομένα.

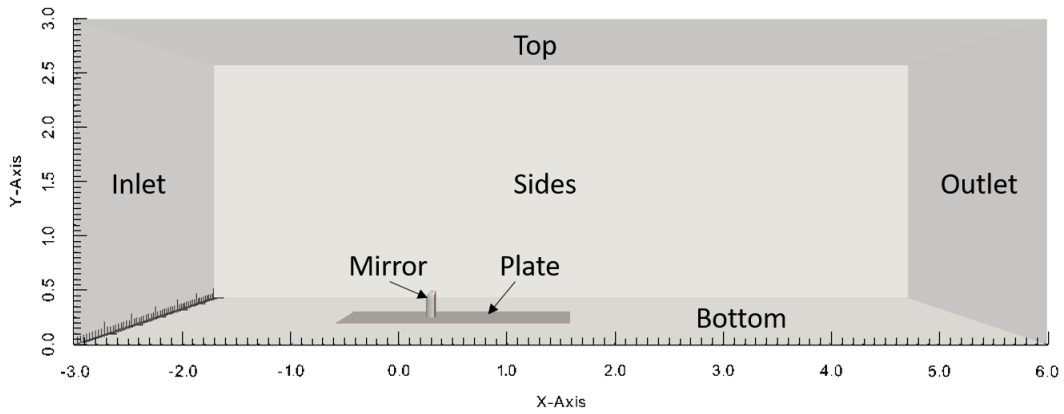

Σχήμα 2: *Απλοποιημένος καθρέφτης σε επίπεδη πλάκα. Η γεωμετρία του καθρέφτη και το χωρίο υπολογισμού.*

	C_D	$\frac{C_D - C_D(ref)}{C_D(ref)}\%$
Ref. value, simulation [4]	0.4437	–
RANS	0.5243	18.17%
URANS	0.4952	11.61%
DDES-linearUpwind	0.45507	2.56%
DDES-limitedLinear	0.43625	1.678%
DDES-DEShybrid	0.4475	0.856%

Πίνακας 1: *Απλοποιημένος καθρέφτης σε επίπεδη πλάκα. Σύγκριση του συντελεστή αντίστασης υπολογισμένου με RANS-SA, URANS-SA και DDES-SA μοντέλο, με την τιμή αναφοράς από την προσομοίωση στην αναφορά [4], όπου χρησιμοποιήθηκε εμπορικό λογισμικό και DES μοντέλο. Δοκιμάζονται τρία σχήματα διακριτοποίησης για την εξίσωση της ορμής με το DDES μοντέλο.*

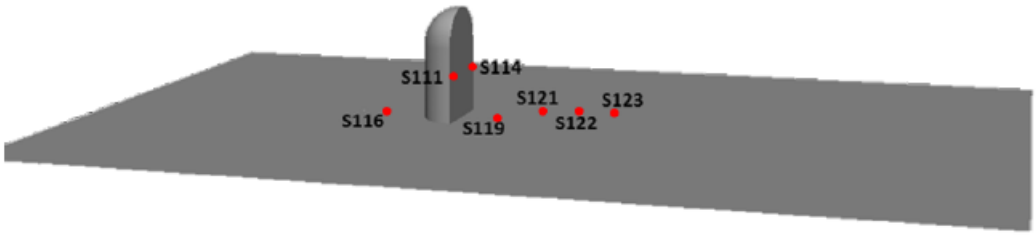

Σχήμα 3: *Απλοποιημένος καθρέφτης σε επίπεδη πλάκα. Η θέση των αισθητήρων πίεσης στην επιφάνεια του καθρέφτη και της επίπεδης πλάκας.*

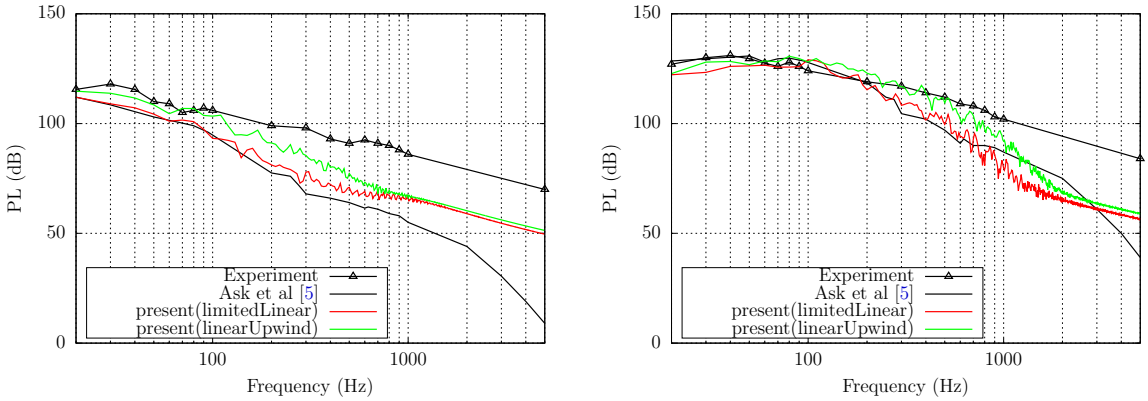

(α′) *Αισθητήρας πίεσης S111*

(β′) *Αισθητήρας πίεσης S121*

(γ′) *Αισθητήρας πίεσης S122*

(δ′) *Αισθητήρας πίεσης S123*

Σχήμα 4: *Απλοποιημένος καθρέφτης σε επίπεδη πλάκα. Φάσμα επιπέδου πίεσης PL (dB) στους αισθητήρες πίεσης στην επιφάνεια S111, S121, S122, S123.*

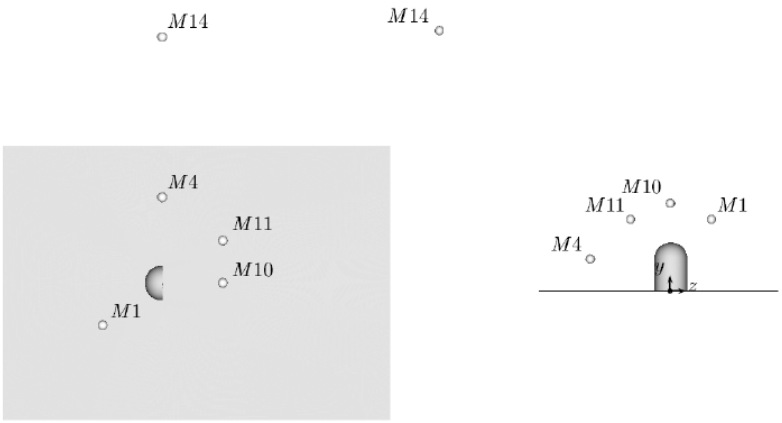

Σχήμα 5: *Απλοποιημένος καθρέφτης σε επίπεδη πλάκα. Η θέση των μικροφώνων στα οποία υπολογίζεται η ακουστική πίεση μέσω της αναλογίας του Curle.*

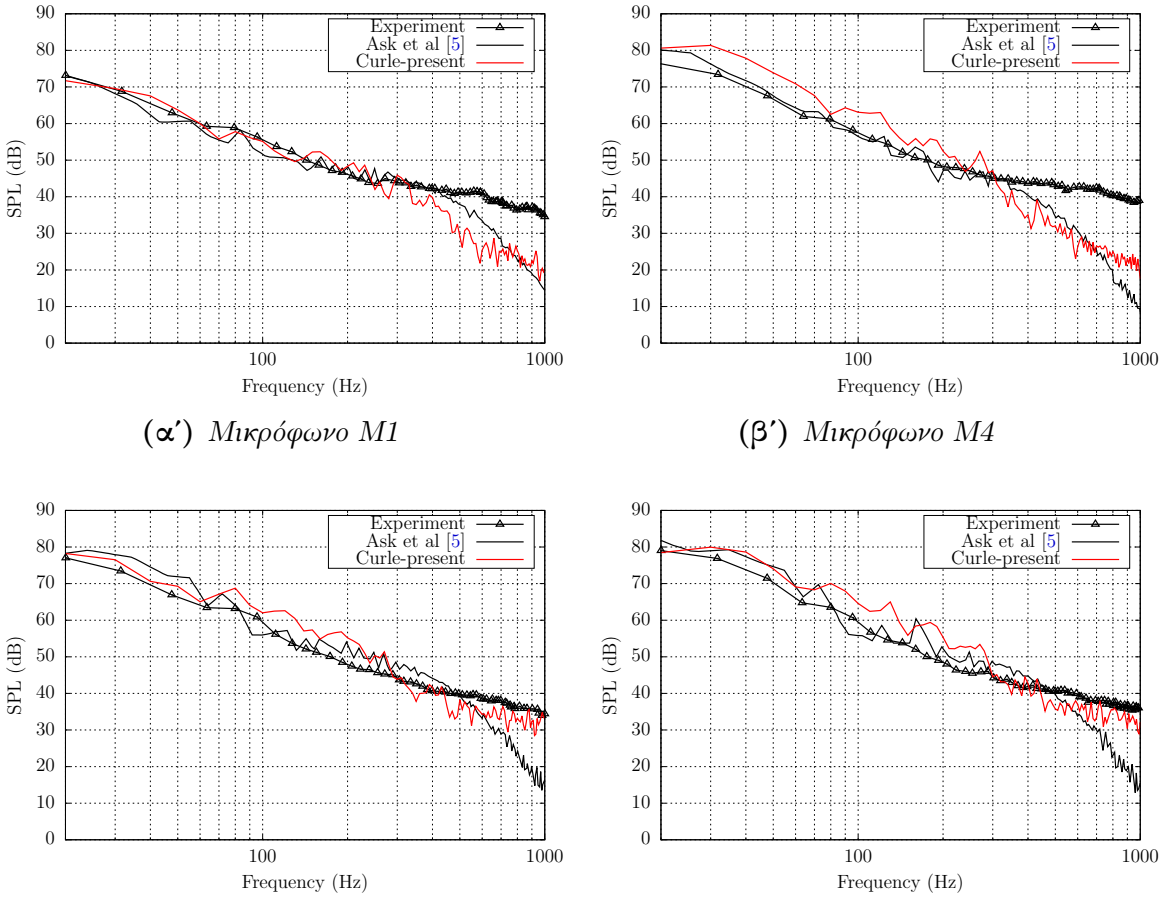

(α′) *Μικρόφωνο M1*

(β′) *Μικρόφωνο M4*

(γ′) *Μικρόφωνο M10*

(δ′) *Μικρόφωνο M11*

Σχήμα 6: *Εφαρμογή σε αυτοκίνητο παραγωγής. Φάσμα επιπέδου ακουστικής πίεσης SPL (dB) στα μικρόφωνα M1, M4, M10, M11.*

Εφαρμογή σε αυτοκίνητο παραγωγής

Στη δεύτερη περίπτωση, προσομοιώνεται η ροή γύρω από μισό αυτοκίνητο (σχ. 7) και η εκπεμπόμενη ισχύς του θορύβου από μία υποπεριοχή του υπολογίζεται μέσω της μεθόδου ENP (σχ. 9). Για την πιστοποίηση της μεθόδου, αυτή εφαρμόζεται σε μία βασική γεωμετρία αυτοκινήτου και σε μια τροποποιημένη με επιπλέον προσθήκη 5 εξογκωμάτων, οι οποίες παρουσιάζονται στο σχ. 8. Η τροποποίηση έχει ως στόχο την παραγωγή θορύβου. Διερευνάται αν η μέθοδος μπορεί να αναγνωρίσει αυτή την αύξηση του θορύβου. Η πιστοποίηση είναι έμμεση· γίνεται σύγκριση της διαφοράς του θορύβου μεταξύ των δύο γεωμετριών, μετρημένη πειραματικά στο εσωτερικό, στο επ΄ άπειρο όριο, μέσω της τεχνικής beamforming με την διαφορά του δείκτη ENP (σχ. 13). Στο σχ. 10 συγκρίνεται ο χάρτης των πηγών θορύβου μεταξύ της βασικής και της τροποποιημένης γεωμετρίας, ενώ στα σχ. 11 και σχ. 12 φαίνονται τα πεδία που δίνουν συνεισφορά στο ENPD. Αυτοί οι χάρτες μπορούν να βοηθήσουν τον μηχανικό να προτείνει τροποποιήσεις για μείωση του θορύβου.

Σχήμα 7: *Εφαρμογή σε αυτοκίνητο παραγωγής. Η προς μοντελοποίηση γεωμετρία του αυτοκινήτου, όπως μετρήθηκε στην αεροσύραγγα.*

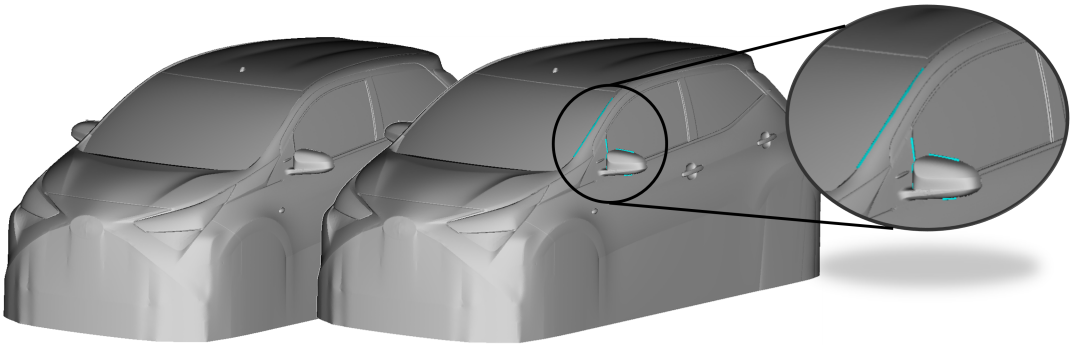

Σχήμα 8: *Εφαρμογή σε αυτοκίνητο παραγωγής. Η γεωμετρία του βασικού αυτοκινήτου (αριστερά) και του τροποποιημένου (δεξιά).*

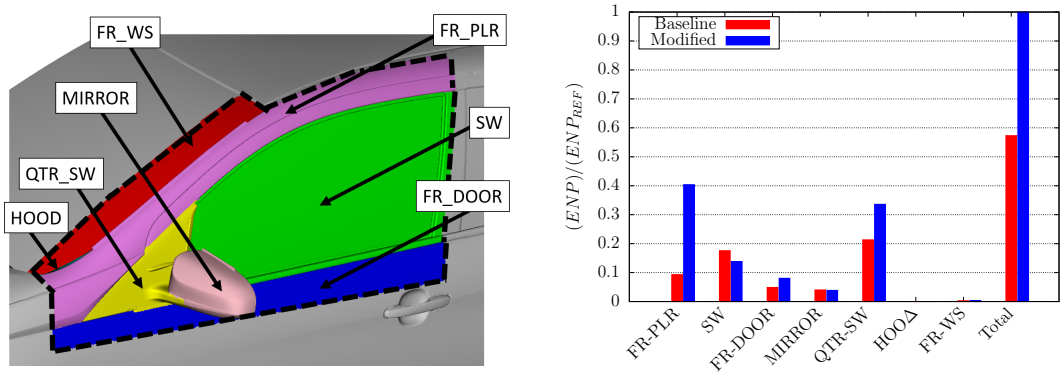

Σχήμα 9: *Εφαρμογή σε αυτοκίνητο παραγωγής. Η περιοχή όπου μελετάται ο αεροδυναμικά επαγόμενος θόρυβος (αριστερά) και η συνεισφορά κάθε μέρους αυτής στον συνολικό δείκτη ENP για την μπάντα* $500 - 4000Hz$ *(δεξιά).*

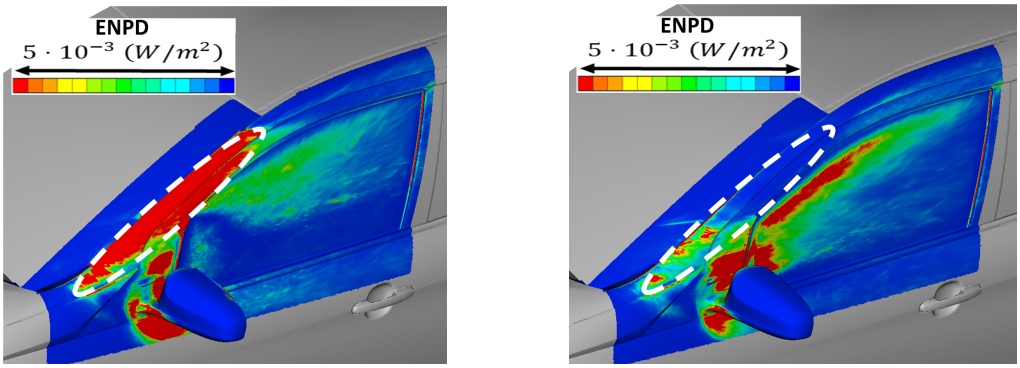

Σχήμα 10: *Εφαρμογή σε αυτοκίνητο παραγωγής. Σύγκριση της έντασης των πηγών θορύβου στην επιφάνεια του αυτοκινήτου στα 1000 Hz της 1ης οκτάβας, μεταξύ της τροποποιημένης (αριστερά) και της βασικής γεωμετρίας (δεξιά).*

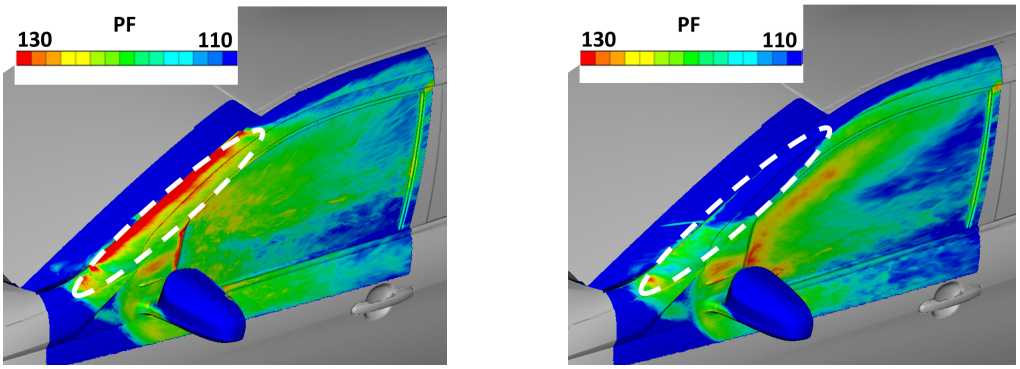

Σχήμα 11: *Εφαρμογή σε αυτοκίνητο παραγωγής. Σύγκριση της έντασης των διαταραχών της πίεσης στην επιφάνεια του αυτοκινήτου στα 1000 Hz της 1ης οκτάβας, μεταξύ της τροποποιημένης (αριστερά) και της βασικής γεωμετρίας (δεξιά).*

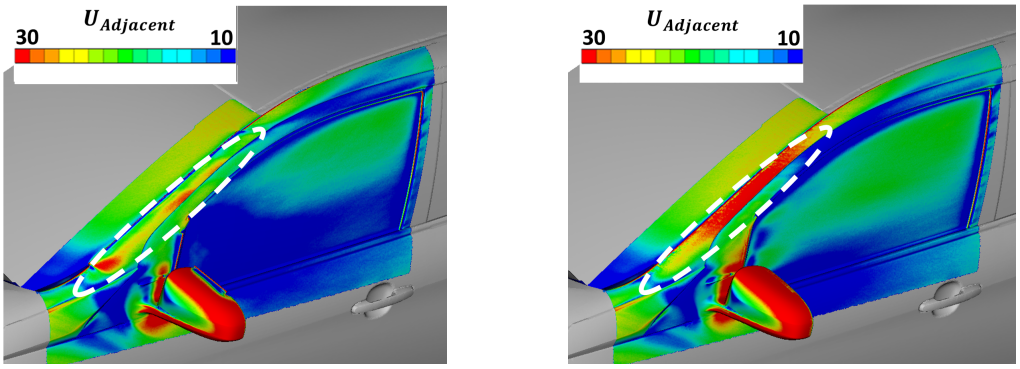

Σχήμα 12: *Εφαρμογή σε αυτοκίνητο παραγωγής. Σύγκριση της μέσης ταχύτητας της ροής στο πρώτο κελί μετά τον τοίχο, μεταξύ της τροποποιημένης (αριστερά) και της βασικής γεωμετρίας (δεξιά).*

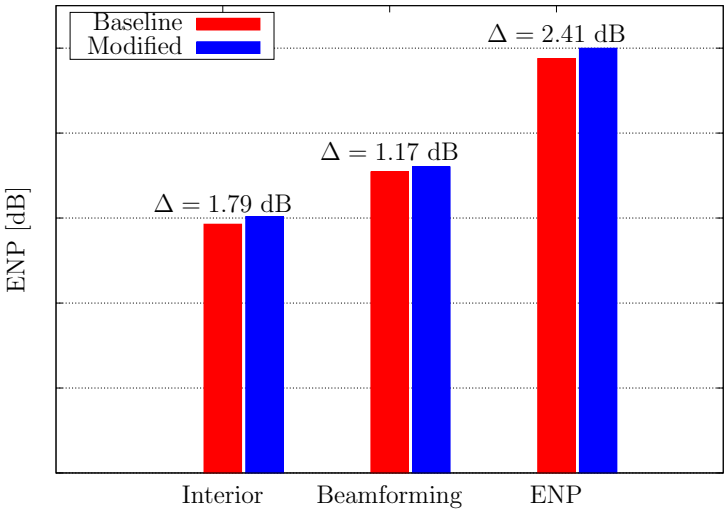

Σχήμα 13: *Εφαρμογή σε αυτοκίνητο παραγωγής. Σύγκριση της μεταβολής του θορύβου ΔdB από την τροποποιημένη γεωμετρία στην βασική στην μπάντα $500-4000$ Hz, μετρημένη στο εσωτερικό του αυτοκινήτου, υπολογισμένη από μετρήσεις στο επ΄ άπειρο όριο (Beamforming) και μέσω του δείκτη ENP.*

Η επιλογή της προσομοίωσης μισού αυτοκινήτου, δικαιολογείται λόγω της συμμετρίας και του μεγάλου υπολογιστικού κόστους στην αντίθετη περίπτωση. Παρόλο που η επιλογή αυτή εισάγει κάποιο σφάλμα στη λύση κοντά στο επίπεδο συμμετρίας, αναμένεται η ροή κοντά στην περιοχή του καθρέφτη να μην επηρεάζεται αισθητά. Αυτό διαπιστώνεται, τουλάχιστον για τα μέσα χρονικά πεδία συγκρίνοντας τα με πειραματικά δεδομένα (σχ 15. Στο σχ. 14 φαίνονται δύο στιγμιότυπα της μη-μόνιμης λύσης στην περιοχή του καθρέφτη.

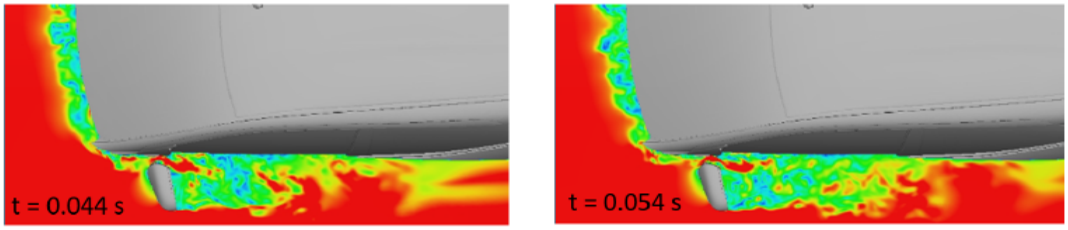

Σχήμα 14: *Εφαρμογή σε αυτοκίνητο παραγωγής. Δύο στιγμιότυπα της μη-μόνιμης ταχύτητας στην περιοχή του καθρέφτη.*

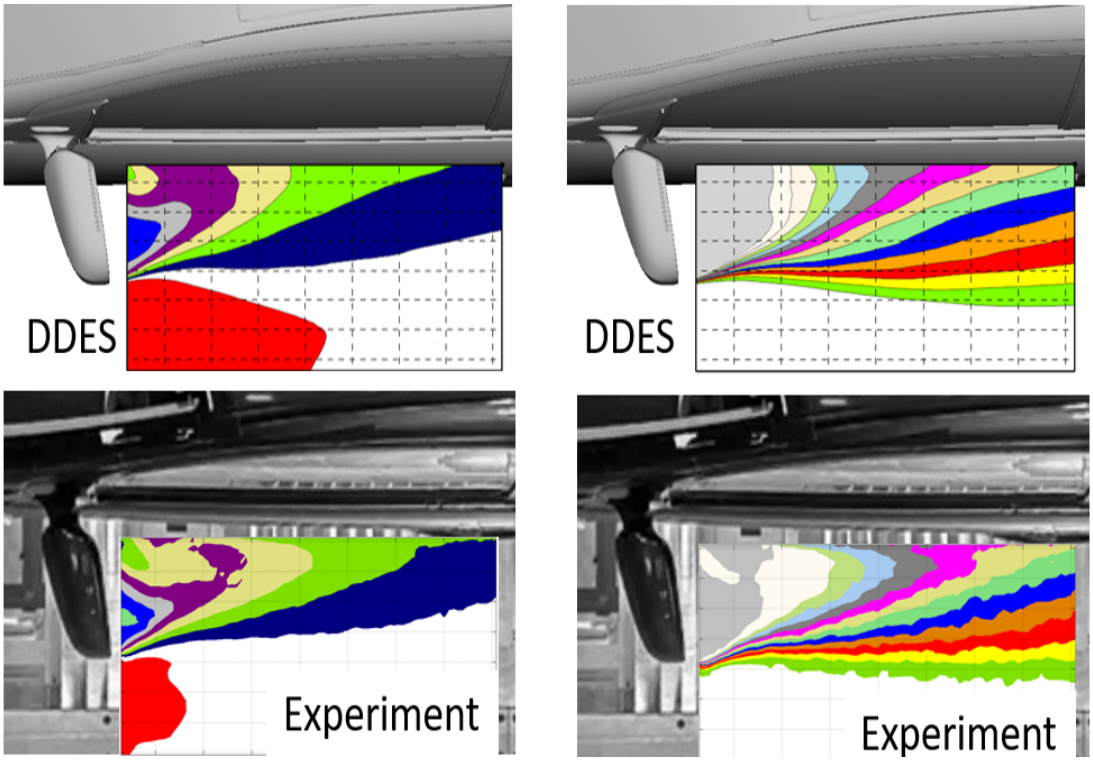

(α′) $\frac{U_x}{U_\infty}$ (β′) $c_{p,total}$

Σχήμα 15: *Εφαρμογή σε αυτοκίνητο παραγωγής. Σύγκριση των μέσων πεδίων της αδιάστατης ταχύτητας στην κατεύθυνση της ροής και του συντελεστής ολικής πίεσης στον ομόρου του καθρέφτη, υπολογισμένων από το μοντέλο DDES και μετρημένων στην αεροσύραγγα.*

Σύνοψη-Σχόλια

Σε αυτήν τη διπλωματική εργασία μελετήθηκε, μέσω των δύο μεθόδων που προγραμματίστηκαν, ο εξωτερικός θόρυβος από γεωμετρίες επιβατηγών οχημάτων. Στην περίπτωση του απλοποιημένου καθρέφτη αποδείχθηκε ότι το DDES μοντέλο είναι ικανό να προβλέψει τη μη-μόνιμη πίεση στην επιφάνεια αεροδυναμικών σωμάτων μέχρι κάποια συχνότητα αποκοπής, μέσω σύγκρισης με πειραματικά δεδομένα. Επίσης, πιστοποιήθηκε η απλοποιημένη αναλογία του Curle σε ορισμένα σημεία στο επ΄ άπειρο όριο. Επόμενο στάδιο για αυτή τη μέθοδο είναι η εφαρμογή της σε μία πιο περίπλοκη γεωμετρία και η διερεύνηση του ύψους συχνότητας αποκοπής σε σχέση με την ανάλυση του πλέγματος. Στην περίπτωση του αυτοκινήτου, πιστοποιήθηκε έμμεσα η μέθοδος ENP, μέσω σύγκρισης της μεταβολής του δείκτη ENP, σε σχέση με την μεταβολή στον εσωτερικό θόρυβο και την μεταβολή στον θόρυβο υπολογισμένο από την τεχνική Beamforming, μεταξύ της τροποποιημένη· και της βασική γεωμετρίας. Η διαφορά σε dB είναι παρόμοια, παρόλο που η απόλυτες τιμές διαφέρουν. Ακόμη, φάνηκε ότι ο χάρτης των πηγών θορύβου αναγνωρίζει τις τροποποιήσεις.

Επιλεγμένη Βιβλιογραφία

[1] P. R. Spalart, S. Deck, M. L. Shur, K. D. Squires, M. Kh. Strelets, and A. Travin: *A new version of detached-eddy simulation, resistant to ambiguous grid densities*. In Theoretical and Computational Fluid Dynamics Journal, 20(3):181, May 2006.

[2] N. Curle and M. J. Lighthill: *The influence of solid boundaries upon aerodynamic sound*. In Proceedings of the Royal Society of London. Series A. Mathematical and Physical Sciences, 231(1187):505–514, 1955.

[3] V. Phan, H. Tanaka, T. Nagatani, M. Wakamatsu, and T. Yasuki: *A cfd analysis method for prediction of vehicle exterior wind noise*. SAE International Journal, Passeng. Cars - Mech. Syst., 10:286–298, March 2017.

[4] J. Ask and L. Davidson: *A numerical investigation of the flow past a generic side mirror and its impact on sound generation*. Journal of Fluids Engineering, 131(6), May 2009.

[5] J. Ask and L. Davidson: *The sub-critical flow past a generic side mirror and its impact on sound generation and propagation*. In the 12th AIAA/CEAS Aeroacoustics Conference (27th AIAA Aeroacoustics Conference). Cambridge, Massachusetts., May 2006.